

STATE OF CALIFORNIA DEPARTMENT OF TRANSPORTATION
TECHNICAL REPORT DOCUMENTATION PAGE
 TR0003 (REV. 10/98)

1. REPORT NUMBER CA03-0272	2. GOVERNMENT ASSOCIATION NUMBER	3. RECIPIENT'S CATALOG NUMBER
4. TITLE AND SUBTITLE Development of 3D Microwave Imaging Technology for Damage Assessment of Concrete Bridge	5. REPORT DATE November 2003	6. PERFORMING ORGANIZATION CODE
	8. PERFORMING ORGANIZATION REPORT NO. FHWA/CA/IR/2004/02	
7. AUTHOR(S) Maria Q. Feng, Franco De Flaviis, Yoo Jin Kim, Hyunseok Ko, and Sunan Liu	10. WORK UNIT NUMBER	
9. PERFORMING ORGANIZATION NAME AND ADDRESS Civil and Environmental Engineering E4120 Engineering Gateway University of California, Irvine Irvine, CA 92697-2175	11. CONTRACT OR GRANT NUMBER 65A0140	
	13. TYPE OF REPORT AND PERIOD COVERED Final Report	
12. SPONSORING AGENCY AND ADDRESS California Department of Transportation Division of Research and Innovation, MS-83 1227 O Street Sacramento, CA 95819	14. SPONSORING AGENCY CODE	
	15. SUPPLEMENTAL NOTES	
16. ABSTRACT An innovative microwave 3-dimensional (3D) sub-surface imaging technology is developed for detecting and quantitatively assessing internal damage of concrete structures. This technology is based on reconstruction of dielectric profile (image) of a structure illuminated with microwaves sent and received by antenna arrays. In this project, it is found that focused microwave is much more effective than the unfocused ones in detecting small defects, and thus a unique numerical bi-focusing technique is developed to focus both the transmitting and the receiving microwave signals. A multi-frequency technique is applied to improve the image clarity by reducing the background noises. Two software packages have been developed in this study: one for 3D image reconstruction and the other for image visualization. Two engineering prototypes have been fabricated: one consists of arrays of 128 antennas and the other 256 antennas with sophisticated electronic switching controlled by software. The first prototype system is tested on concrete blocks, in which voids and steel bars are successfully detected. It was experimentally demonstrated that bi-focusing operator can double the image resolution.		
17. KEY WORDS Microwave, Nondestructive Evaluation (NDE), 3D Imaging Technology, Damage Detection	18. DISTRIBUTION STATEMENT No restrictions. This document is available to the public through the National Technical Information Service, Springfield, VA 22161	
19. SECURITY CLASSIFICATION (of this report) Unclassified	20. NUMBER OF PAGES 126	21. PRICE



Division of Research
& Innovation

Development of 3D Microwave Imaging Technology For Damage Assessment of Concrete Bridge

Final Report

Development of 3D Microwave Imaging Technology For Damage Assessment of Concrete Bridge

Final Report

Report No. CA03-0272

November 2003

Prepared By:

Department of Civil and Environmental Engineering
University of California, Irvine
Irvine, CA 92697-2175

Prepared For:

California Department of Transportation
Division of Research and Innovation, MS-83
1227 O Street
Sacramento, CA 95814

DISCLAIMER STATEMENT

This document is disseminated in the interest of information exchange. The contents of this report reflect the views of the authors who are responsible for the facts and accuracy of the data presented herein. The contents do not necessarily reflect the official views or policies of the State of California or the Federal Highway Administration. This publication does not constitute a standard, specification or regulation. This report does not constitute an endorsement by the Department of any product described herein.

For individuals with sensory disabilities, this document is available in Braille, large print, audiocassette, or compact disk. To obtain a copy of this document in one of these alternate formats, please contact: the Division of Research and Innovation, MS-83, California Department of Transportation, P.O. Box 942873, Sacramento, CA 94273-0001.

FINAL REPORT TO
THE CALIFORNIA DEPARTMENT OF
TRANSPORTATION

**Development of
3D Microwave Imaging Technology
For Damage Assessment of Concrete Bridge**

65A0140

Maria Q. Feng, Professor
Franco De Flaviis, Assistant Professor

And
Yoo Jin Kim, Post Graduate Researcher
Hyunseok Ko, and Sunan Liu, Graduate Research Assistants

DEPARTMENT OF CIVIL AND ENVIRONMENTAL ENGINEERING
UNIVERSITY OF CALIFORNIA, IRVINE

PRINTED NOVEMBER 2003

STATE OF CALIFORNIA · DEPARTMENT OF TRANSPORTATION
TECHNICAL REPORT DOCUMENTATION PAGE
 TR0003 (REV. 9/99)

1. REPORT NUMBER FHWA/CA/IR/2004/02	2. GOVERNMENT ASSOCIATION NUMBER	3. RECIPIENT'S CATALOG NUMBER
4. TITLE AND SUBTITLE Development of 3D Microwave Imaging Technology for Damage Assessment of Concrete Bridge		5. REPORT DATE November, 2003
7. AUTHOR Maria Q. Feng, Franco De Flaviis, Yoo Jin Kim, Hyunseok Ko, and Sunan Liu		6. PERFORMING ORGANIZATION CODE UC Irvine
9. PERFORMING ORGANIZATION NAME AND ADDRESS Civil and Environmental Engineering E4120 Engineering Gateway University of California, Irvine Irvine, CA 92697-2175		8. PERFORMING ORGANIZATION REPORT NO.
12. SPONSORING AGENCY AND ADDRESS California Department of Transportation (Caltrans) Sacramento, CA		10. WORK UNIT NUMBER
15. SUPPLEMENTARY NOTES		11. CONTACT OR GRANT NUMBER 65A0140
16. ABSTRACT An innovative microwave 3-dimensional (3D) sub-surface imaging technology is developed for detecting and quantitatively assessing internal damage of concrete structures. This technology is based on reconstruction of dielectric profile (image) of a structure illuminated with microwaves sent and received by antenna arrays. In this project, it is found that focused microwave is much more effective than the unfocused ones in detecting small defects, and thus a unique numerical bi-focusing technique is developed to focus both the transmitting and the receiving microwave signals. A multi-frequency technique is applied to improve the image clarity by reducing the background noises. Two software packages have been developed in this study: one for 3D image reconstruction and the other for image visualization. Two engineering prototypes have been fabricated: one consists of arrays of 128 antennas and the other 256 antennas with sophisticated electronic switching controlled by software. The first prototype system is tested on concrete blocks, in which voids and steel bars are successfully detected. It was experimentally demonstrated that bi-focusing operator can double the image resolution.		13. TYPE OF REPORT AND PERIOD COVERED Final Report
17. KEYWORDS Microwave, Nondestructive Evaluation (NDE), 3D Imaging Technology, Damage Detection	18. DISTRIBUTION STATEMENT No restrictions.	
19. SECURITY CLASSIFICATION (of this report) Unclassified	20. NUMBER OF PAGES	21. COST OF REPORT CHARGED

DISCLAIMER: The opinion, findings, and conclusions expressed in this publication are those of the authors and not necessarily those of the STATE OF CALIFORNIA

Contents

List of Figures	iii
List of Tables	vi
Acknowledgement	vii
Abstract	viii
1. Introduction.....	1
1.1. Problem Statement.....	1
1.2. Review of the State of the Art	3
1.3. Research Objective	7
2. Overview of the Proposed Microwave Imaging Technology	8
2.1. Overview.....	8
2.1.1. Surface-Focused Imaging Technology	9
2.1.2. Sub-Surface-Focused Imaging Technology.....	10
2.2. Previous Related Works	11
3. Software Development.....	15
3.1. Image Reconstruction Algorithm and Software	15
3.2. Study of Image Resolution	19
3.3. Multi-Frequency Technique	20
3.4. Visualization Software.....	22
4. Hardware Development	23
4.1. Prototype I	23
4.1.1. Antenna Array Prototype I.....	23
4.1.1.1. Single-Slot Antenna Element.....	24
4.1.1.2. 16×8 Antenna Array	26
4.1.2. Control Module for Prototype I	29
4.2. Prototype II	30

4.2.1. Antenna Array Prototype II	31
4.2.1.1. Single-Slot Antenna Element.....	31
4.2.1.2. PIN Diodes.....	34
4.2.1.3. 4×4 Antenna Array	36
4.2.1.4. 16×8 Antenna Array	43
4.2.2. System Integration	49
4.2.2.1. Construction of Measurement Matrix.....	50
4.2.2.2. Components Details.....	51
4.2.2.3. Control Program.....	53
4.2.2.4. Measurement Speed Evaluation.....	56
5. Numerical Simulation	57
5.1. Effective Focusing Area (EFA).....	57
5.2. Simulation Results Using 5.2 GHz.....	58
5.3. Simulation Results Using 10.0 GHz.....	64
6. Experimental Verification.....	66
6.1. Microwave Imaging Using Prototype I	66
6.1.1. Experimental Setup.....	66
6.1.2. Experimental Results	68
7. Operators Manual of Imaging System	71
8. Summary and Concluding Remarks	76
Nomenclature.....	77
References.....	78
A. Appendix A: Reference Manual of Modules.....	80
B. Appendix B: Manual of Image Reconstruction Program	87
C. Appendix C: Manual of Control Program	99

List of Figures

Figure 1.1 Void and performance degradation	3
Figure 1.2 Infrared Image Indicating Voids of a Jacketed Column.....	6
Figure 2.1 Reflection Mechanisms in RC Column.....	9
Figure 2.2 Use of Dielectric Lens to Focus Waves on Bonding Interface	10
Figure 2.3 Use of Microwave Arrays to Focus Waves on Sub-Surface Point.....	11
Figure 2.4 Designed Dielectric Lenses	12
Figure 2.5 Experimental Setup	12
Figure 2.6 Typical Responses Using S_{11} measurement	13
Figure 2.7 Scanned Microwave Image of Concrete Column Showing Debonding.....	13
Figure 3.1 Electromagnetic Compensation Principle	16
Figure 3.2 Imaging Geometry.....	17
Figure 3.3 Resolution of the system (25mm) at 5.2GHz	20
Figure 3.4 Comparison of Single/Multi Illuminating Frequency (Image of Two Point-like Objects).....	21
Figure 3.5 Example Screen Shot of Visualization Software.....	22
Figure 4.1 Two-Dimensional Planar Rectangular Microwave Antenna Array	24
Figure 4.2 Geometry of Single-Slot Antenna	25
Figure 4.3 Measurement Result of Single-Slot Antenna Element.....	26
Figure 4.4 Fabricated Two-Dimensional Antenna Array	27
Figure 4.5 Measurement Results of 16×8 Antenna Array	28
Figure 4.6 Switch Box and Power Supply (Manual Operation).....	29
Figure 4.7 Description of Three-Dimensional Imaging System (Block Diagram).....	30
Figure 4.8 Structures and Dimension of Single-Slot Antenna Element	31
Figure 4.9 Single-Slot Antenna Element	32
Figure 4.10 Comparison Between Simulation and Measurement Result	32
Figure 4.11 Radiation Pattern of Slot Antenna.....	33
Figure 4.12 Test and De-embedding Fixture	34
Figure 4.13 Measurement Comparisons of PIN Diodes	35
Figure 4.14 Dimension of PIN Diode (MPP-4203)	35

Figure 4.15 Fabricated 4 by 4 Antenna Array	36
Figure 4.16 Layout of Ground	37
Figure 4.17 Switching Behavior of Antenna	37
Figure 4.18 Comparison Between Simulation and Measurement	38
Figure 4.19 With & Without Diodes.....	38
Figure 4.20 Measurement Set-Up for Insertion Loss.....	39
Figure 4.21 Horn Antenna Dimension.....	39
Figure 4.22 Measurement Result	40
Figure 4.23 Complete Slot Antenna Array	41
Figure 4.24 Measurement of Each Antenna Element	42
Figure 4.25 Final Array with Feed Network and Bias Lines.....	44
Figure 4.26 Final Array with Slots	45
Figure 4.27 Original Layout	46
Figure 4.28 Simulation Result	46
Figure 4.29 Solution I	47
Figure 4.30 Simulation Result	47
Figure 4.31 Entire Array with Solution I	47
Figure 4.32 Simulation Result	47
Figure 4.33 Solution II.....	48
Figure 4.34 Simulation Result	48
Figure 4.35 Overall Array with Solution II	48
Figure 4.36 Simulation Result	48
Figure 4.37 Integrated System with Control Rack, Laptop, and Network Analyzer	49
Figure 4.38 Schematic of Algorithm for System Integration	50
Figure 4.39 Demo Model of 1:128 Switch	51
Figure 4.40 Texas Instruments Multiplexers CD74HC4051E.....	52
Figure 4.41 1:8 Switch.....	52
Figure 4.42 Practical Model of 1:128 Switch.....	53
Figure 4.43 Measurement of Data Through Network Analyzer	54
Figure 4.44 Execution of Imaging Program after Measurement	54
Figure 4.45 Panel Interface	55

Figure 4.46 Measurement Time Shown in Oscilloscope	56
Figure 5.1 Effective focusing area of planar rectangular antenna array	58
Figure 5.2 Simulation Results with Descriptions	63
Figure 5.3 Resolution Improvement Using Higher Frequency.....	65
Figure 6.1 Experimental Setup	67
Figure 6.2 Description of Calibration Scheme	68
Figure 6.3 Reconstructed Image of Case 1	69
Figure 6.4 Reconstructed Image of Case 2	70
Figure 6.5 Reconstructed Image of Case 3	70
Figure 7.1 Job Flow of the System	71
Figure 7.2 Block Diagram of the System.....	72
Figure 7.3 Outside View of the System	72
Figure 7.4 Front Panel of Control Module.....	74
Figure 7.5 Example Screen Shot of Visualization Software.....	75
Figure A.1 Schematic of Algorithm.....	81
Figure A.2 Practical Model of 1:128 Switch	82
Figure A.3 Communication Between LabJack and Network Analyzer.....	83
Figure A.4 Element of Measurement Matrix Corresponding to the Number of Element in Antenna Array.....	84
Figure A.5 Interface of LabView	85
Figure A.6 Photo of LabJack	85
Figure A.7 Using the LabJack with Enable Line and Address Line.....	86
Figure A.8 Truth table of MAX396.....	86
Figure C.1 Hierarchy of the LabView program ‘caltrans.vi’	99

List of Tables

Table 1.1 Evaluation of Established Methods	6
Table 6.1 Descriptions of Cases for Experimental Study	66

Acknowledgement

The project was supported by California Department of Transportation under Award No. 65A0140. The authors would like to thank the project managers, Mr. Rosme Aguilar and Mr. Stephen Sahs with Caltrans, for their supervision, encouragement and support.

Professor Luis Jofre at Technical University of Catalonia, Barcelona, Spain, provided technical advice regarding imaging algorithm and antenna design.

Abstract

An innovative microwave 3-dimensional (3D) sub-surface imaging technology is developed for detecting and quantitatively assessing internal damage of concrete structures. This technology is based on reconstruction of dielectric profile (image) of a structure illuminated with microwaves sent and received by antenna arrays.

In this project, it is found that focused microwave is much more effective than the unfocused ones in detecting small defects, and thus a unique numerical bi-focusing technique is developed to focus both the transmitting and the receiving microwave signals. A multi-frequency technique is applied to improve the image clarity by reducing the background noises.

Two software packages have been developed in this study: one for 3D image reconstruction and the other for image visualization. Two engineering prototypes have been fabricated, one consists of arrays of 128 antennas and the other 256 antennas with sophisticated electronic switching controlled by software. The first prototype system is tested on concrete blocks, in which voids and steel bars are successfully detected. It was experimentally demonstrated that bi-focusing operator can double the image resolution.

Chapter 1

INTRODUCTION

1.1. Problem Statement

This research intended to target the following problems associated with concrete bridges.

Problem 1: Assessment of internal damage in concrete bridges

Statistics have shown that one third of the nation's highway bridges are rated either structurally deficient or functionally obsolete, and many of these bridges will fail to achieve their design life of fifty to seventy-five years (Dunker and Rabbat, 1990). In 1995, the Federal Highway Administration (FHWA) estimated the cost at approximately \$6 billion per year in the next 25 years to repair and replace these bridges, but the TEA-21 budget is only at the level of 3 billion per year (FHWA, 1998). It is important, then, to be able to accurately predict remaining lives of existing bridges by assessing their structural integrity. Currently, the assessment heavily relies on visual inspections, which apparently have some limitations. In California, majority of highway bridges are concrete bridges, and such invisible damage as voids and cracks inside concrete and debonding between rebars and concrete caused by corrosions, earthquakes, and other reasons, is of significant concern. Sometimes it is difficult to assess the extent of damage developed inside the concrete based only on concrete surface cracks.

Problem 2: Detection of damage within concrete structures wrapped with FRP jackets

Recently, FRP composite jacketing has demonstrated its ability to enhance the confinement and thus to improve the structural integrity of old concrete bridge columns and girders. The light weight, high strength, and ease of installation make such materials very practical for retrofitting concrete bridges. Indeed, in California there are an

increasing number of bridge columns being strengthened with FRP jackets including approximately three thousand columns in the most recent retrofit project involving the I-80 viaduct (Yolo Causeway) in Sacramento-Yolo County.

Despite the proven structural performance of the jacketing retrofit measure and the large number of bridge columns being retrofitted with FRP jackets, the post-disaster damage of the concrete columns covered by the FRP composites, remains a significant concern. Such damage includes large concrete cracks, debonding between concrete and rebars, and debonding between concrete and FRP jackets. Unfortunately, there is no unintrusive technology available at this moment to detect such invisible damage.

Problem 3: Quality assurance in FRP jacketing

Unlike steel jacketing where grout is pumped to fill gaps between the jacket and the column at the time of installation, a jacket made of several layers of FRP material is often manually applied to a concrete structural element, layer by layer, glued with adhesive epoxy. The bonding quality between the layers of the composite jacket and between the jacket and concrete is of another significant concern, as it purely depends on the workmanship. Imperfect bonding condition, particularly the existence of a large area of voids, can significantly degrade the structural integrity and safety that could otherwise be attainable by jacketing. This has been demonstrated by the results of the experiment performed by the PI at UCI (Haroun, et al., 1997). Three identical half-scale circular bridge columns with lap splices were built. Two of the columns were wrapped with identical glass-fiber jackets: one was well wrapped with the adhesive epoxy carefully applied to the entire jacketing area, while the other was poorly wrapped with many voids in the epoxy layers. Force-displacement envelopes from the cyclic loading tests of the three columns (unwrapped, well wrapped, and poorly wrapped) are shown in [Figure 1.1](#). The well wrapped column performed excellently by increasing the column ductility factor from less than two (unwrapped column) to six, while the poorly wrapped with many voids barely reached the ductility factor of three.

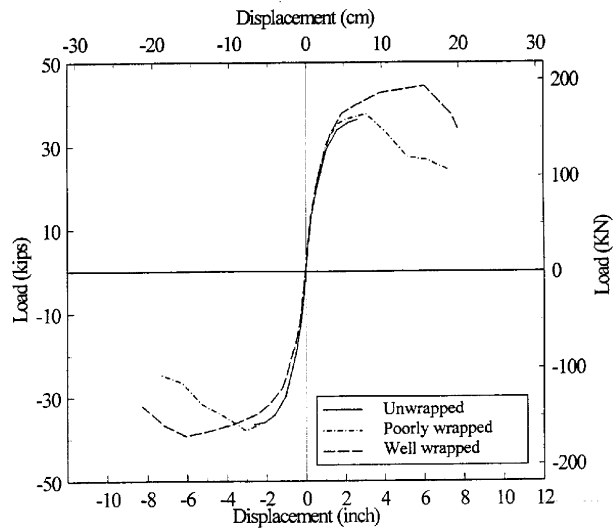


Figure 1.1 Void and performance degradation

Therefore, it is very important to assess the bonding condition of the composite jackets after the jacket is installed, in order to ensure the expected performance of the jacketed columns. Once detected, the voids in the bonding interface can be eliminated by injecting epoxy at the time of jacket installation. The same PI has tried the infrared thermography for this purpose and found it to be ineffective for a thick jacket with low heat conductivity. In addition, the heat applied to the column for building a thermographic profiling may change the property of FRP materials especially before the materials are fully cured.

1.2. Review of the State of the Art

Various NDE techniques have been studied to detect cracks and voids of concrete and debonding/delaminations between concrete and rebars. Among them, acoustic wave, X-ray, nuclear-magnetic resonance (NMR), infrared thermography, and ground penetrating radar (GPR) are mostly effective. Except for the infrared thermography, none of them, however, has been studied for FRP-retrofitted concrete structures

The acoustic/ultrasonic wave detection is based on the difference in wave velocity when acoustic/ultrasonic waves propagate through different materials. At the boundaries between materials, the waves are reflected. The damage such as cracks also act as boundaries. By analyzing the echoes, it is possible to determine the locations of these boundaries, as well as the materials in each layer. If sufficient data are available, a 2-D or 3-D image of the reflected wave may be reconstructed. The ultrasonic imaging theory is largely dependent on ray tracing and not difficult to implement. For reinforced concrete columns wrapped with steel jackets, acoustic wave method can be effective because metal conducts sound wave very well. An FHWA-sponsored project has developed an ultrasonic imaging method to detect cracks in steel bridges (Chase et al., 1997), and other research projects have demonstrated the potential to detect voids in concrete using ultrasonic tomography (Olson, et al, 1993), although the results are influenced by sizes and shapes of aggregates.

The NMR imaging technology is based on the differences in natural resonant frequencies (in MHz range) in different materials under nuclear excitation. High-sensitivity receivers receive these signals, and an image of resonant frequency is reconstructed for each material. Although it is possible for an NMR system to generate high resolution 3-D images, it is very expensive and difficult to operate when a high spatial resolution is required. X-ray imaging is, in principle, very similar to the ultrasonic imaging and is good in penetrating through loose materials. However, X-ray machines are usually heavy and difficult to use, as X-ray is harmful to human body.

GPR is widely used to detect anomalies in a material. It is built to detect the boundaries between materials that have different electrical properties, namely, dielectric constant and conductivity. The basic idea of GPR is very similar to that of the acoustic ultrasonic system. A GPR transmitter sends a fast electromagnetic (EM) pulse with a width in the range of nano-seconds. This pulse propagates through materials and gets reflected at the interfaces between the materials with different electrical properties. The reflected signal, mixed with the transmitted wave, is received by the receiver. If the transmitted signal is narrow enough, the reflected pulses, though very weak compared with transmitted one and distorted due to the loss in the materials, can be identified, taking advantage of the time separation between the transmitted and received pulses. By

converting the time scale to distance scale, the locations of the boundaries are then determined. Small and reliable devices producing very short pulses (0.2 ns) able to obtain spatial resolutions in the range of centimeters have been fabricated and used as single sensors and also as array of sensors for imaging purposes (Mast, et al., 1998). The GPR system is very effective when used to detect relatively large objects having appreciable difference in dielectric constant with the host material through which EM waves propagate with little loss. In fact, GPR was studied for identifying the delaminations and reinforcing steel rebars in a concrete bridge deck slab (Chase et al., 1997). However, for the jacketed columns which require deep detection, the traditional, time domain-based GPR is not particularly effective primarily because the received signal is heavily contaminated by noise as it propagates.

Infrared thermography has been studied for detecting delaminations on concrete bridge deck and concrete surface fatigue cracks (Chase et al., 1997), as well as concrete pavement voids (Weil, 1994). To build a thermographic profile, one heats up, through the surface, the entire structure with electric lamps or a hair-dryer-like heater, and then measures the infrared radiation from the structure. At the points where voids or cracks exist, the thermographic profile will be different from other areas due to the difference in heat conductance between air and concrete. This PI has worked with the Aerospace Corporation to use an infrared camera to assess the bonding condition of an FRP-jacketed column and one of the images is shown in Figure 1.2. The infrared thermography, by nature, is not very accurate because of the continuous distribution of the heat and the amplitude-only measurement of the heat signal. It is impossible to detect the radial location and depth of voids. In addition, it is difficult to use infrared thermography for deep detection. The heat applied to the column for building a thermographic profile may change the property of FRP materials especially before the materials are fully cured.

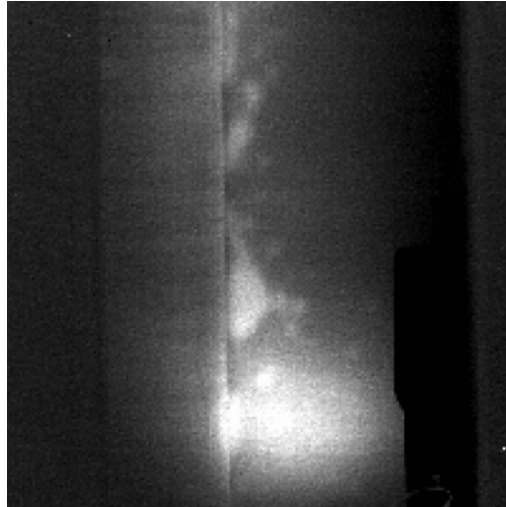


Figure 1.2 Infrared Image Indicating Voids of a Jacketed Column

Regarding the established nondestructive evaluation methods, advantages and disadvantages are summarized and compared with each other in [Table 1.1 \(Kim, 2002\)](#).

Table 1.1 Evaluation of Established Methods

Technique	Applications	Advantages	Potential Obstacles to Implementation
Acoustic imaging (Ultrasonic, impact echo and acoustic emission)	Location of voids	Not affected by the reinforcement	Long data acquisition process Highly sensitive to the aggregate size
Infrared thermography	Location of cracks, voids, and delaminations	Easy to apply	No depth information Sensitive to environmental conditions No deep detection Heat affects FRP bond curing
GPR	Location of reinforcement, voids and cracks	Rapid and non-contact measurement and imaging of large area	Limited algorithms in imaging concrete High attenuation of EM waves in moisture Total reflection from metals
Radiography & Radioactive tomography	Location of reinforcement, voids and cracks	High resolution images due to the use of non-diffracting sources (X-ray) with high penetrating capability	Expensive and dangerous Time consuming Accessibility to both sides of the object required

1.3. Research Objective

The primary objective of this project is to develop a portable 3D microwave imaging technology using antenna arrays for nondestructive evaluation of internal and invisible damage in reinforced concrete bridge members with and without FRP composite jackets. Targeted damage includes air voids, cracks, rebar de-bonds, and FRP jacket de-bonds due to poor installation workmanship and earthquakes.

Chapter 2

OVERVIEW OF THE PROPOSED MICROWAVE IMAGING TECHNOLOGY

2.1. Overview

The proposed microwave imaging technology is based on the analysis, in time and frequency domains, of a continuous microwave sent toward and reflected from a layered medium. It is well known that when a plane electromagnetic (EM) wave launched from an illuminating device (typically an antenna or a lens) toward a layered medium encounters a dielectric interface, a fraction of the wave energy is reflected while the rest is transmitted into the medium.

In the case of a RC column wrapped with a layer of FRP jacket subjected to the incoming wave as shown in [Figure 2.1](#), the first reflection (#1) occurs at the surface of the jacket, while the second (#2) at the interface between the jacket and the adhesive epoxy, and the third (#3) at the interface between the adhesive epoxy and the concrete, assuming the jacket is perfectly bonded to the column without a void or debonding. In addition, reflections from the interface between the concrete and steel reinforcing rebars and from the sources internal to the illuminating device will also take place. If there is an air gap resulting from a void or debonding between the composite jacket and the column, an additional reflection (#4) will occur at this particular location, as illustrated in [Figure 2.1](#). Therefore, imperfect bonding conditions can be, in principle, detected by analyzing these reflections in the time and/or in the frequency domains.

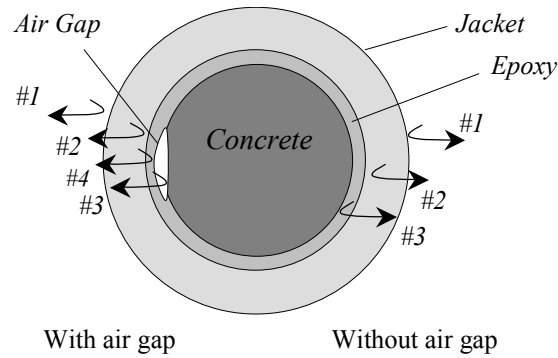


Figure 2.1 Reflection Mechanisms in RC Column

Based on the numerical studies performed by the authors, focused microwave is much more effective than the conventional un-focused microwave for detecting small defects (Feng et al., 2002). The authors proposed two innovative techniques for focusing microwaves: one using dielectric lenses (referred to as surface-focused imaging technology and the other using antenna array (referred to as sub-surface-focused imaging technology).

2.1.1. Surface-Focused Imaging Technology

The surface-focused microwave imaging technology is proposed for assessing damage not too deep below the structure surface, such as internal voids near the surface and debonding between concrete and FRP jackets. Previous work by this proposal team demonstrated that the plane EM wave is not effective in detecting such voids and debonding, as the reflection contribution of the voids and debonding is very small compared to that from the concrete structure itself. In order to overcome the difficulty associated with the plane EM wave, the use of a dielectric lens was invoked to focus the EM wave on the bonding interface of the jacketed column while diffusing the field in other regions of no interest, as illustrated in Figure 2.2. Waves reflected from the other regions where the beam is defocused will be much weaker than those from the focused region, and thus the difference between the perfect and poor bonding conditions in the focused region can be detected more effectively.

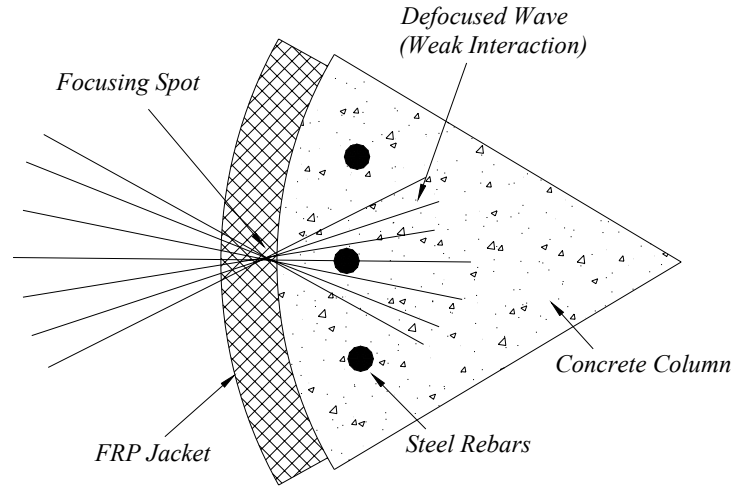


Figure 2.2 Use of Dielectric Lens to Focus Waves on Bonding Interface

2.1.2. Sub-Surface-Focused Imaging Technology

In order to assess damage within a concrete structural element far away from its surface and to obtain the depth information about damage, a sub-surface-focused microwave imaging technology using transmitting and receiving arrays, as shown in [Figure 2.3](#), is proposed. This technology can construct a 3D microwave image, showing the information under the surface, thus it is possible to detect the depth of damage in concrete. Furthermore, this technology uses transmitting and receiving arrays and the focusing point can be quickly changed by software without physically moving the hardware, which makes it possible to quickly measure a large area involving many points of inspection.

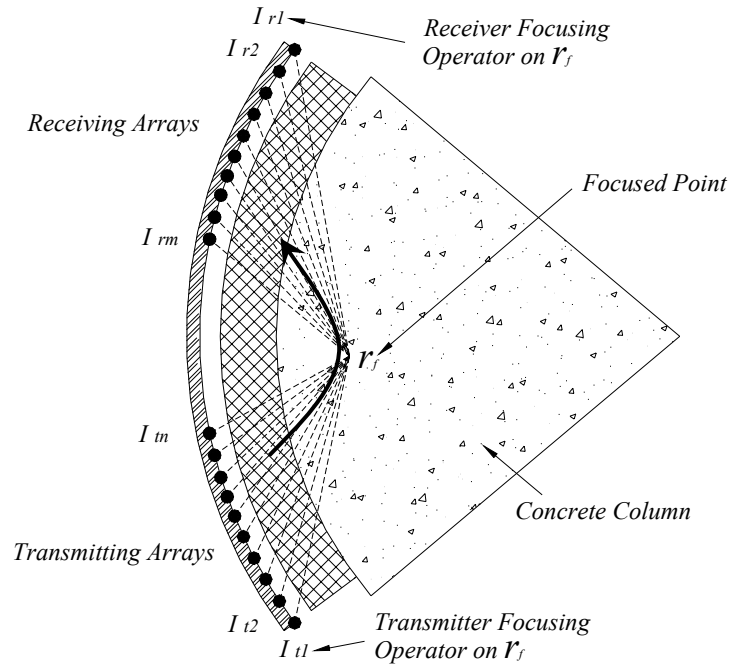
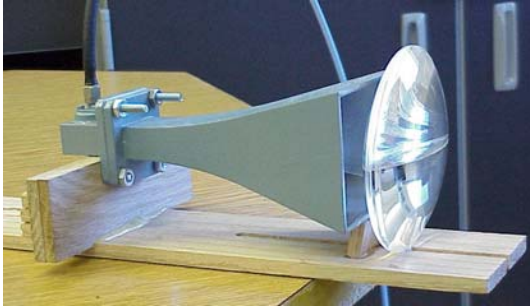


Figure 2.3 Use of Microwave Arrays to Focus Waves on Sub-Surface Point

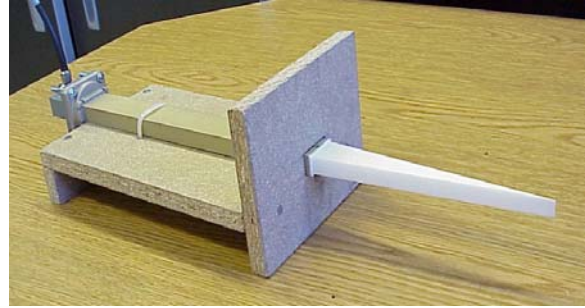
2.2. Previous Related Works

Under the support of NSF, the proposal team developed the surface-focused microwave imaging technology and experimentally demonstrated its efficacy in detecting debonding in FRP-jacketed columns.

Dielectric lenses were developed for focusing microwaves onto locations of interest in concrete structures. Two types of the developed lenses are shown in [Figure 2.4](#): one in triangular and the other in circular shape. They can be setup for the reflection measurement (S_{11}) (requiring only one lens as shown in [Figure 2.5\(a\)](#)), or the transmission measurement (S_{21}) (requiring two lenses as shown in [Figure 2.5\(b\)](#)).



(a) Circular Lens

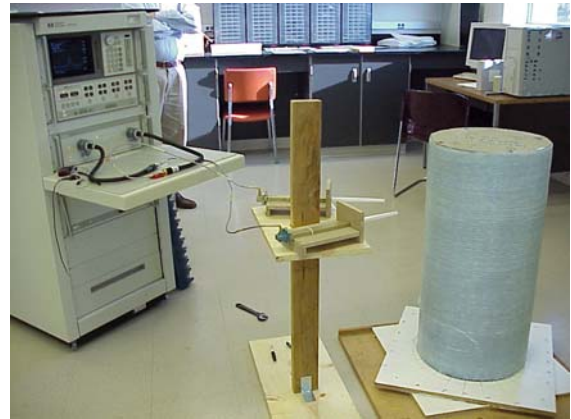


(b) Triangular Lens

Figure 2.4 Designed Dielectric Lenses



(a) Reflection Measurement (S_{11})



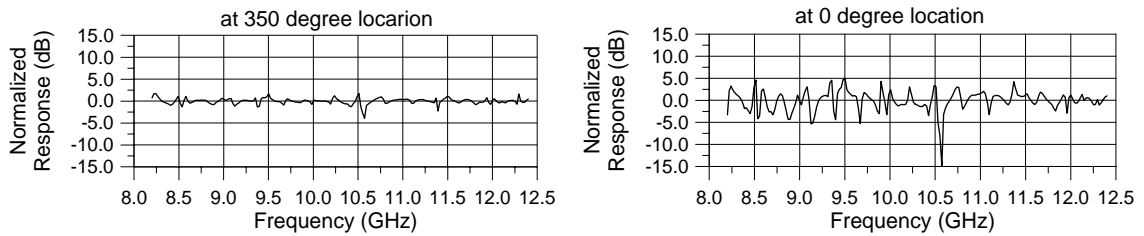
(b) Transmission Measurement (S_{21})

Figure 2.5 Experimental Setup

The effectiveness of the proposed EM imaging technology using focused EM waves was investigated through a series of experiments on a variety of concrete specimen including concrete cubs and FRP-jacketed concrete columns. The concrete cub has 30 cm (11.81 in) in each side and the concrete columns are of 40.64 cm (16 in) in diameter and 81.28 cm (32 in) in height. Some of these columns were built without reinforcing rebars and the some with No. 5 longitudinal rebars and No. 2 circular hoops, in order to examine the influence of steel rebars on the EM wave reflection. Each of the columns was wrapped with a three-layer glass FRP jacket. Various voids and debonding conditions were artificially introduced inside the concrete cubs and between the jackets and the columns of the jacketed columns.

Figure 2.5 shows an experimental setup with the concrete columns respectively using the triangular and circular lenses. Continuous sinusoidal microwaves with its

frequency sweeping from 8.2 GHz to 12.4 GHz were generated from the signal analyzer and sent to the jacketed columns through the lenses. Typical frequency-domain responses by S_{11} measurement using one circular lens are plotted in the Figure 2.6. The response has been normalized by the reference value representing a perfect bonding condition. It is shown that the response from the poor bonding condition in Figure 2.6(b) has a large variance while the one from the good bonding condition in Figure 2.6(a) is almost zero.



(a) Response from Good Bonding Condition (b) Response from Poor Bonding Condition

Figure 2.6 Typical Responses Using S_{11} measurement

Figure 2.7 shows a scanned image of a column surface area. This area contains a void between the jacket and the column caused by a hole with a diameter of approximately 2 cm in the concrete column surface. Although the air void cannot be seen from the outside of the jacket, the scanned microwave images clearly identify the location and size of the void.

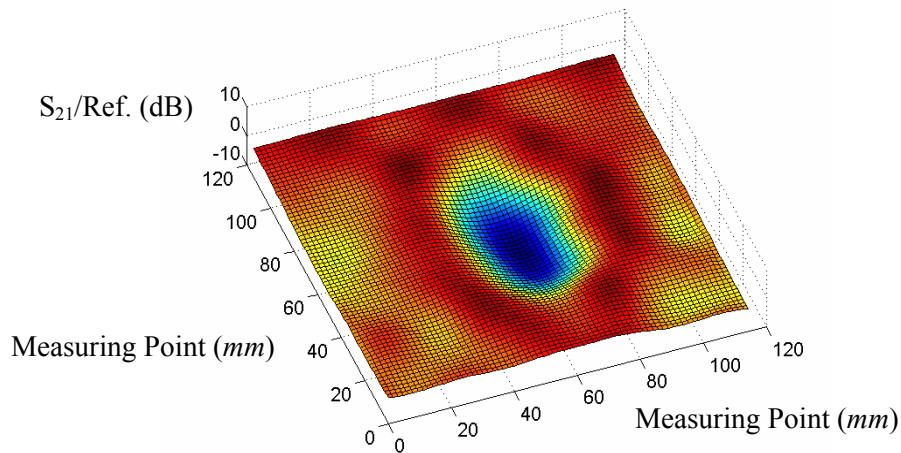


Figure 2.7 Scanned Microwave Image of Concrete Column Showing Debonding

From the experimental results, it is demonstrated that the surface-focused imaging technology can successfully detect the location and size of voids in concrete structures with and without FRP jackets. Accurate information about the void's depth, however, cannot be easily obtained.

Chapter 3

SOFTWARE DEVELOPMENT

3.1. Image Reconstruction Algorithm and Software

From the electromagnetic point of view, nondestructive evaluation in civil engineering can be confronted with the identification of dielectric inhomogeneities (as air void or steel rebar) inside homogeneous dielectric materials (as concrete or FRP). For the reconstruction or imaging of these defects, an illumination field has to be applied, propagating uniformly through the medium. When the illumination field reaches the defects, the uniformity will be lost and a disturbance on the existing field, generally called total field (\mathbf{E}_t) as represented in [Figure 3.1\(a\)](#), will be created. In order to model this situation following the electromagnetic compensation principle ([Harrington, 1961](#)), the inhomogeneities can be replaced by an equivalent electric current distribution:

$$\mathbf{J}_{eq} = j\omega(\varepsilon_{obj} - \varepsilon_{media})\mathbf{E}_t \quad (3.1)$$

where ε_{obj} and ε_{media} are permittivity of the object and the homogeneous surrounding medium respectively. These currents can also be treated as the source of a scattered field \mathbf{E}_s ($\mathbf{E}_s = \mathbf{E}_t - \mathbf{E}_i$) placed inside a homogeneous medium in [Figure 3.1\(b\)](#):

$$\mathbf{E}_s = \int_V \mathbf{J}_{eq} \frac{e^{-jk\mathbf{r}}}{4\pi\mathbf{r}} dV \quad (3.2)$$

When the electric contrast (based on the difference of permittivity and the size of the defect in terms of wavelengths) between the defects and the homogenous surrounding medium is low enough, the disturbances created on the propagating field by these inhomogeneities can be considered small, and the total field can be approximated by the initial incident field ($\mathbf{E}_t \approx \mathbf{E}_i$). The equivalent electric current distribution, therefore, can also be approximated by:

$$\mathbf{J}_{eq} = j\omega(\varepsilon_{obj} - \varepsilon_{media})\mathbf{E}_i \quad (3.3)$$

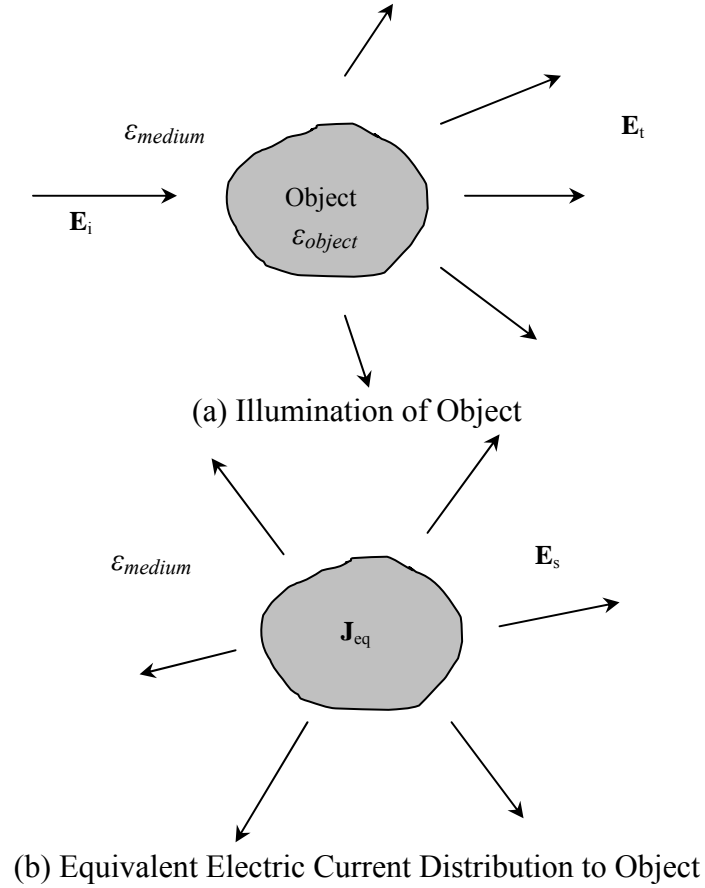


Figure 3.1 Electromagnetic Compensation Principle

This approximation (Slaney et al., 1984) is called the first-order Born approximation and it simplifies enormously the inverse reconstruction procedure. In order to obtain an image of the object (internal dielectric inhomogeneities in the case) from external measurements, the reconstruction of a current distribution \mathbf{J}_{eq} from the scattered field measured over a certain wrapping surface can be the replica of the object. The current distribution is able to be obtained from the inversion of the integral equation (2).

The geometry of imaging is shown in Figure 3.2, where the transmitting surface array is able to sequentially focus on every interrogation point of the reconstructing volume while the receiving surface array measures the scattered field enveloping the object. The measurement geometry uses $N_k \times N_l$ elements forming a transmitting array and $N_m \times N_n$ elements forming a receiving array. In the measurement, an $N_t \times N_r$ measurement matrix, where $N_t = N_k \times N_l$ is the total numbers of transmitting elements and

$N_r = N_m \times N_n$ is the total numbers of receiving elements, can be obtained as follows: for every selected transmitting element, the receiving array is scanned obtaining an N_r -measurement column, then the procedure is repeated for the rest of the N_t transmitting elements.

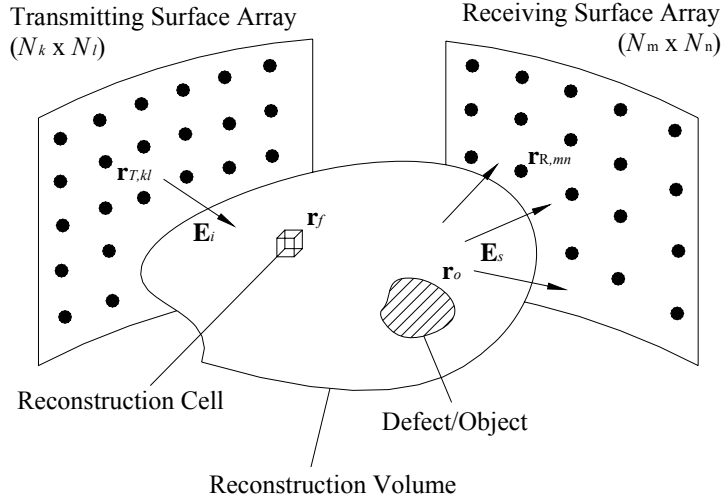


Figure 3.2 Imaging Geometry

The image reconstruction algorithm forms a point image by means of synthesizing the two focused arrays (transmitting and receiving arrays). All the elements of the arrays are weighted by a focusing operator so as to be focused on a unique point, which can be achieved by a numerical treatment of the measurement matrix. The focusing operator (Broquetas et al., 1991) can be obtained by taking an inverse of the field induced by a current point source. It is well known that the electric fields of the point electric source are proportional to the Green's function, $e^{-jk_e|\mathbf{r}|}/4\pi\mathbf{r}$, while the electric fields are proportional to a Hankel function of the second kind whose argument is proportional to the distance from the source to the observation point in 2-dimensional space (Balanis, 1989). Therefore, the incident field at $\mathbf{r}_i=(x_i,y_i,z_i)$ when focusing from every transmitting point $\mathbf{r}_{Tkl}=(x_{Tkl},y_{Tkl},z_{Tkl})$ on the reconstructing point $\mathbf{r}_f=(x_f,y_f,z_f)$ can be expressed as

$$E_i(\mathbf{r}_i) = \sum_{l=1}^{N_t} \sum_{k=1}^{N_k} I_{Tkl}(\mathbf{r}_f) \cdot \frac{e^{-jk_e|\mathbf{r}_{Tkl}-\mathbf{r}_i|}}{4\pi|\mathbf{r}_{Tkl}-\mathbf{r}_i|} \quad (3.4)$$

where $I_{Tkl}(\mathbf{r}_f)$, the focusing operator, is given by

$$I_{Tkl}(\mathbf{r}_f) = \frac{4\pi |\mathbf{r}_{Tkl} - \mathbf{r}_f|}{e^{-jk_e |\mathbf{r}_{Tkl} - \mathbf{r}_f|}} \quad (3.5)$$

where $k_e = k_0 \sqrt{\varepsilon_r}$. The concrete was assumed to be homogeneous having uniform dielectric constant $\varepsilon_r=5.3$ for the purpose of computational ease (Feng et al., 2002).

Scattered field measured at $\mathbf{r}_{Rmn}=(x_{Rmn}, y_{Rmn}, z_{Rmn})$ of a defect placed at $\mathbf{r}_0=(x_0, y_0, z_0)$ can be expressed as following the Eq. (3.2).

$$E_s(\mathbf{r}_{Rmn}) = \int_V E_i(\mathbf{r}_0) \cdot I_{obj} \cdot \frac{e^{-jk_e |\mathbf{r}_{Rmn} - \mathbf{r}_0|}}{4\pi |\mathbf{r}_{Rmn} - \mathbf{r}_0|} dV \quad (3.6)$$

where I_{obj} is a constant for every object containing its electromagnetic macroscopic characteristics.

When focusing back the received field at $\mathbf{r}_{Rmn}=(x_{Rmn}, y_{Rmn}, z_{Rmn})$ on the interest point $\mathbf{r}_f=(x_f, y_f, z_f)$, electromagnetic image of E_f at $\mathbf{r}_f=(x_f, y_f, z_f)$ can be expressed as

$$E_f(\mathbf{r}_f) = \sum_{n=1}^{N_n} \sum_{m=1}^{N_m} E_s(\mathbf{r}_{Rmn}) \cdot I_{Rmn}(\mathbf{r}_f) \quad (3.7)$$

where $I_{Rmn}(\mathbf{r}_f)$, the focusing operator, is given by

$$I_{Rmn}(\mathbf{r}_f) = \frac{4\pi |\mathbf{r}_{Rmn} - \mathbf{r}_f|}{e^{-jk_e |\mathbf{r}_{Rmn} - \mathbf{r}_f|}} \quad (3.8)$$

Finally, all the processes can be grouped as follows:

$$E_f(\mathbf{r}_f) = \sum_{n=1}^{N_n} \sum_{m=1}^{N_m} \left[I_{Rmn}(\mathbf{r}_f) \cdot \int_V \left\{ I_{obj} \cdot \frac{e^{-jk_e |\mathbf{r}_{Rmn} - \mathbf{r}_0|}}{4\pi |\mathbf{r}_{Rmn} - \mathbf{r}_0|} \cdot \sum_{l=1}^{N_l} \sum_{k=1}^{N_k} I_{Tkl}(\mathbf{r}_f) \cdot \frac{e^{-jk_e |\mathbf{r}_{Tkl} - \mathbf{r}_0|}}{4\pi |\mathbf{r}_{Tkl} - \mathbf{r}_0|} \right\} dV \right] \quad (3.9)$$

In order to express Eq. (3.9) as a matrix form including the measurement matrix, the index of transmitting and receiving array can be arranged as follows:

$$\mathbf{r}_{Tkl} \rightarrow \mathbf{r}_{Tt} \quad \text{for transmitting array} \quad (3.10)$$

where subscript t is from 1 to the maximum number of transmitting element, and

$$\mathbf{r}_{Rmn} \rightarrow \mathbf{r}_{Rr} \quad \text{for receiving array} \quad (3.11)$$

where subscript r is from 1 to the maximum number of receiving element.

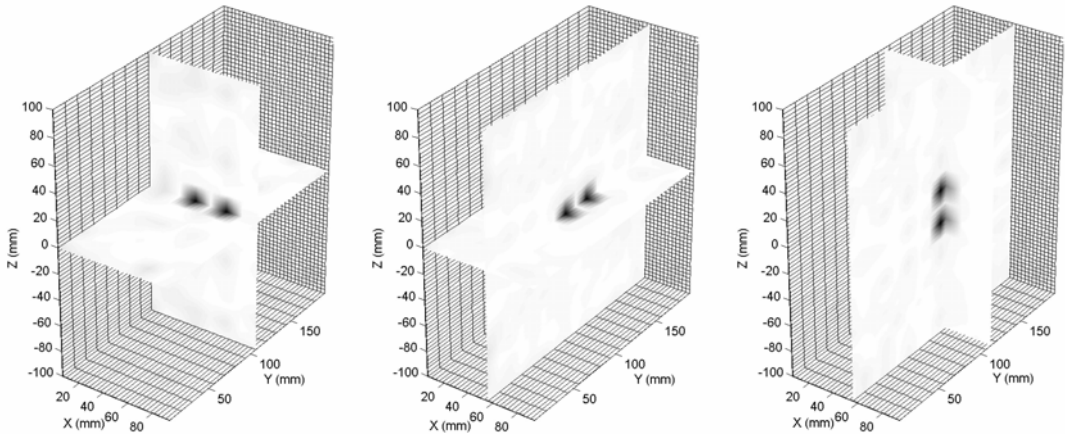
Then, the matrix form can be expressed as follows:

$$E_f(\mathbf{r}_f) = \begin{bmatrix} I_{T1} & I_{T2} & \Lambda & I_{Tr} \end{bmatrix} \cdot \begin{bmatrix} E_{s,T1R1} & E_{s,T1R1} & \Lambda & E_{s,T1R1} \\ E_{s,T1R1} & E_{s,T1R1} & \Lambda & E_{s,T1R1} \\ M & M & O & M \\ E_{s,T1R1} & E_{s,T1R1} & \Lambda & E_{s,T1R1} \end{bmatrix} \cdot \begin{bmatrix} I_{R1} \\ I_{R2} \\ M \\ I_{Rr} \end{bmatrix} \quad (3.12)$$

Finally, a 3D image of a volume can be generated based on the image E_f at each interrogation (focusing) point within the reconstructing volume.

3.2. Study of Image Resolution

The image reconstruction algorithm developed in the previous section was applied to the case of two (transmitting and receiving) arrays each consisting of 128 (8×16) antennas, with the frequency of 5.2 GHz, while the wavelength in concrete, λ_e , is 25.06 mm. Numerical simulations using analytical measurement data were conducted in order to verify the resolution capability of the system. Two point-like objects were placed with the distance of 25.0 mm along each axis at the center of the reconstructing volume. As shown in [Figure 3.3](#), the results demonstrated that the system, due to the use of bi-focusing (focusing both the transmitting and receiving arrays), is able to achieve a resolution in the order of the wavelength in the dielectric medium, which is 25.0 mm at 5.2 GHz in concrete.



(a) X-direction (b) Y-direction (c) Z-direction

Figure 3.3 Resolution of the system (25mm) at 5.2GHz

3.3. Multi-Frequency Technique

In order to improve the quality of reconstructed image by reducing the background noises, a narrow band multi-frequency technique was applied. In this technique, three or four microwaves with frequencies near the designed illuminating frequency was sent from and received by the antenna arrays. By averaging the images reconstructed from the waves of different frequencies, background noise including the steel interference can be averaged out and the object image can be amplified to improve the signal-to-noise ratio. This technique has been used with some success for similar problems (Pierri et al., 2000, Bucci et al., 2000).

According to the sweeping of frequency, both incident/scattered field and numerical focusing operator become a function of frequency:

$$\begin{aligned}
 E_i(\mathbf{r}_i) &\rightarrow E_i(\mathbf{r}_i, k_{eN}) \\
 E_s(\mathbf{r}_{Rmn}) &\rightarrow E_s(\mathbf{r}_{Rmn}, k_{eN}) \\
 E_f(\mathbf{r}_f) &\rightarrow E_f(\mathbf{r}_f, k_{eN}) \\
 I_{Tkl,Rmn}(\mathbf{r}_f) &\rightarrow I_{Tkl,Rmn}(\mathbf{r}_f, k_{eN})
 \end{aligned} \tag{3.13}$$

where k_{eN} , the effective wave number at the N^{th} frequency.

Then, the electromagnetic image of E_f at $\mathbf{r}_f = (x_f, y_f, z_f)$ can be expressed as

$$E_f(\mathbf{r}_f) = \sum_{N=1}^{N_{Freq}} \sum_{n=1}^{N_n} \sum_{m=1}^{N_m} \left[I_{Rmn}(\mathbf{r}_f, k_{eN}) \cdot \int_V \left\{ I_{obj} \cdot \frac{e^{-jk_{eN}|\mathbf{r}_{Rmn}-\mathbf{r}_0|}}{|\mathbf{r}_{Rmn}-\mathbf{r}_0|} \cdot \sum_{l=1}^{N_l} \sum_{k=1}^{N_k} I_{Tkl}(\mathbf{r}_f, k_{eN}) \frac{e^{-jk_{eN}|\mathbf{r}_{Tkl}-\mathbf{r}_0|}}{|\mathbf{r}_{Tkl}-\mathbf{r}_0|} \right\} dV \right] \tag{3.14}$$

or

$$E_f(\mathbf{r}_f) = \sum_{N=1}^{N_{Freq}} \begin{bmatrix} I_{T1} & I_{T2} & L & I_{Tt} \end{bmatrix} \cdot \begin{bmatrix} E_{s,T1R1} & E_{s,T1R2} & L & E_{s,T1Rr} \\ E_{s,T2R1} & E_{s,T2R2} & L & E_{s,T2Rr} \\ M & M & O & M \\ E_{s,TtR1} & E_{s,TtR2} & L & E_{s,TtRr} \end{bmatrix} \cdot \begin{bmatrix} I_{R1} \\ I_{R2} \\ M \\ I_{Rr} \end{bmatrix} \tag{3.15}$$

where N_{Freq} is the number of frequencies used.

The multi-frequency illumination technique was applied to reconstruct the images of two point-like objects separated 25.0mm, which is the wavelength (λ_e) in concrete at 5.2GHz. Four frequencies of 4.6, 4.8, 5.0, and 5.2GHz were used in the case. When using the single frequency illumination, the largest background noise level was 76.8% of the image, which was reduced to 36.9% after using the multi-frequency illumination technique. As shown in Figure 3.4, the background noise was successfully reduced with the images of the point like objects more clearly reconstructed, when using several frequencies.

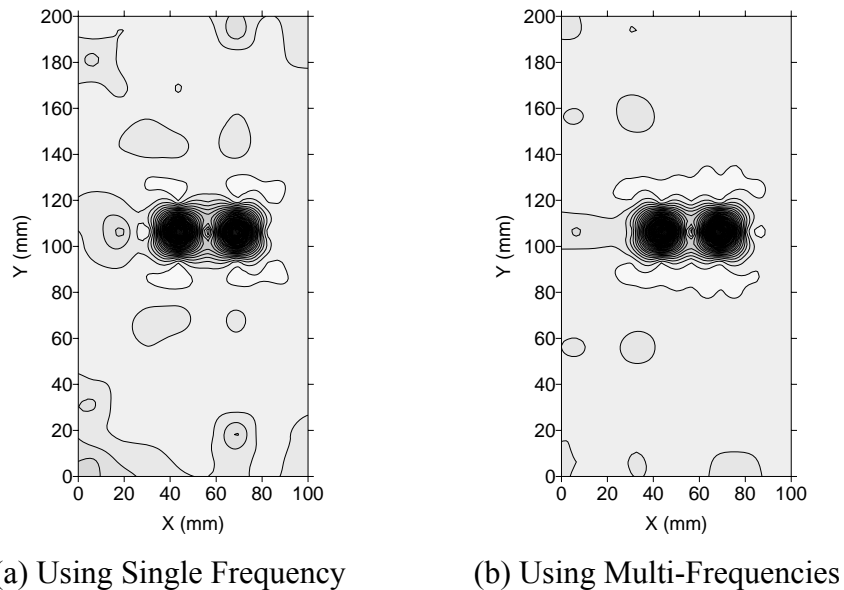
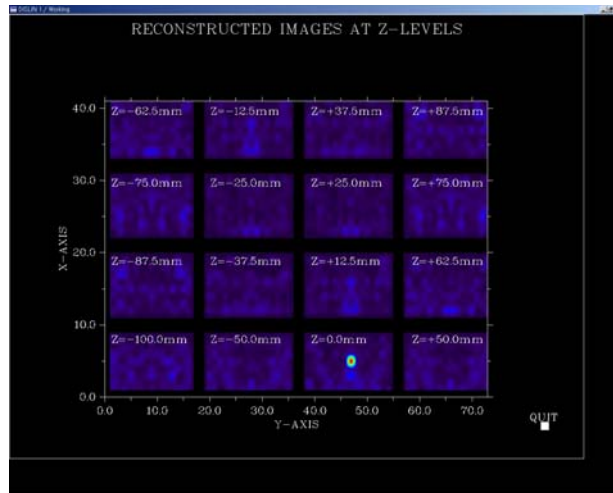


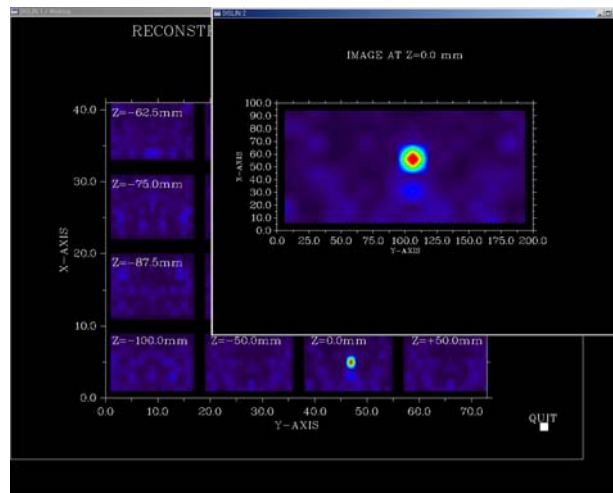
Figure 3.4 Comparison of Single/Multi Illuminating Frequency
(Image of Two Point-like Objects)

3.4. Visualization Software

In addition to the image reconstruction algorithm, a visualization software package was developed for displaying the 3D measurement and assessment results. The software first displays cut images at several vertical locations in the reconstructed volume, and then the user can pick any of the cut images to investigate in detail. Also, the post-process software is integrated with the image reconstruction algorithm and measurement program, which makes it possible to carry out the on-site measurement and assessment within several minutes at most. Figure 3.5 shows an example screen of the visualization software, in which one of the cut images is magnified in a pop-up window.



(a) Several Cut Images along Z-Axis



(b) Magnified Image at Z=0 mm

Figure 3.5 Example Screen Shot of Visualization Software

Chapter 4

HARDWARE DEVELOPMENT

4.1. Prototype I

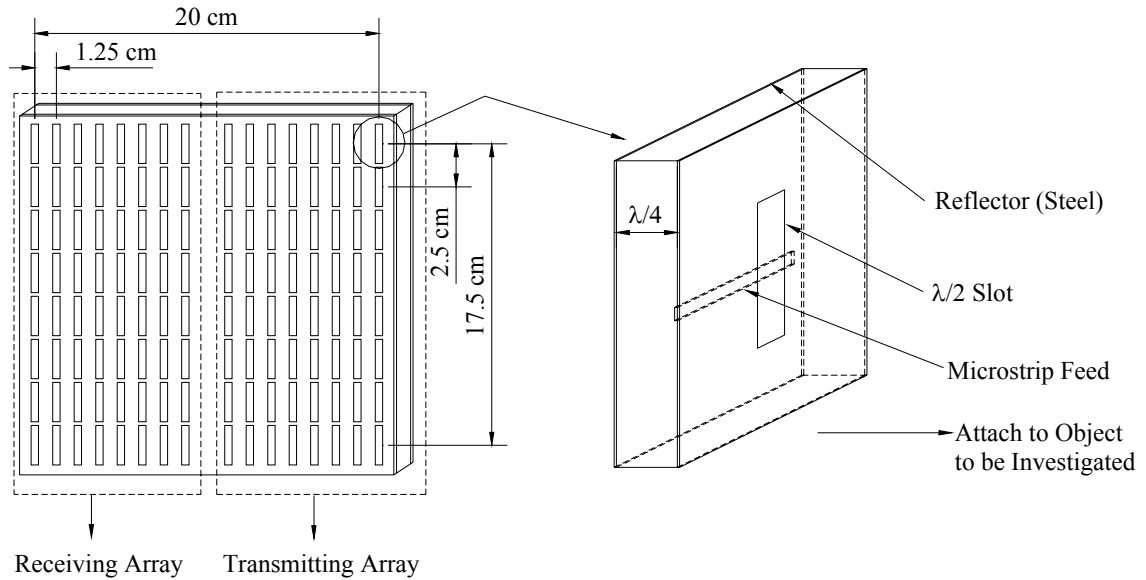
4.1.1. Antenna Array for Prototype I

Prototype I consists of 128 antenna elements placed in two 8×8 matrices. As illustrated in [Figure 4.1](#), the planar rectangular microwave antenna is composed of transmitting and receiving arrays, each consisting of 8×8 slot antennas. Each of these two planar 8×8 arrays consists of a parallel fed 8-element vertical array producing a tomographic focused slice perpendicular to the vertical axis of the structure, and an electronically switched 8-element horizontal array able to focus on a particular point inside the previous tomographic focused slice. The transmitting antenna array focuses the illuminating fields on a particular point inside the volume of investigation and the receiving array focuses the receiving beam on the same point. The whole antenna is a sandwich structure with two metallic grounded substrates separated by a light foam layer. The grounded substrate close to the target concrete structure contains the radiating half-wavelength ($\lambda/2$) slots in the exterior ground plane and the 100Ω microstrip feeding line on the interior side. The second grounded plane, quarter-wavelength ($\lambda/4$) apart from the slot plane, acts as a reflector in order to produce a unidirectional radiation towards the volume of investigation.

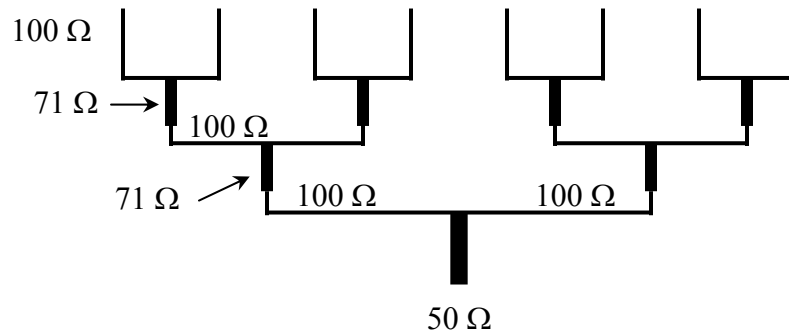
An illuminating frequency of 5.2GHz was chosen as it represents a reasonable tradeoff between the signal attenuation and the image resolution. Due to the use of the bi-focusing technique, an image resolution of 2.5cm can be achieved at 5.2GHz, which is the wavelength (λ_e) in concrete.

A microstrip slot antenna was chosen in order to be directly attached to the concrete surface or the matching cushion. The microstrip slot antenna has the advantage of being able to produce either bi-directional or unidirectional radiation patterns with a large bandwidth. The strip and slot combination offers an additional degree of freedom in the design of the microstrip antenna ([Garg et al., 2001](#)).

At last, the geometry of the slot antenna was determined so as to obtain a wide bandwidth at the resonance frequency of 5.2GHz. The number of antennas (128) and the antenna array dimension of 20cm×20cm were selected as they represent a reasonable tradeoff between the resolution and the reconstructed area covered by the antenna array.



(a) Conceptual Design of Planar Rectangular Slot Antenna Array

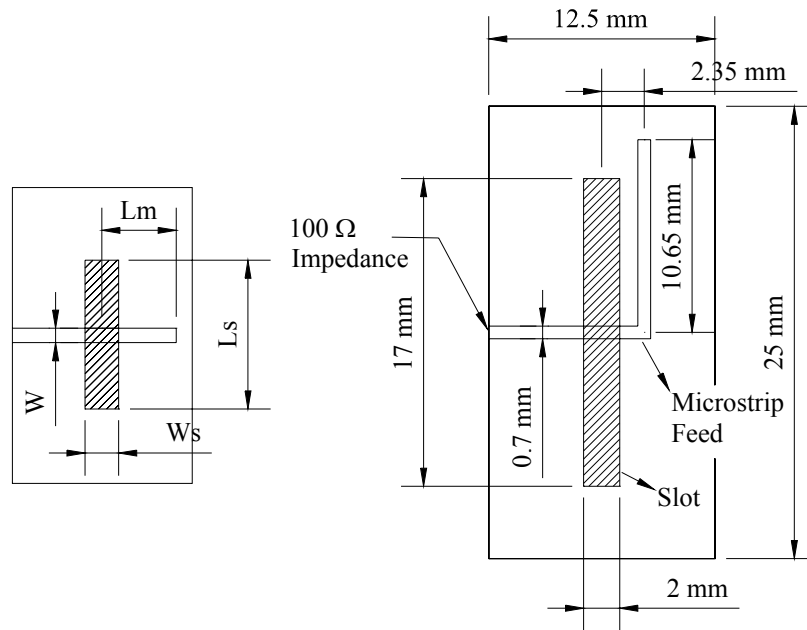


(b) Eight Elements Linear Array with Corporate Feed Configuration

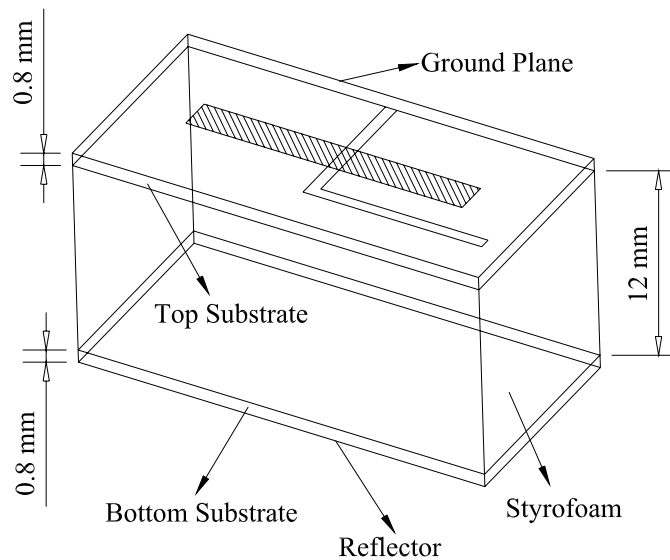
Figure 4.1 Two-Dimensional Planar Rectangular Microwave Antenna Array

4.1.1.1. Single-Slot Antenna Element

Prior to the antenna array design, a single-slot antenna was designed and simulated using Ansoft High Frequency Structure Simulator (HFSS). The geometry of the single-slot antenna is described in [Figure 4.2](#).



(a) Geometry of Single-Slot and Microstrip Feed

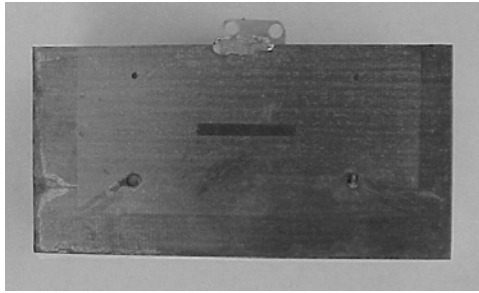


(b) Geometry of Substrates and Foam

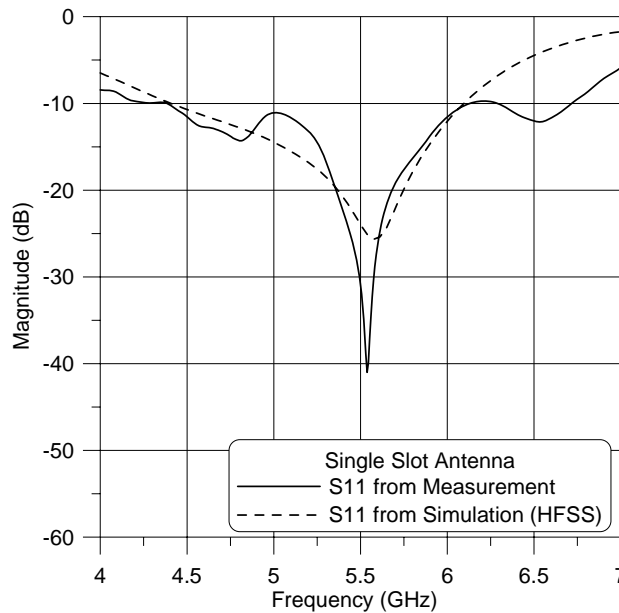
Figure 4.2 Geometry of Single-Slot Antenna

As shown in **Figure 4.2**, a dimension of 12.5 mm \times 25 mm is assigned for each slot. This limitation of the size forces the microstrip feed to be bended. The important factors that can affect the resonance frequency and bandwidth are the length of microstrip feed, L_m , and the length of the slot, L_s . These are adjusted to satisfy the resonant

frequency around 5.2 GHz and a large bandwidth suggested by the simulation results using HFSS. The S_{11} parameter of the designed single-slot antenna is calculated, renormalized with port characteristic impedance of 50Ω and plotted in Figure 4.3 in the frequency range from 4 GHz to 7 GHz. The magnitude of S_{11} at resonance (5.58 GHz) is -26 dB, the one at 5.2 GHz is -17 dB, and the bandwidth at -10 dB is about 1.5 GHz.



(a) Fabricated Single-Slot Antenna Element



(b) S_{11} Parameter of Single-Slot Antenna Calculated Using HFSS ($Z_0 = 50 \Omega$)

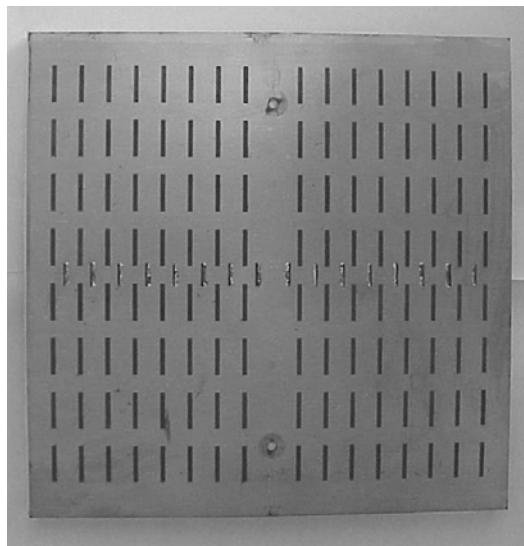
Figure 4.3 Measurement Result of Single-Slot Antenna Element

4.1.1.2. 16×8 Antenna Array

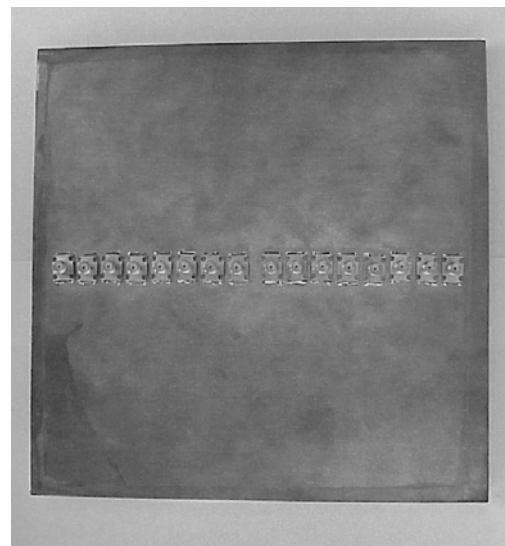
A significant technical challenge in developing the antenna array is to achieve a high radiation performance (meaning a larger bandwidth at the illuminating frequency) and low mutual coupling (meaning low interference among the slot antenna elements).

Although numerous studies have been performed by electrical engineers to study radiation of antenna arrays into air for communication purposes, no literature can be found regarding design knowledge for concrete-radiation antenna arrays.

The antenna array fabricated in this study was tested using a network analyzer, measuring reflection parameters (S_{ii}) for investigating the radiation performance and transmission parameters (S_{ij}) for the mutual coupling. The antenna array was placed on a concrete block, allowing the wave radiating through the concrete. As plotted in **Figure 4.5(a)**, the magnitude of S_{ii} parameters around 5.2 GHz is less than -10dB, implying that the antenna achieved high radiation performance. The transmission parameters plotted in **Figure 4.5(b)** shows that the interference between the co-lateral elements (array 8 and 9) is as low as -20 dB, which is acceptable. Therefore, this study achieved a high-performance antenna array.

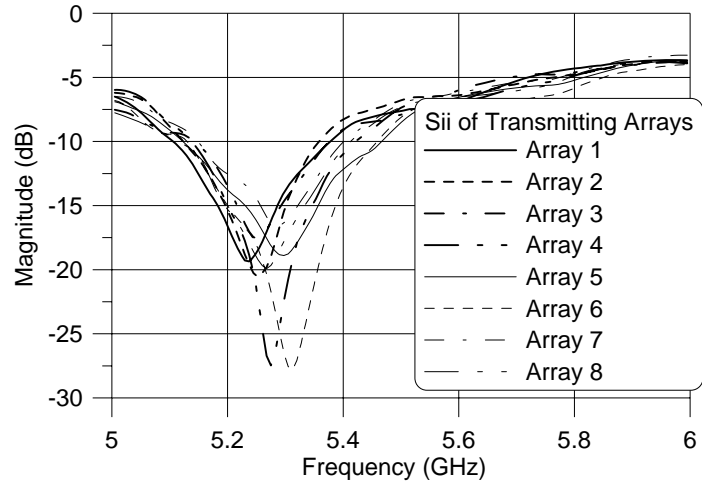


(a) 16×8 Slots

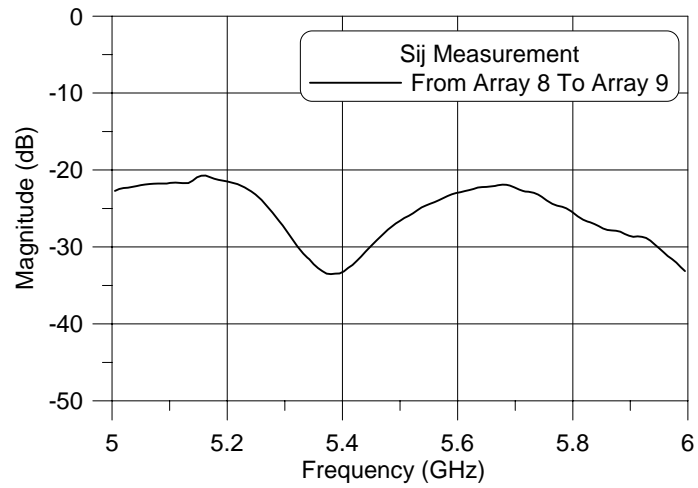


(b) Coaxial Feeds

Figure 4.4 Fabricated Two-Dimensional Antenna Array



(a) S_{ii} Measurement of Transmitting Arrays

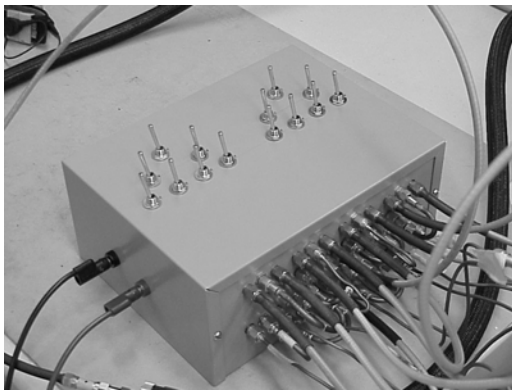


(b) Transmission Measurement (S_{ij} of Array 8 and Array 9)

Figure 4.5 Measurement Results of 16×8 Antenna Array

4.1.2. Control Module for Prototype I

For the reason that the antenna array has 16 coaxial feeds, a switch box is necessary to control the input from and output to the network analyzer. In this study, RF switches, which can control two outputs from one input in each unit with a control voltage of 20V, are used and assembled to make the switch box: there are 8 transmitting ports with one input from the network analyzer, and 8 receiving ports with one output to network analyzer. **Figure 4.6** represents the switch box and a power supply to provide control voltage.



(a) Switch Box



(b) Power Supply

Figure 4.6 Switch Box and Power Supply (Manual Operation)

4.2. Prototype II

Prototype II is a much more sophisticated and ambitious system. Compared to Prototype I, it not only consists of much more antenna elements (256) to cover a larger inspection volume, but also engages much more sophisticated electronic antenna switching controlled by software. The system is composed with a control module, switching unit, antenna array, network analyzer, image reconstruction algorithm, and display unit. The final product to user is the reconstructed sub-surface image under testing, the 3D dielectric profiles of the objects in reconstructing volume. The measurement is performed by electronically switched antenna array and portable network analyzer, which is also controlled by control module. The block diagram in [Figure 4.7](#), describes the connectivity and job flow of the system.

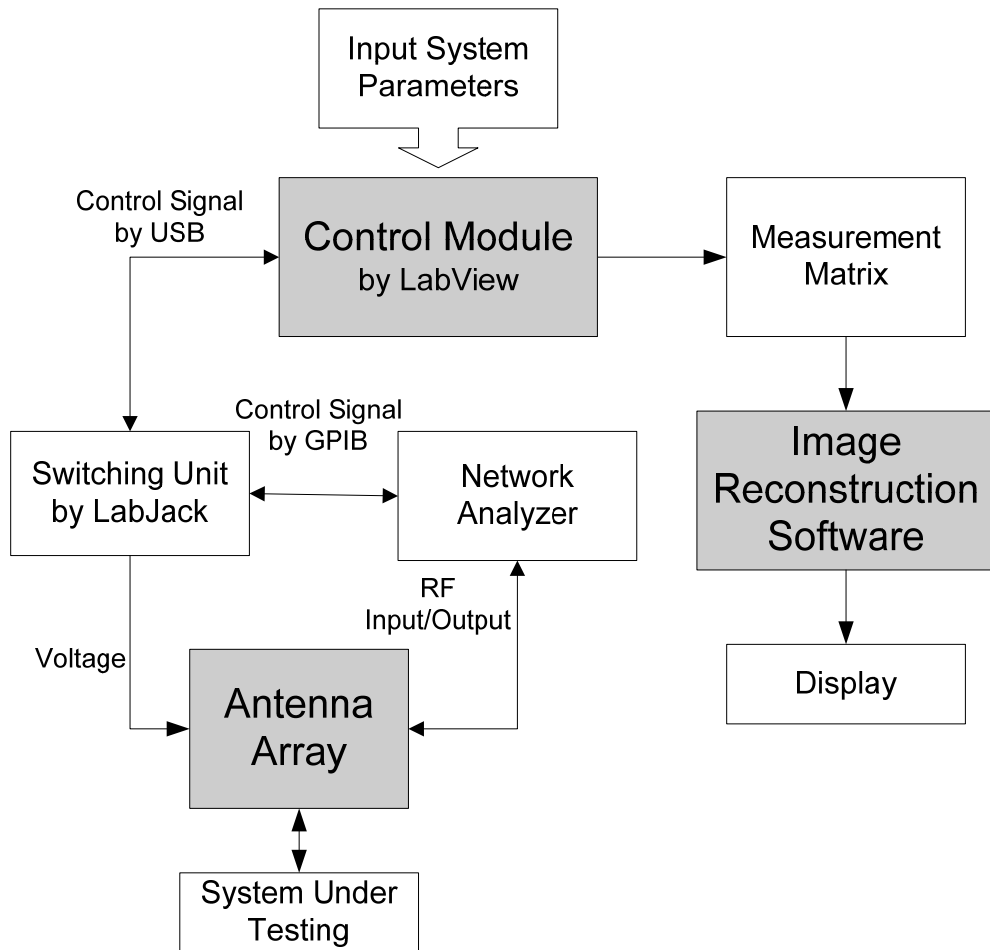


Figure 4.7 Description of Three-Dimensional Imaging System (Block Diagram)

4.2.1. Antenna Array for Prototype II

4.2.1.1. Single-Slot Antenna Element

The illumination frequency on a working medium of concrete ($\epsilon_r = 5.3$) was chosen as 5.2GHz, which again represents a reasonable trade-off between the image resolution and the penetration depth. The type of antenna was chosen as a microstrip-fed single antenna. The entire structure of the slot antenna and its dimension are illustrated in **Figure 4.8**. Two layers of 15-mil-thick Duroid 5880 ($\epsilon_r = 2.2$, $\tan \delta = 0.0009$) are placed on the top and bottom of the foam. The foam used here is Rohacell Rigid Foam by Richmond Aircraft Products whose dielectric constant is nearly unity, which resembles that of air. The thickness of the foam is 12 mm, which is approximately quarter-wave length if the thickness of the top and bottom dielectrics is included. The substrate has two sides of 0.5 oz. of copper layer rolled. The antenna is fed by microstrip line that passes the slot in the middle. The dimension of the microstrip-fed slot antenna was designed and optimized initially to give the impedance matching to 50Ω and operate at 5.2 GHz using Agilent's Momentum. Then, another simulator called High Frequency Structure Simulator (HFSS) was used to check that the two different simulators provide similar, if not identical, results. The width of the microstrip feed was chosen to yield 50Ω transmission line.

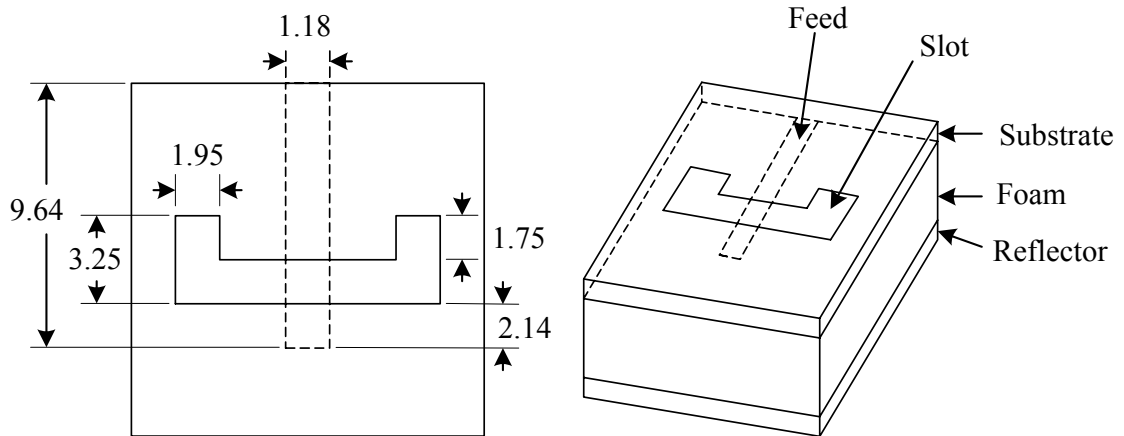


Figure 4.8 Structures and Dimension of Single-Slot Antenna Element

The slot was modeled as “magnetic wall,” which is frequently used to approximate the holes in electromagnetic simulation. In addition, more boundary condition such as perfect electric field for the ground plane was applied to reduce the simulation time. The comparison between simulation result using HFSS and measurement is shown in Figure 4.10. The plot shows that simulation resonates at 5 GHz with the return loss of -20 dB while the measurement’s resonant frequency is at 5.2 GHz with the return loss of -21 dB. Very good consistency between the simulation and measurement results exist in both resonant frequency and return loss of the antenna. The -10 dB bandwidths are 13.5% and 11.5% for the simulation and the measurement respectively.

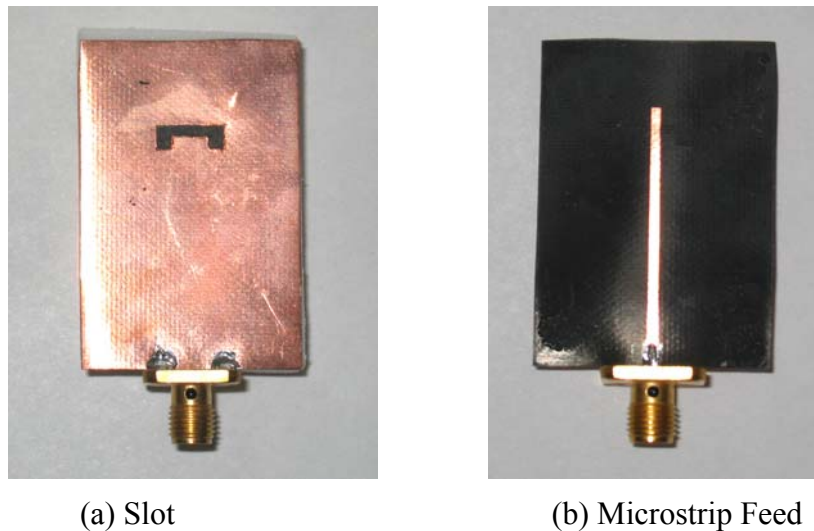


Figure 4.9 Single-Slot Antenna Element

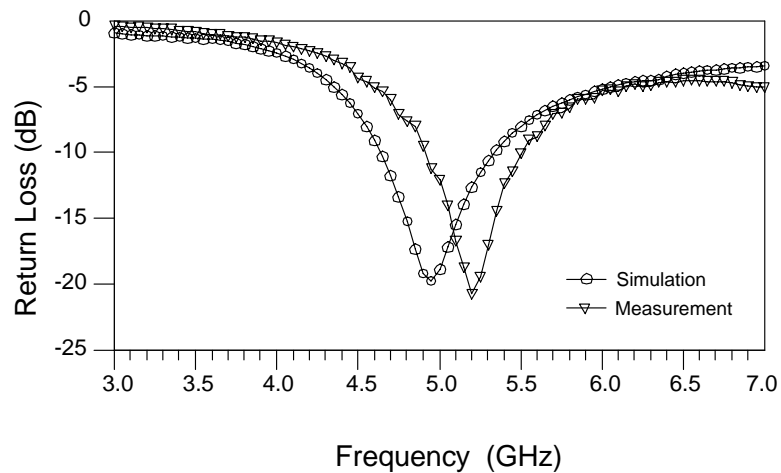
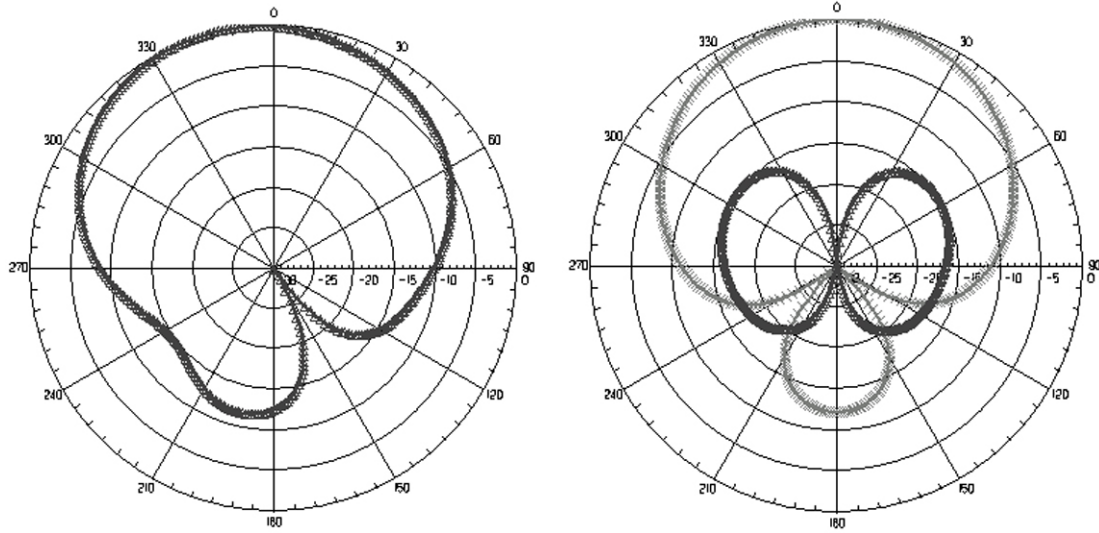


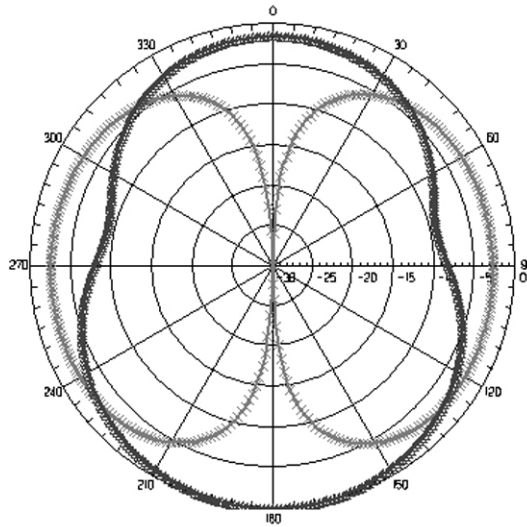
Figure 4.10 Comparison Between Simulation and Measurement Result

The simulated radiation patterns of different polarization at different cuts are shown in **Figure 4.11**. Also, HFSS was used for the simulation. Each plot had been normalized to its maximum electric field and contains electric fields in both phi and theta directions. The line with \times marks is E_{phi} and the line with Δ marks represents E_{theta} . E_{phi} at $\varphi = 0^\circ$ is almost negligible, but E_{phi} is dominant at $\varphi = 90^\circ$.



(a) E_{phi} and E_{theta} at $\varphi = 0^\circ$

(b) E_{phi} and E_{theta} at $\varphi = 90^\circ$



(c) E_{phi} and E_{theta} at $\theta = 90^\circ$

Figure 4.11 Radiation Pattern of Slot Antenna

4.2.1.2. PIN Diodes

The individual antenna element in three-dimensional array was designed to be activated by switching using PIN diodes. Three different types of diodes were evaluated to find the most suitable diodes; Agilent's HSMP-389F, HMPP-3895 and Microsemi's MPP-4203 come in different packages and material. HSMP-389F is SOT-323 type. HMPP-3895 is specially packaged in MiniPak[®] without lead pins but with gold pads at the bottom. These two diodes are in common cathode configuration. Two PIN diodes share cathode in one package. MPP-4203 is in 0204 package and therefore the smallest. This diode, however, contains only one diode in each package.

For the measurement, 50-Ohm microstrip line was fabricated using the same dielectric used for the antenna with the center of the line open-circuited for diode mounting. Then, the through-line was de-embedded mathematically for more accurate measurement. Bias voltage of 0.9 volt was applied to the diode. The test fixture and de-embedding through line are shown in [Figure 4.12](#).



(a) Test Fixture



(b) De-embedding Fixture

Figure 4.12 Test and De-embedding Fixture

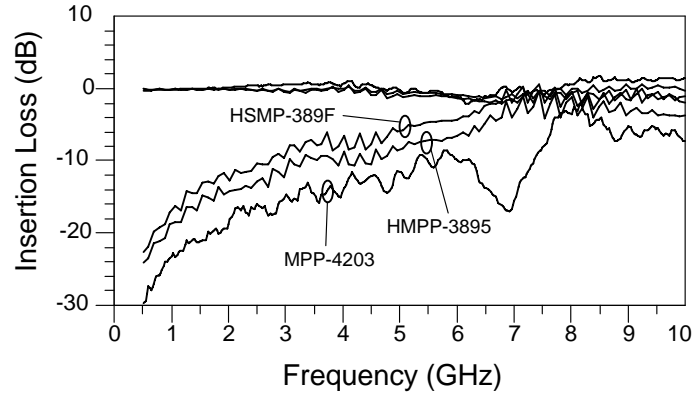


Figure 4.13 Measurement Comparisons of PIN Diodes

The measurement results of three different types of diodes are compared in **Figure 4.13**. The sudden drop in the MPP-4203's measurement between 6 GHz and 8 GHz could be removed by performing calibration procedure more carefully. MPP-4203 shows the most promising isolation at 5 GHz. Although insertion losses are very closely spaced to each other, MPP-4203 suffers from the lowest insertion loss of all. Insertion loss is 0.3 dB while the isolation is nearly 12 dB.

Figure 4.14 shows the dimension of the MPP-4203. The largest dimension is only 1 mm with the rest being sub-millimeter.

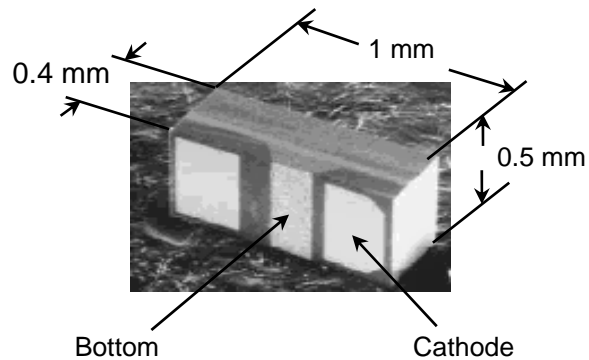
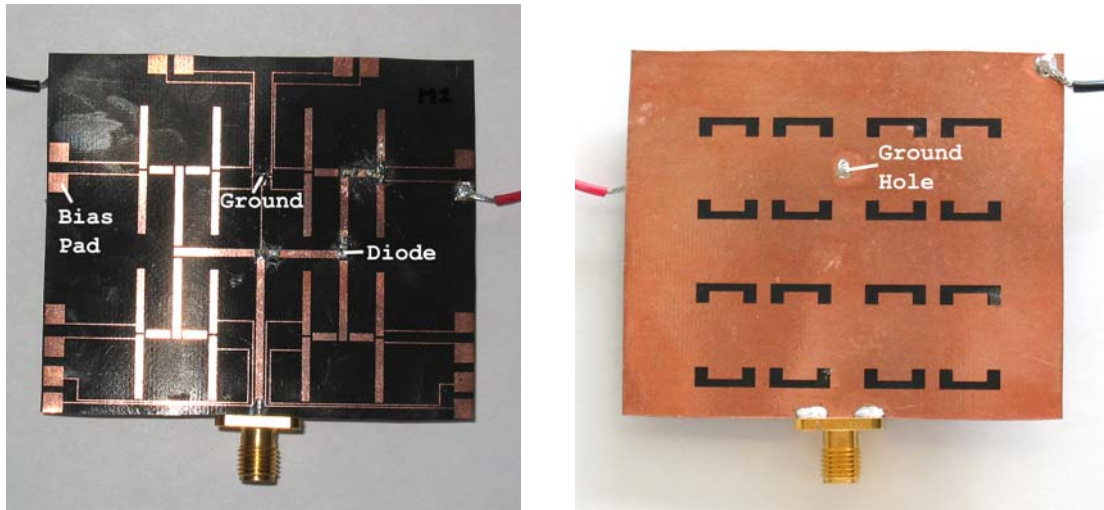


Figure 4.14 Dimension of PIN Diode (MPP-4203)

4.2.1.3. 4×4 Antenna Array

At first, a preliminary 4 by 4 antenna array was fabricated and real diodes were soldered onto the substrate as shown in [Figure 4.15](#) to verify the simulation results. The design of the 4×4 antenna array can be directly expanded to the whole array, or can be a sub-module of the whole array, i.e. the whole array consists of sixteen 4×4 modules. [Figure 4.16](#) shows the layout of the ground and ground pad. In the middle of the ground pad, via was created by drilling a hole connecting the via pad to the ground. Only four PIN diodes were used to turn on one antenna element. Via is located approximately 1 mm above bias line as shown in [Figure 4.16](#). Bias pads were located along the periphery of the substrate square.



(a) Feed Network with Bias Pads

(b) U-shaped Slots

Figure 4.15 Fabricated 4 by 4 Antenna Array

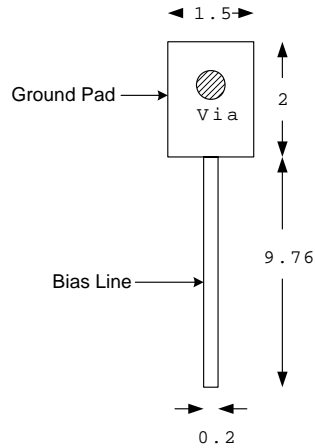


Figure 4.16 Layout of Ground

Figure 4.17 shows two measurements of the array: when all the four diodes are turned on and off. DC voltage of 3.6 V and 20 mA DC current was applied to the antenna array. Across each diode, roughly 0.9 V was applied. This bias can turn on four diodes at the same time, establishing low impedance path to the input port. The resonant frequency was 4.94 GHz and return loss was -36 dB when all the diodes were turned on. When they were off, return loss was -0.03 dB at 4.94 GHz. PIN diodes exhibited very good isolation at off state. The -10 dB bandwidth was approximately 11.3 %.

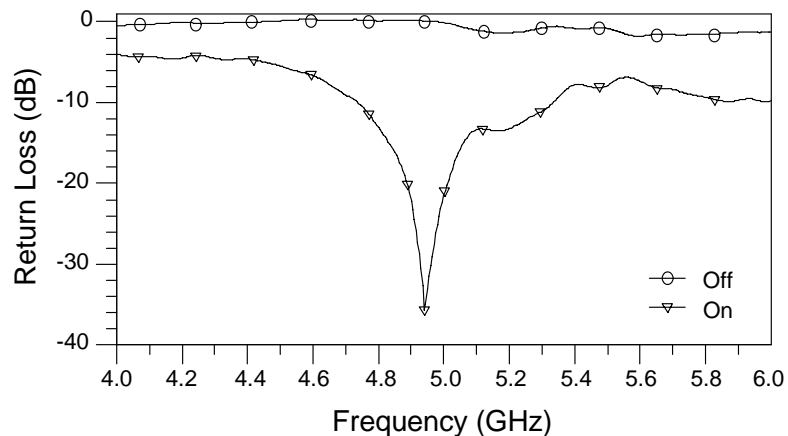


Figure 4.17 Switching Behavior of Antenna

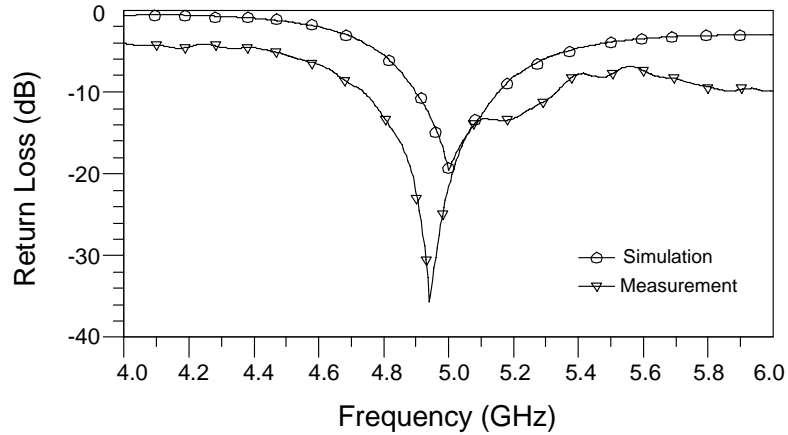


Figure 4.18 Comparison Between Simulation and Measurement

Figure 4.18 shows the comparison between the simulation result using Momentum and measurement. Very good agreement was observed between them. Simulation result indicates the resonant frequency at 5 GHz with the return loss of roughly -20 dB. Also, Figure 4.19 compares the array's return loss when diodes were applied with bias and microstrip lines replaced the diodes. In the gap where diode was to be soldered across, a small piece of copper tape was placed. Both lateral and vertical dimensions of tape resembled that of the diode. The diode's parasitic capacitance at on state slightly brought down the resonant frequency of the array.

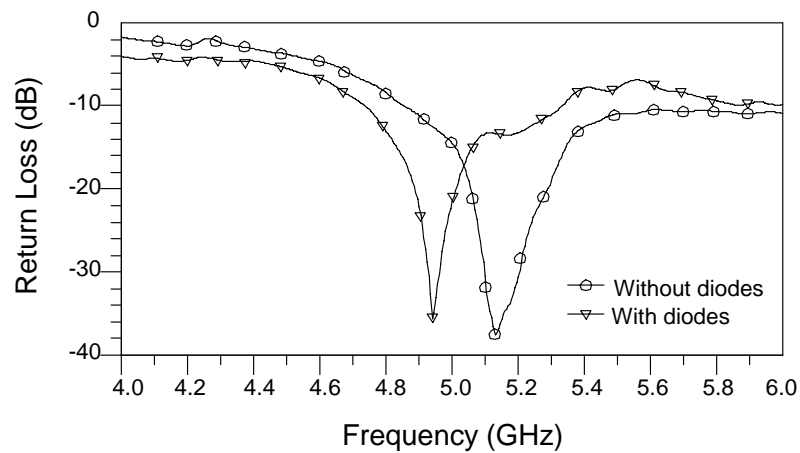


Figure 4.19 With & Without Diodes

Diodes' applicability to microwave imaging was also checked. To do so, the set-up in Figure 4.20 was used to test if the receiving antenna array was able to accept any power from the transmitting horn antenna or vice versa. A rectangular concrete block was inserted between the transmitting and receiving antenna with certain dimension. The broadband receiving horn antenna was verified experimentally that it operates at 5.2 GHz with concrete block before performing the measurement. The dimension of the horn antenna used is illustrated in Figure 4.21. Only part of input power that was transmitted through the horn antenna would be received by the antenna array, more likely activated antenna element.

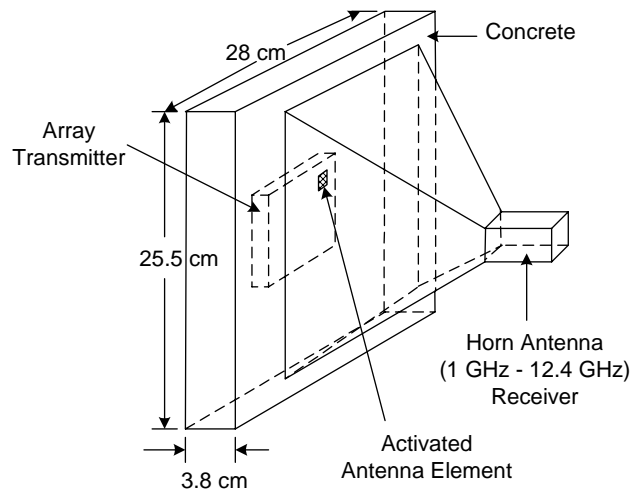


Figure 4.20 Measurement Set-Up for Insertion Loss

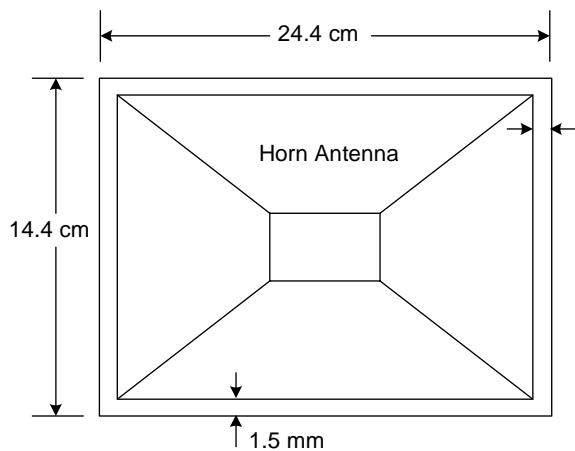


Figure 4.21 Horn Antenna Dimension

Theoretical fraction of this received power by the activated slot antenna element can be easily derived from the following expression:

$$S_{21} = 10 \log \left[\frac{\left(\frac{\lambda}{2}\right)^2}{9.4\lambda * 5.5\lambda} \right] = -23dB \quad (4.1)$$

The denomination within bracket is the dimension on the horn antenna expressed in wavelength, assuming the wavelength within concrete is 26 mm at 5 GHz. The experimental result is shown in [Figure 4.22](#), where the peak value corresponds to -18 dB at 5 GHz. The difference between theoretical and experimental values was 5 dB or 22 %. The general behavior illustrated in [Figure 4.22](#) confirms that the antenna array is capable of receiving or transmitting power from or to its counterpart.

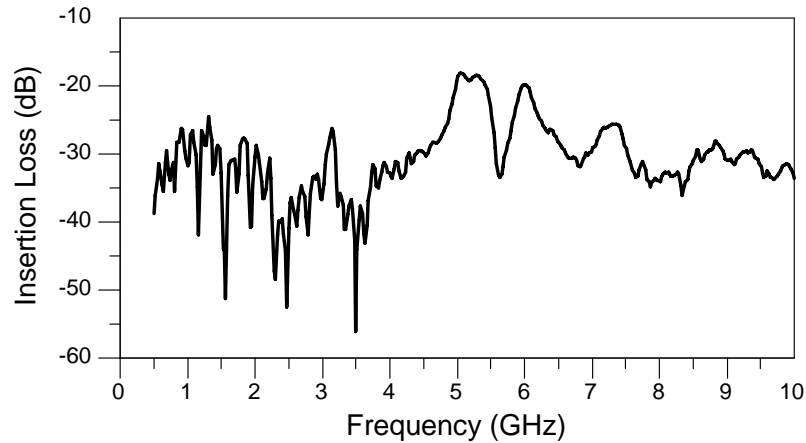
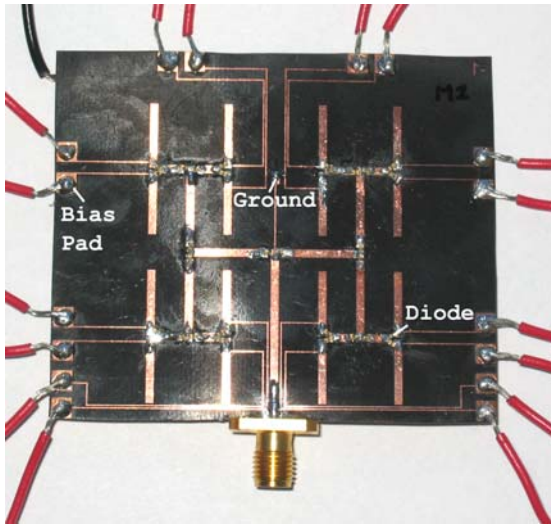
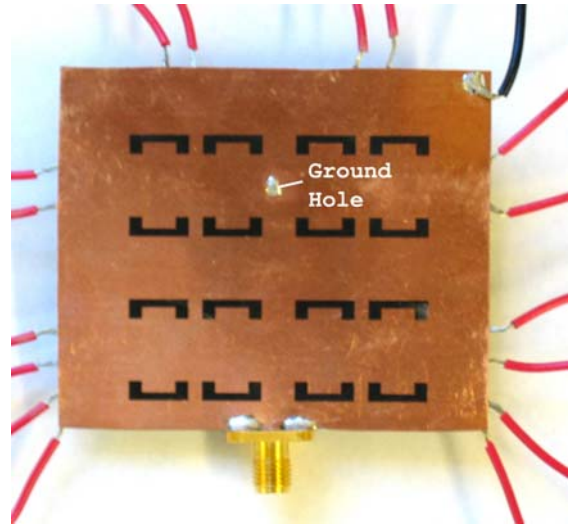


Figure 4.22 Measurement Result

After the successful performance of the preliminary antenna array, all of the sixteen slot antenna elements were loaded with PIN diodes for a final test. The total of thirty diodes was surface-mounted as shown in [Figure 4.23](#). The same bias condition was used as before: 3.6 DC voltage that supplies 20 mA DC current. Four diodes are supplied with bias at a time to establish low impedance RF path from the input port to the microstrip slot antenna.



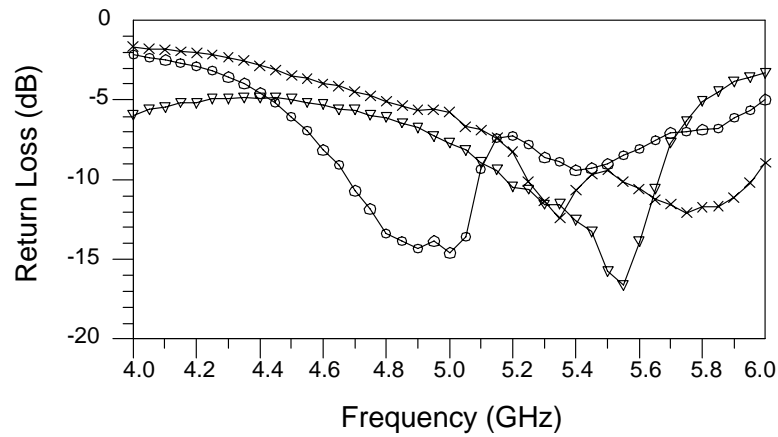
(a) Feed Network with Bias Pads



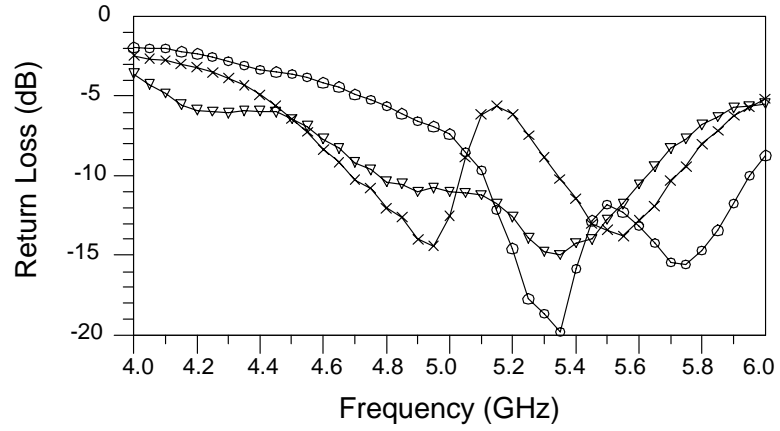
(b) U-shaped Slots

Figure 4.23 Complete Slot Antenna Array

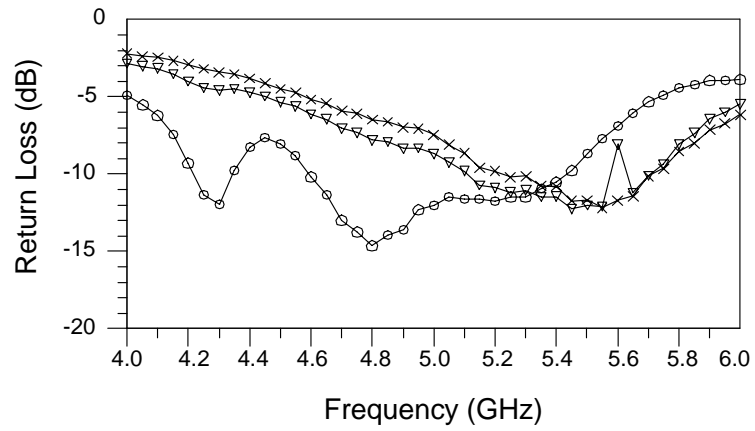
The measurement result is shown in [Figure 4.24](#). Due to the numerous measurements, the set of three measurements are grouped for each plot for better visibility. The results look different from that of the preliminary array, where only four diodes were used. As each antenna element turns on, it produces different resonant frequency and return loss. Also, the measurements reveal that the antenna element sometimes behaves as a dual-band antenna resonating at two adjacent frequencies.



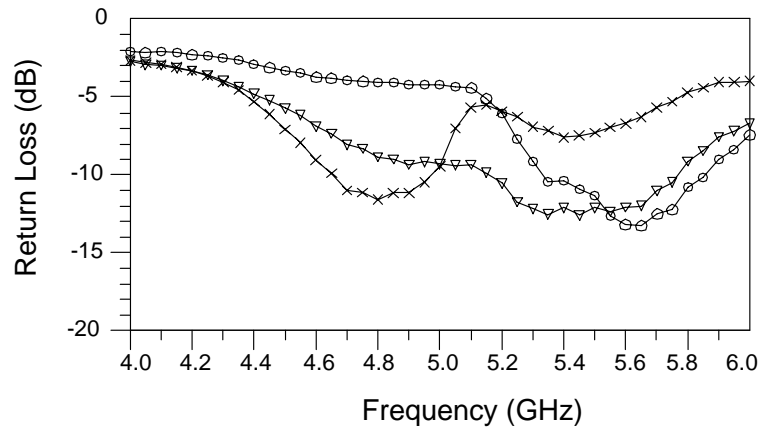
(a)



(b)



(c)



(d)

Figure 4.24 Measurement of Each Antenna Element

4.2.1.4. 16×8 Antenna Array

The 4×4 antenna array was duplicated to produce a final array which has 16×8 (256) antenna elements. The dimension of the slot and microstrip feed network is preserved except for the location bias ground and thin bias lines. Both [Figure 4.25](#) and [4.26](#) shows each of two surfaces of the final array with 256 elements. The final array consists of 8 unit cell (4×4 antenna) arrays. Each unit cell array was added with additional microstrip lines for feeding and the gap for PIN diodes. The bias ground was moved closer to the input port at the bottom. At both sides of the array, the bias lines were arranged in such a way to accommodate total number of 4 ribbon connectors, which would be connected to the control box that control the sequence of switching diodes. Only 32 out of 37 pins are used for controlling diodes with the pin at the lowest bottom being ground. This array would require 480 PIN diodes surface-mounted. The lateral and vertical dimensions are 204.8 mm and 237.6 mm respectively, which is slightly smaller than the letter-sized printing paper.

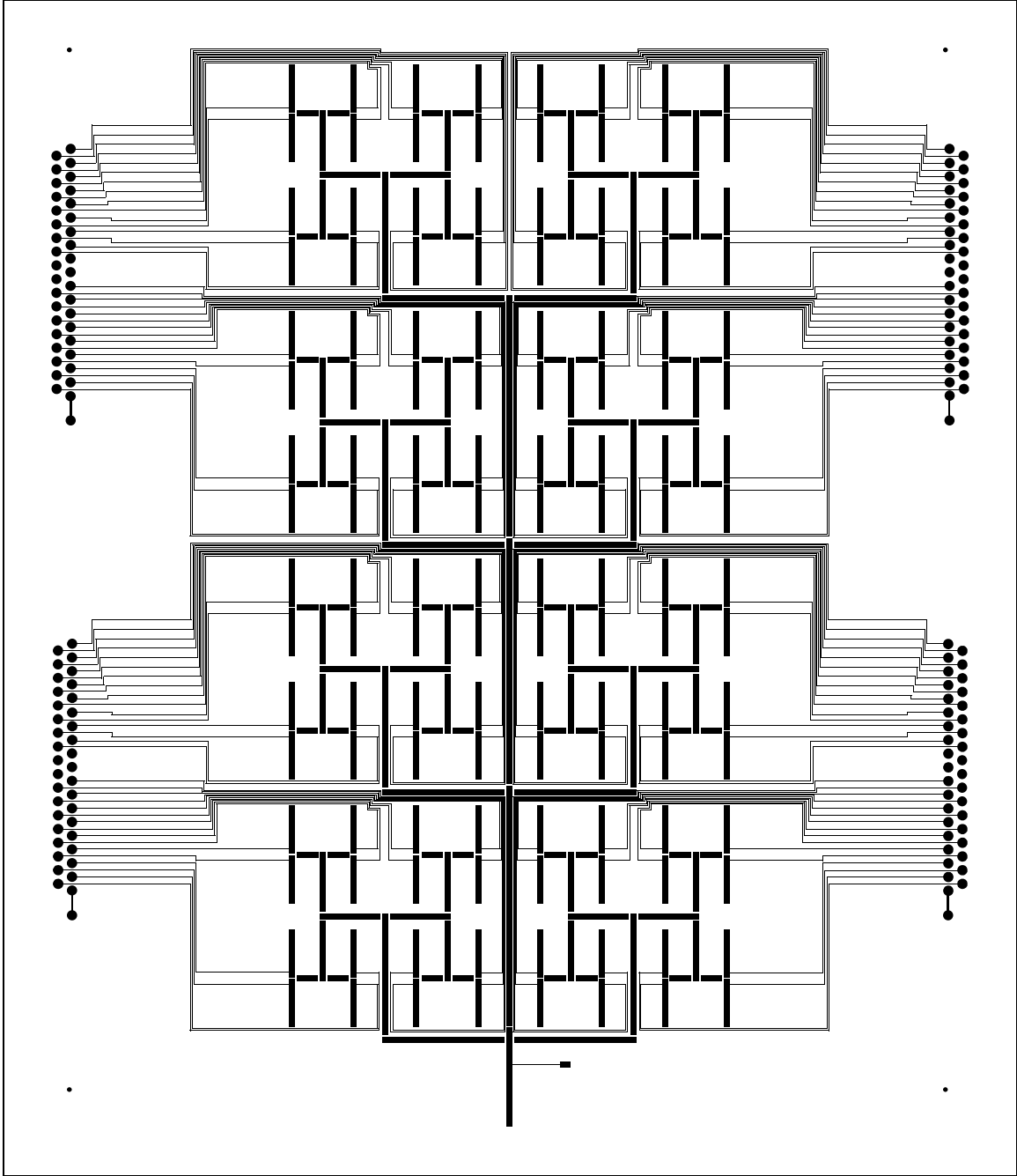


Figure 4.25 Final Array with Feed Network and Bias Lines

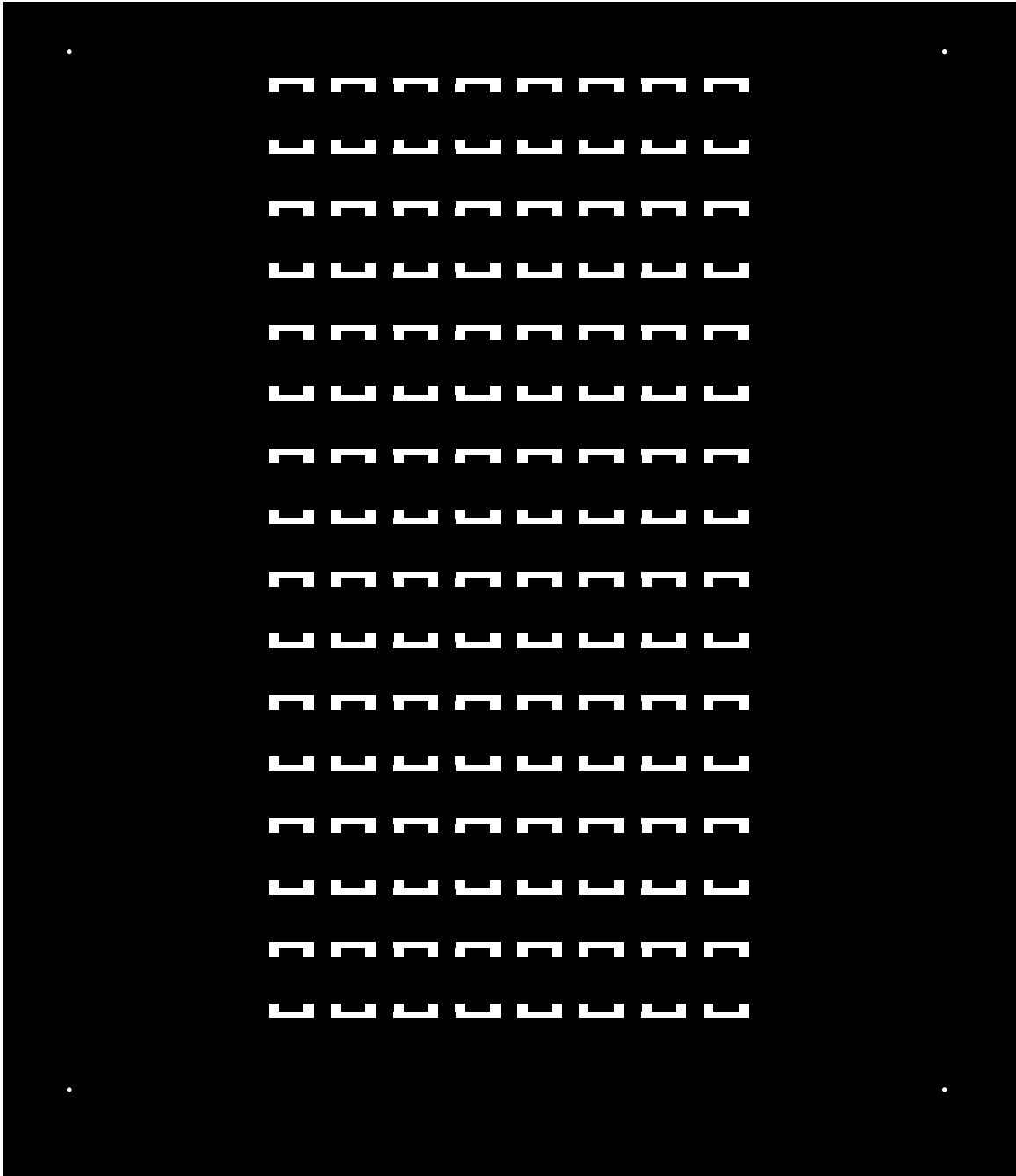


Figure 4.26 Final Array with Slots

Power transfer was also investigated to examine how well the power applied to input port is being transferred to the antenna. [Figure 4.27](#) shows the lay-out of an antenna assuming that it is on with the rest of the diodes perfectly open-circuited. The diodes that turn on are treated as perfect conductor to ignore the effect of the diodes. The overall circuit is treated as two-port with the input being first port and the end of bias line

being second port. The simulation result in Figure 4.28 indicates that roughly 1/3 of input power leaks to the bias line, which should be avoided.

To solve this problem, two possible solutions are suggested: half-wave short stub and quarter-wave open stub. The idea is to make the impedance of the bias line ideally infinite so that bias line is as if it is not there at all. These will be discussed in the following.

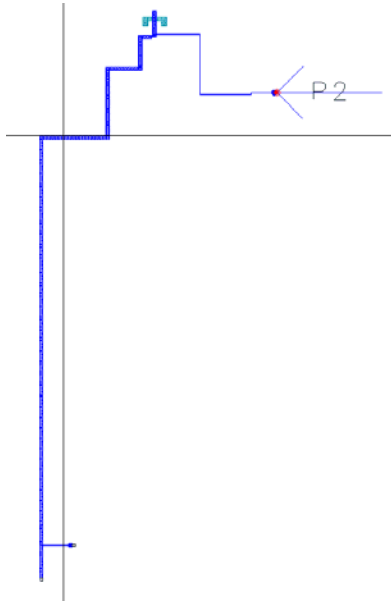


Figure 4.27 Original Layout

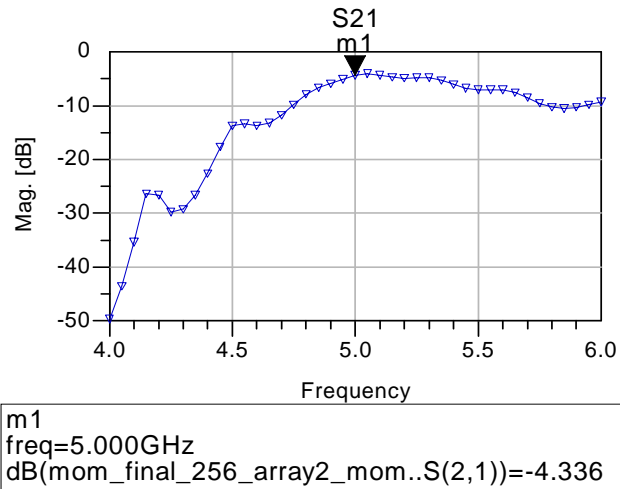


Figure 4.28 Simulation Result

Solution I: One possible solution to eliminate this power leakage through the bias line could be the addition of the quarter-wave long short stub at half-wavelength away from the microstrip feed of the slot antenna. Figure 4.29 shows the scheme of the possible solution. The simulation result is in Figure 4.30. S_{12} , the power that is transferred to the bias line, is significantly reduce to under -20 dB up to 5.4 GHz.

The entire geometry from the input to the antenna implementing this possible solution is drawn in Figure 4.31 and simulation is performed as in Figure 4.32. Once again, power leakage through bias line is acceptable, less than -20 dB at the operating frequency of the antenna.

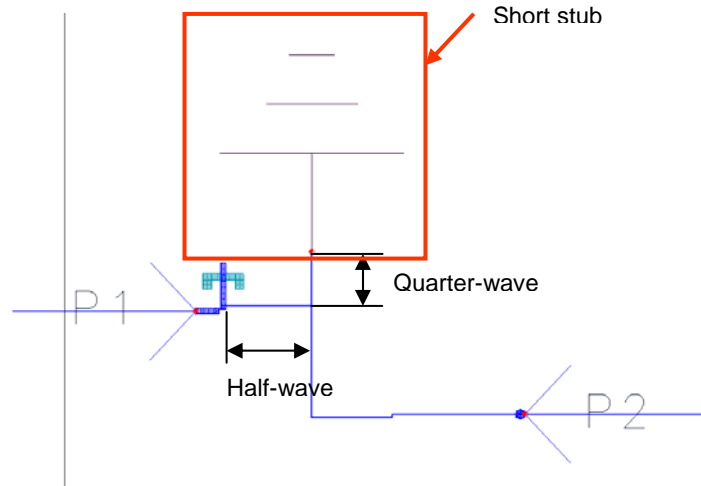


Figure 4.29 Solution I

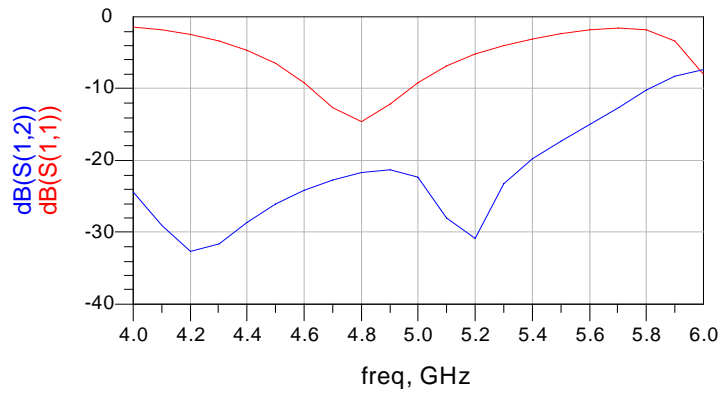


Figure 4.30 Simulation Result

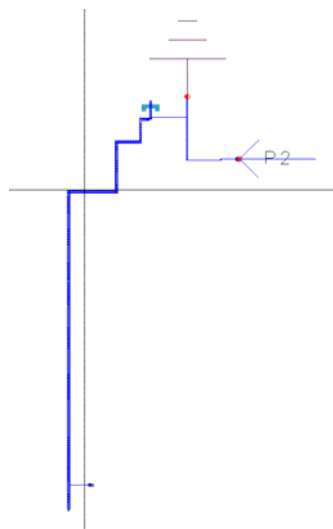


Figure 4.31 Entire Array with Solution I

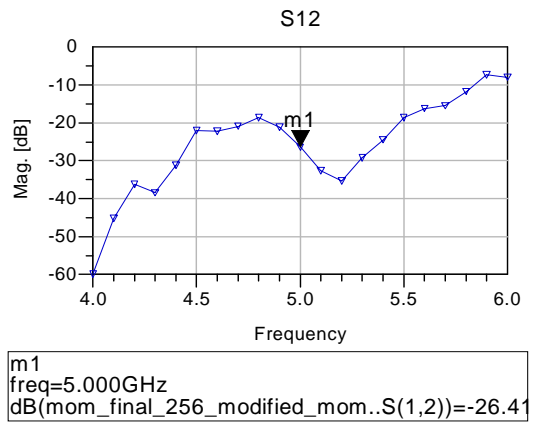


Figure 4.32 Simulation Result

Solution II: Another possible alternative is adding the quarter-wave long open stub quarter-wave away from the microstrip feed as illustrated in Figure 4.33. Figure 4.34 shows the simulation result. Power leakage, S_{12} , is even smaller than solution I, smaller than -50 dB up to 5.3 GHz.

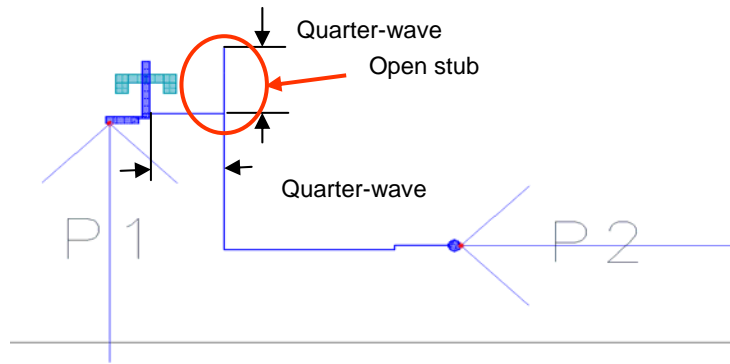


Figure 4.33 Solution II

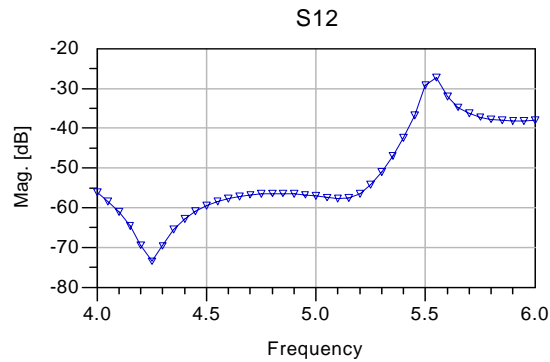


Figure 4.34 Simulation Result

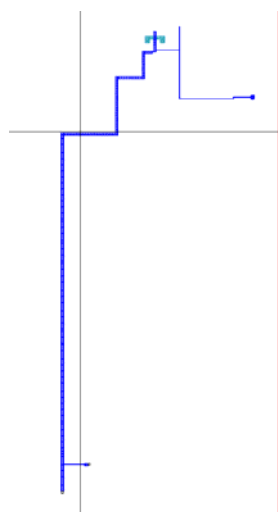


Figure 4.35 Overall Array with Solution II

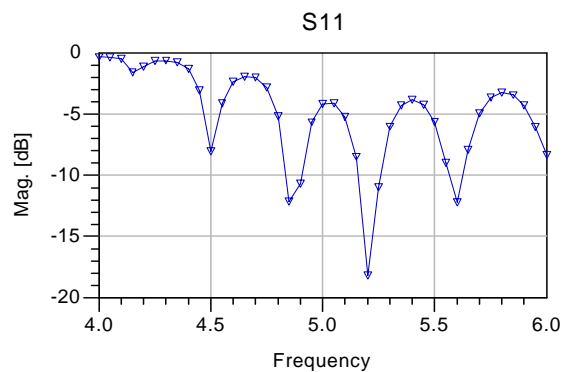


Figure 4.36 Simulation Result

Entire array with solution II is simulated to check if the addition of quarter-wave open stub has any effect on the performance of the antenna. **Figure 4.36** proves that this open stub has no effect: antenna still radiates at 5.2 GHz. This scheme may sound more attracting than the first solution due to the ease in the fabrication since open stub does not require drilling holes to create ground.

4.2.2. System Integration

The system integration is in charge of the control module, switching unit to control network analyzer to generate the measurement data. The white blocks in the block diagram, as shown in **Figure 4.7**, will be addressed for the system integration. The programming details will be showed and the hardware setup will be also described.

Since the antenna array is designed to have 128 bias lines for each transmitting or receiving end, the key thing is to 1) address antennas by controlling analogue voltage output sequentially; 2) take the measurement data from network analyzer. The idea of the first step is that the only one transmitting antenna and one receiving antenna is activated during each measurement time, which requires only one analogue voltage is high out of 128 biasing lines for transmit antennas. For the receiving antennas, the same idea can be applied as the case of transmitting antennas. Then the task is transformed into controlling the output analogue voltage so that only one is high out of 128. The first step turned into designing a 1:128 switch given a common analogue input. **Figure 4.37** shows the intergrated system with labtop and control module.

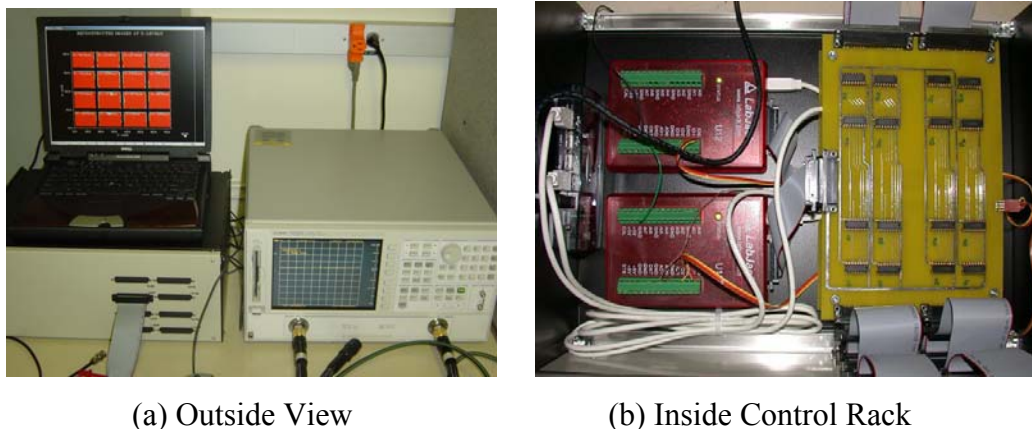


Figure 4.37 Integrated System with Control Rack, Laptop, and Network Analyzer

4.2.2.1. Construction of Measurement Matrix

The image reconstruction algorithm needs a measurement matrix to generate a reconstructed image. The elements of the measurement matrix are scattered fields measured at receiving antenna, and each of them has the index associated with the number of transmitting and receiving antenna; the number of row and column of each element corresponds to the one of transmitting and receiving antenna, respectively.

Since the system has a large number of antennas as transmitting and receiving elements, the best case to address each antenna sequentially is to have 2 loops with receiving antennas as the inner loop while transmitting antennas are swept as the outer loop. In this way, each antenna will be addressed accordingly so that the data will be constructed as a measurement matrix. As a complete program, initialization of the system is always required before the measurement is taken. Plus the request of complete data set is putting the image algorithm right after the measurement is done.

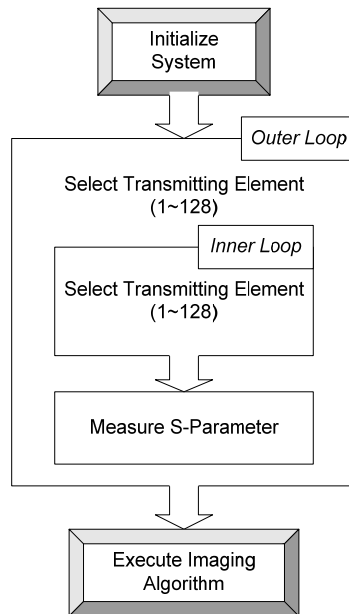


Figure 4.38 Schematic of Algorithm for System Integration

4.2.2.2. Component Details

In order to take the measurement data, a computer program is executed in the computer so that this procedure is going to be done automatically. Since the design of the antenna is requiring the analogue voltage, external hardware except the computer would be implemented to provide it. A brief introduction of the software and hardware is given. The details of each components and protocols are included at [Appendix C](#).

Control Module: The LabView 6i (www.ni.com) was used to control the whole system. The LabView is a graphical programming language, which provide a nice interface and many drivers for various instruments are available. In order to measure the signal, it is needed to control the network analyzer and also to control the analogue voltage for addressing antenna. This procedure requires a program to be able to control both of them. Therefore, the LabView is chosen to fulfill this target.

Switching Unit: The LabJack and Texas Instruments Multiplexers were used for switching unit. LabJack has a number of analogue I/Os as well as digital I/Os, which are needed in controlling voltage output. It also has a good price to quality ratio and nice interface. Features used were 1 Analog Output and 25 D-sub I/O connectors, including 16 signal outputs as well as surface mount digital outputs. The maximum frequency of digital output is 50Hz. Data sheet is available at www.labjack.com.

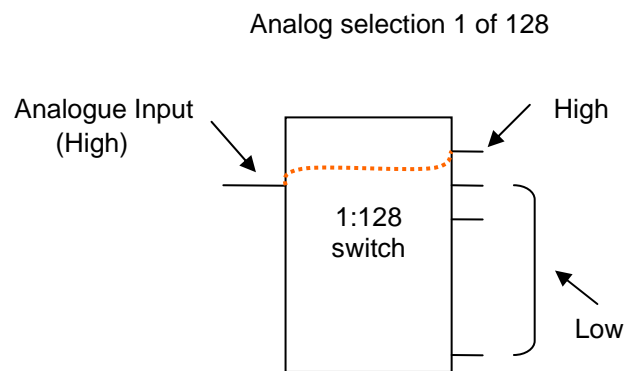


Figure 4.39 Demo Model of 1:128 Switch

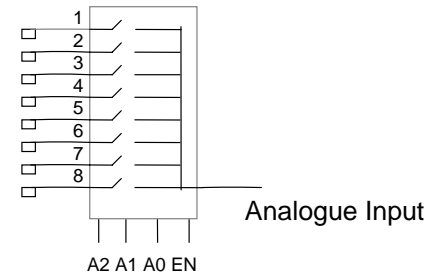
In order to control one output voltage out of 128 lines, the generalized switch 1:128 is needed. The demo model is showed in [Figure 4.39](#). However, no manufacturer

makes it, while 1:8 switch is used frequently. The project team built the 1:128 switch based on 1:8 switch, and 16 switches were needed. The switch is chosen as Texas Instruments Multiplexers CD74HC4051E.



Figure 4.40 Texas Instruments Multiplexers CD74HC4051E

The functionality of this analogue multiplexer/switch is that only one output of 8 ones is equal to the common input voltage. By using the enable line, the switch could be disabled, with the analytic function in [Figure 4.41](#).



Address line and Enable line for 1:8 Switch

Figure 4.41 1:8 Switch

In order to make the 1:128 switch, 16 1:8 switch are used and each enable line are connected with D-sub 25 connector to LabJack digital outputs. The 16 digital outputs are programmed so that one of them is low to enable one of 16 chips active; the rest 15 outputs are high, so respectively the 15 chips are disabled. 3 selected address lines are connected with LabJack surface mount digital outputs. For each combination of 3 digits, one of 8 outputs is selected to have the same voltage as the common input, for all of common inputs of 16 chips, they are wired to 5V analogue voltage output of LabJack. In this way, 1 of 128 switching is realized and the analogue voltage only activate one antenna element by applying analogue voltage, while the rest are disabled. [Figure 4.42](#)

shows 1:128 switch, the yellow color shows the analog voltage flow: 1 of 16 D sub digital outputs is low with the rest of outputs maintaining high voltage, resulting only one chip activated. As the same time, 3 surface mount digital outputs, IO0 IO1 and IO2, are selecting 1 of 8 outputs of this chip. Therefore, 1 of 128 bias lines has high analog voltage with the rest having no voltage and one antenna is working due to the bias voltage applied. Then the 1:128 switch is achieved. 2 sets of switches are used in order to control both transmit and receive ends.

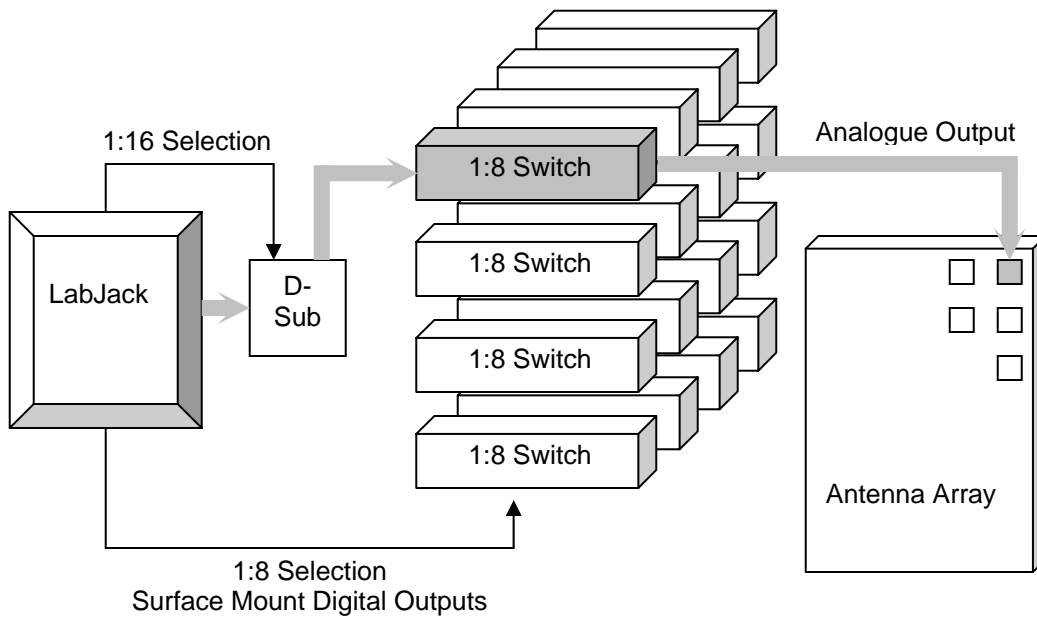


Figure 4.42 Practical Model of 1:128 Switch

4.2.2.3. Control Program

The LabView program followed the schematic of [Figure 4.38](#) exactly. Starting with initializing the system, the measurement part is in the middle, then finally ending with running the image reconstruction algorithm to construct the pictures showing the concrete conditions.

The network analyzer is initialized at frequency 5.2 GHz, which is the working frequency of the antenna arrays with the 3 minimal points of measure. [Figure 4.43](#) shows one of the “frames” in LabView to take the measurement data. There are 4 loops; (1)

transmit parts outer loop 16 times for chip selection, (2) transmit parts inner loop 8 times for outputs of single chip, (3) receive parts outer loop 16 times for chip selection, and (4) receive parts inner loop 8 times for outputs of single chip. Obviously it closely corresponds to the practical model of 1:128 switch. The content inside the most inner “frame” shows the procedure of taking the measurement data of S parameter from network analyzer and save it to file ‘mdata.o’

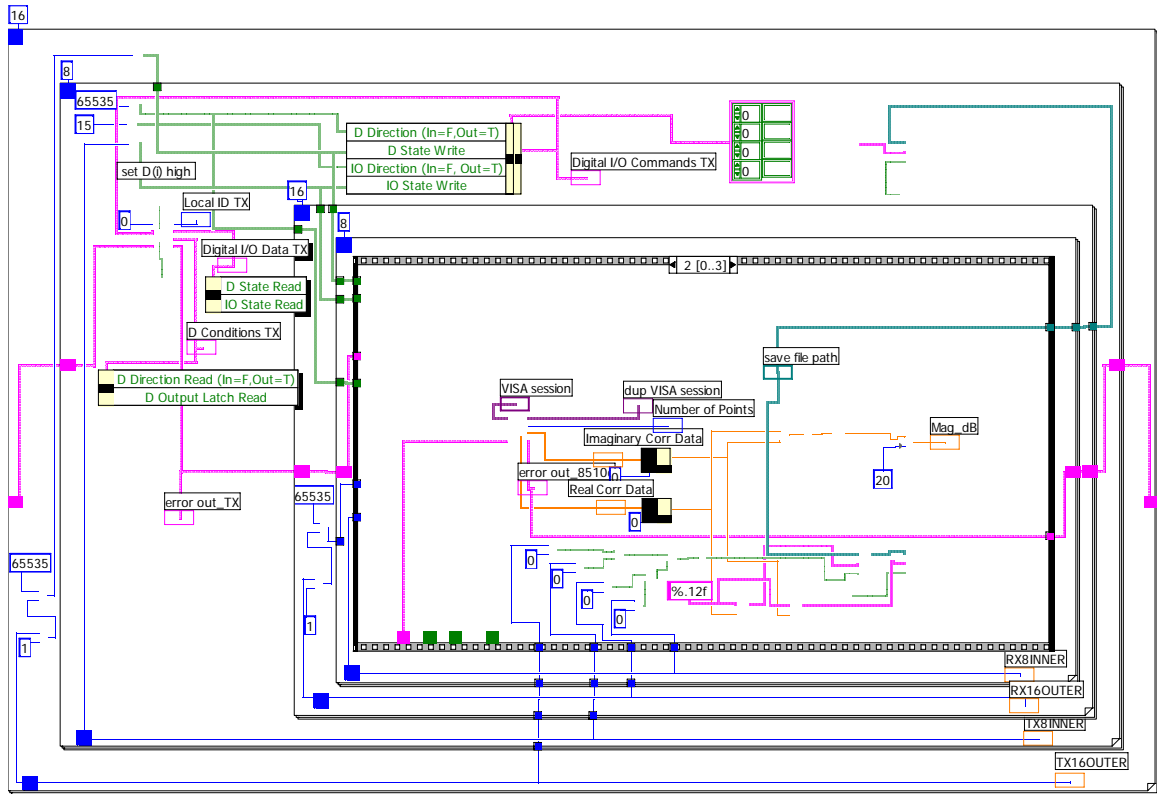


Figure 4.43 Measurement of Data Through Network Analyzer

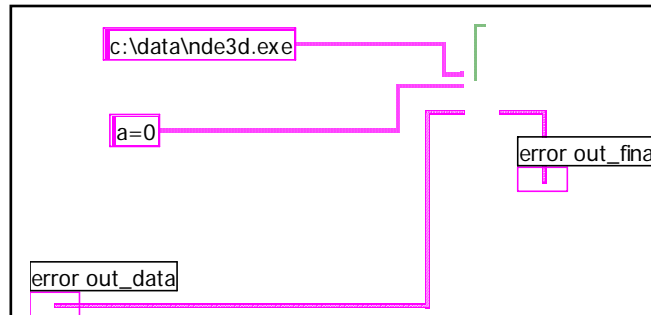


Figure 4.44 Execution of Imaging Program after Measurement

As shown in Figure 4.44, the imaging program can be executed right after the previous loops are done. The LabView program is calling a command window of the operating system, so that an executable file could be run through LabView program. The imaging program 'nde3d.exe' is called in the most upper pink window.

Figure 4.45 shows the panel interface of the program. Basically the diagram does not have to be understood in order to run the program. The panel interface provides the controllers and indicators. Controllers are those items that could be changed by user. Usually the parameters in the controller parts do not need to be modified. The default value is what's going to be needed during the measurement. For example, for the scattered field measurement, the default value is S_{21} , which supposes the transmit antennas are connected with port 1 of network analyzer, while the receive antennas are connected with port 2. If the positions of transmit and receive antennas exchange, S_{12} may be obtained from the S parameter controller.

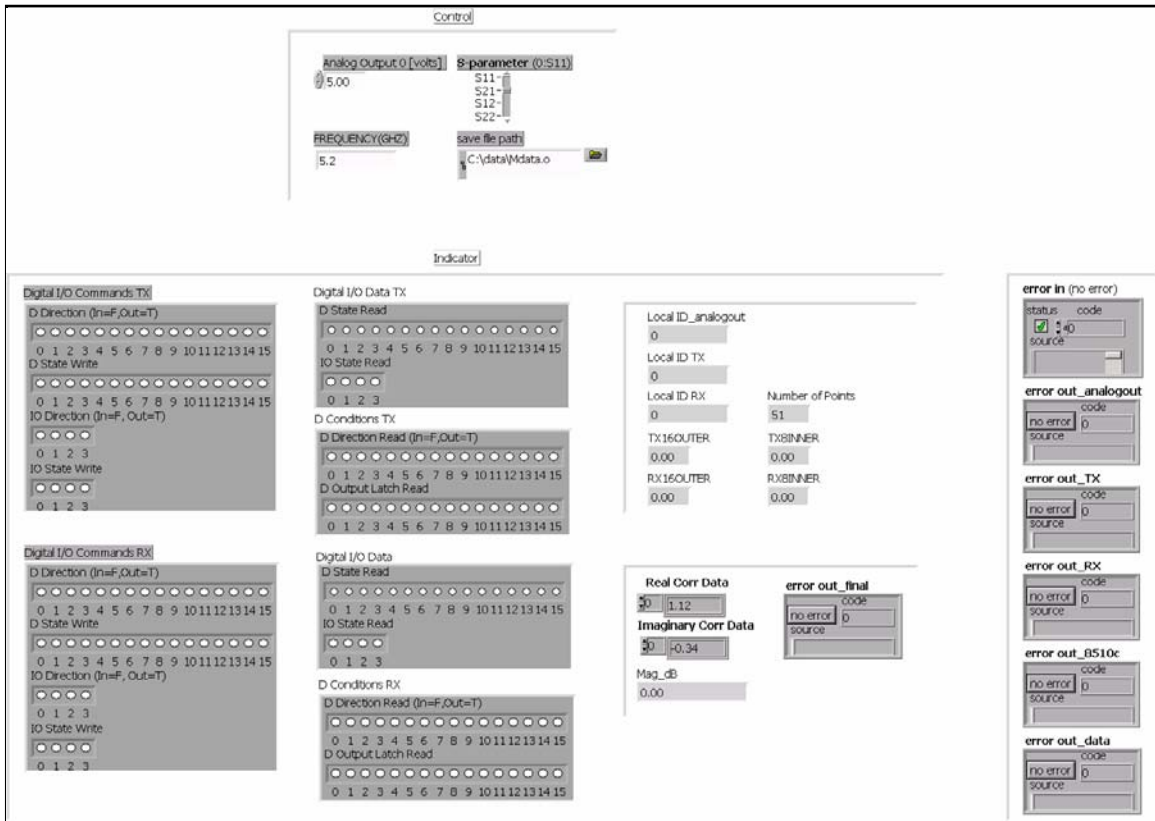


Figure 4.45 Panel Interface

Indicators show the status of the system. There are 2 sets of commands and status of the I/O digital outputs, through the 2 most left columns. The light gray column in the middle tells you the ID number of the LabJacks currently used for transmit and receive ends. As the lower part, the S parameter reading is showed simultaneously, the numbers are changing during the measurement. The magnitude of it is shown also. Error indicators are showing if there are abnormal things happening. If there are, the error information is given. In the normal measurement procedure, errors are not likely to be happened, so just check and make sure the controllers are having the right settings.

4.2.2.4. Measurement Speed Evaluation

In order to evaluate how fast the measurement is done, the 1st and 2nd outputs of the switching units were connected to oscilloscope to record the required time. **Figure 4.46** shows that one time measurement takes about 40ms, which means totally the measurement takes about 15 minutes.

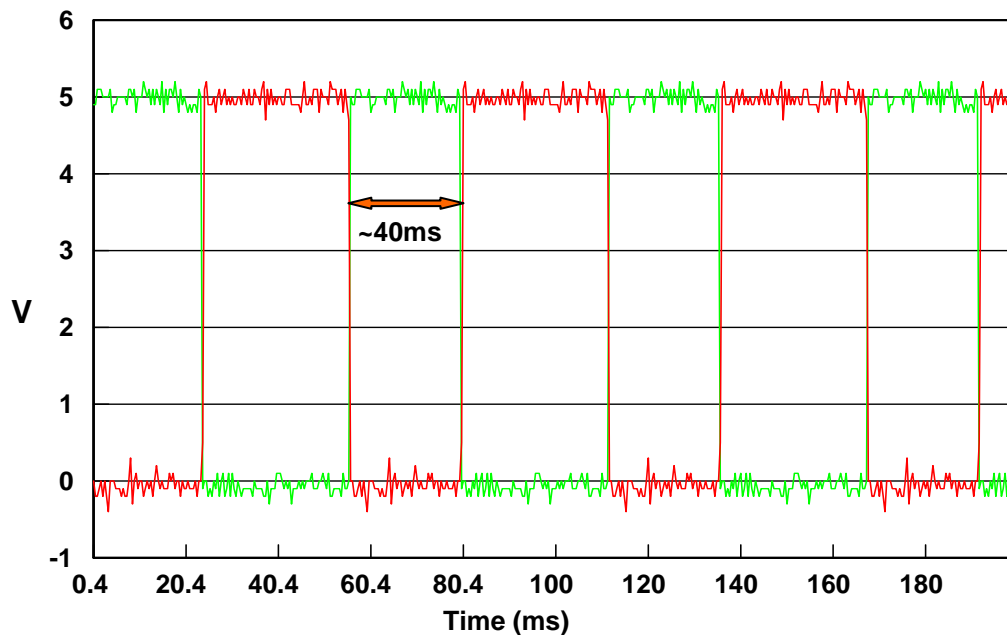


Figure 4.46 Measurement Time Shown in Oscilloscope

Chapter 5

NUMERICAL SIMULATION

Numerical simulations were carried out to test the proposed algorithm for the image reconstruction of a concrete specimen with internal air voids and steel bars. The reconstruction parameters including effective focusing area were investigated. Totally 7 cases were modeled with 5.2GHz as an illuminating frequency and the image of each case was reconstructed. Some of these numerical simulations were compared with the results with 10.0GHz as the illuminating frequency. This comparison showed that the resolution can be improved by using the higher illuminating frequency. For the simulation, planar rectangular antenna arrays were used with 8 transmitting/receiving antennas for the case of 5.2GHz and 16 transmitting/receiving antennas for the case of 10.0GHz. For simplicity, only a 2D rectangular geometry was considered for the investigation and only Y polarization of the antenna was used. Extension to 3D can be easily obtained by using the spherical Green's function as a focusing operator instead of the Hankel function.

5.1. Effective Focusing Area (EFA)

Reconstruction parameters such as focusing intensity and impulse response of the system for the planar antenna array were investigated. Based on the results of a parametric study using point-like objects, the effective focusing area (EFA), in which the focusing operation is effective, was determined. In other words, the focusing intensity level and impulse response shape has a good uniformity in the effective focusing area. Also, the effective penetration depth is determined by the effective focusing area. The shape and size of the effective focusing area (penetration depth) strongly depend not only on the electrical size of the measuring line, but also on the arrangement of the transmitting and receiving elements, which means that the EFA of a planar antenna array differs from the one for circular antenna array. Through a series of simulation using

point-like objects, in which the focusing intensity level and shape of impulse response at different locations were compared, the effective focusing area was determined as the shape of a trapezoid, as represented in [Figure 5.1](#).

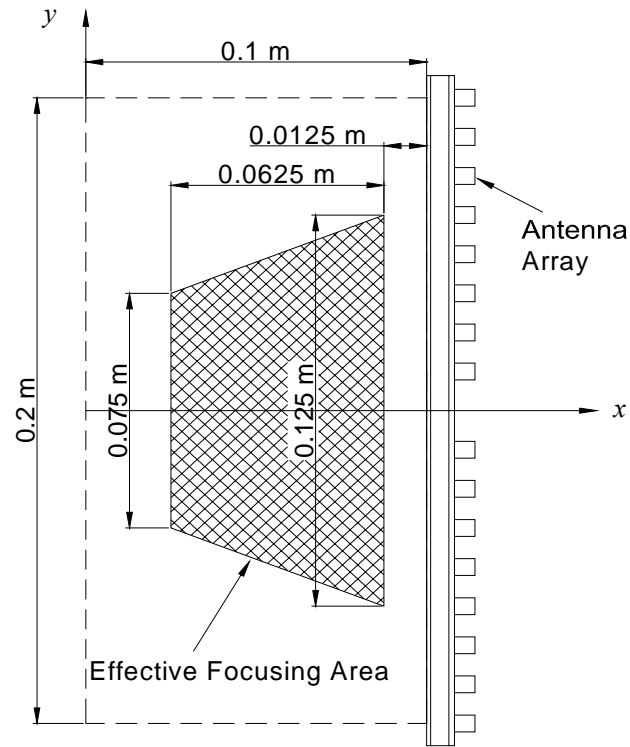


Figure 5.1 Effective focusing area of planar rectangular antenna array

5.2. Simulation Results Using 5.2 GHz

Based on the reconstruction parameters, especially the effective focusing area, numerical simulations were carried out. For the direct problem in which the antenna radiates a wave and receives the scattered field, a 3D structure simulator, CST Microwave Studio[®], was used for measuring the transmission parameters (S_{ij}) in each array. Totally, seven geometries were modeled with a 16-slot antenna. In the simulation, the background material was modeled as concrete so as to radiate the wave through the concrete. Open boundary conditions were applied at the top and the bottom of the geometry in order to generate absorbing conditions.

Using the S_{ij} measurements from each array, the measurement matrix of Eqn. (3.12) was assembled and the electromagnetic image of $E_f(\mathbf{r}_f)$ at $\mathbf{r}_f=(x_f, y_f)$ was obtained as presented previously.

All the objects used in the numerical simulation were located inside of the effective focusing area. The reconstructed images for each case are reported in Figure 5.2 along with the model description and the reconstructed area.

In case 1, the air sphere was successfully reconstructed with exact location and size as represented in Figure 5.2(a). The reconstructed area was limited to 5cm in x -direction because the open boundary in CST Microwave StudioTM was set at the y -axis, from which the distance to the antenna array is 5cm. The reconstructed area in the x -direction for the other cases was also determined by the location of an open boundary (10cm in the x -direction).

In cases 2 and 3, a square and a rectangular air block were placed inside the concrete material, respectively. As shown in Figure 5.2(e) and (f), the reconstructed image shows the exact location and the approximate size of the air blocks in both cases, although there was some noise. These two cases were investigated again at the higher frequency in order to demonstrate the improvement of resolution.

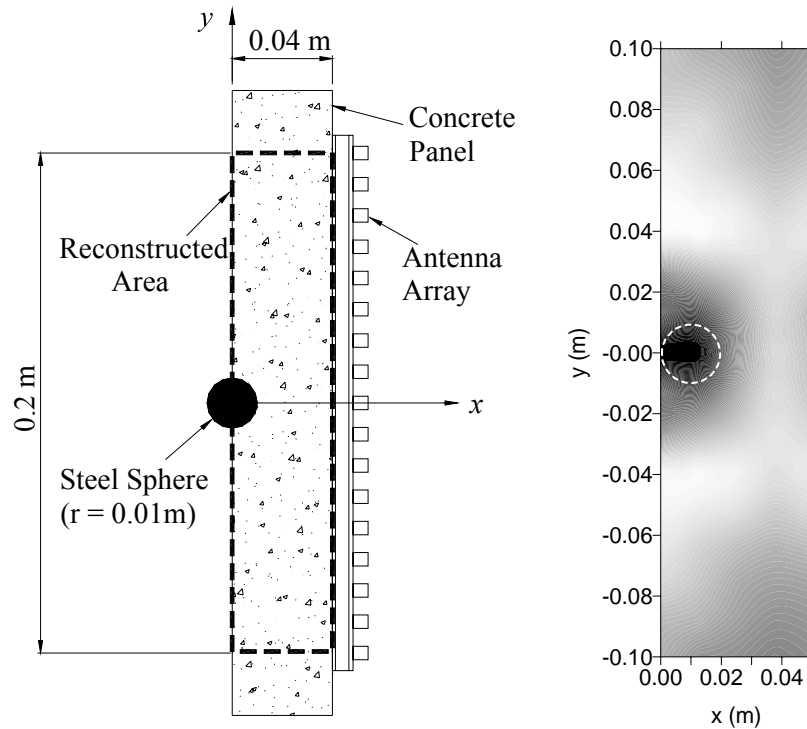
Cases 4 and 5 show the transverse and longitudinal resolution of the system, respectively. The wavelength in concrete at 5.2GHz is about 2.5cm, which provides the resolution of the system of 2.5cm. As represented in Figure 5.2(b), the locations of two steel bars separated with transverse distance of 2.5cm (λ_c) were detected apparently, although the resolution was not sufficient enough to reconstruct the exact shapes of the bars. Figure 5.2(c) shows the reconstructed image of two steel bars placed at a longitudinal distance of 2.5cm (λ_c). In this case, the two bars could be successfully identified, but the exact shapes could not be reconstructed due to the lack of resolution. From the results of cases 2 and 3, it was demonstrated that the resolution of the system with planar antenna array is of the order of a wavelength in concrete (2.5cm), which can identify the approximate shapes and locations.

In case 6, six steel bars were placed at the boundaries of the effective focusing area for the reconstructing of a 2D cross section. The result, as shown in Figure 5.2(d), demonstrated that the objects near the antenna arrays are more clearly identified rather

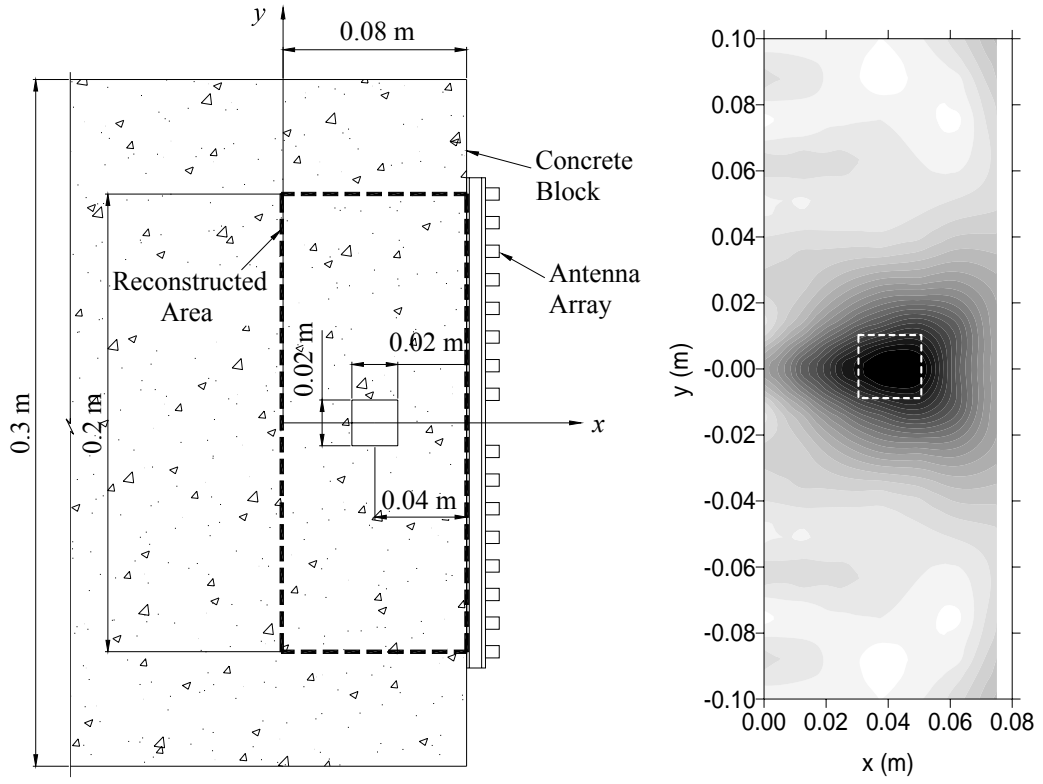
than the ones at the farther boundaries of effective focusing area, which is marked by black line, from the antenna array.

In case 7, a steel square bar and an air block were placed inside the concrete material. The difference in the dielectric constant between steel and concrete is much bigger than the one between air and concrete. For this reason the air void is more difficult to detect than the steel bar. As shown in [Figure 5.2\(g\)](#), although the steel is located far from the antenna array, the main features are correctly located, including size and position, while for the air void only the location is detected.

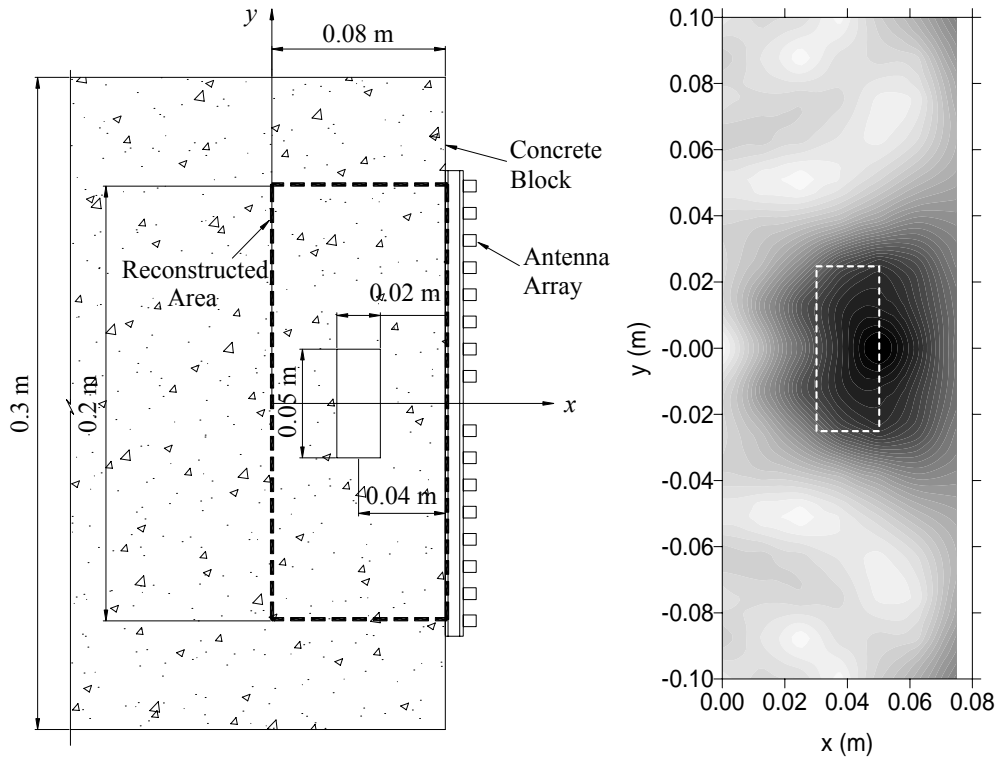
Using the results of the numerical simulation, the efficiency of the image reconstruction algorithm was tested through different cases, including steel, air voids, or combinations of the above. Within the effective focusing area, the location and size of objects were successfully detected.



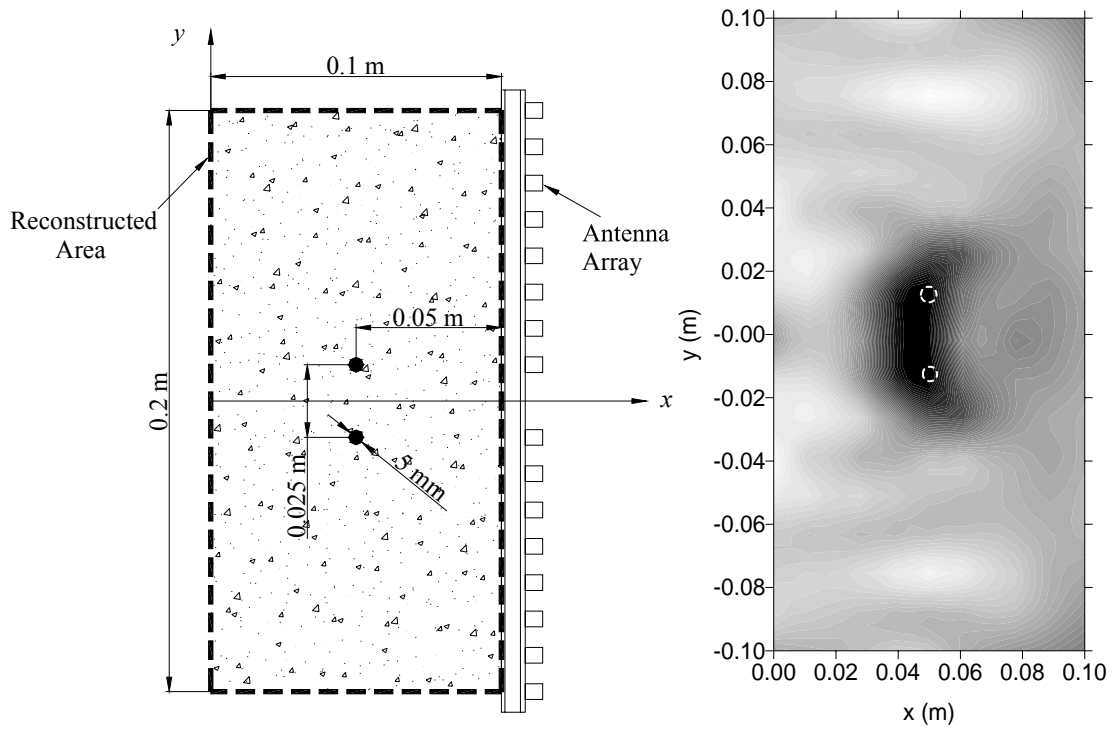
(a) Case 1



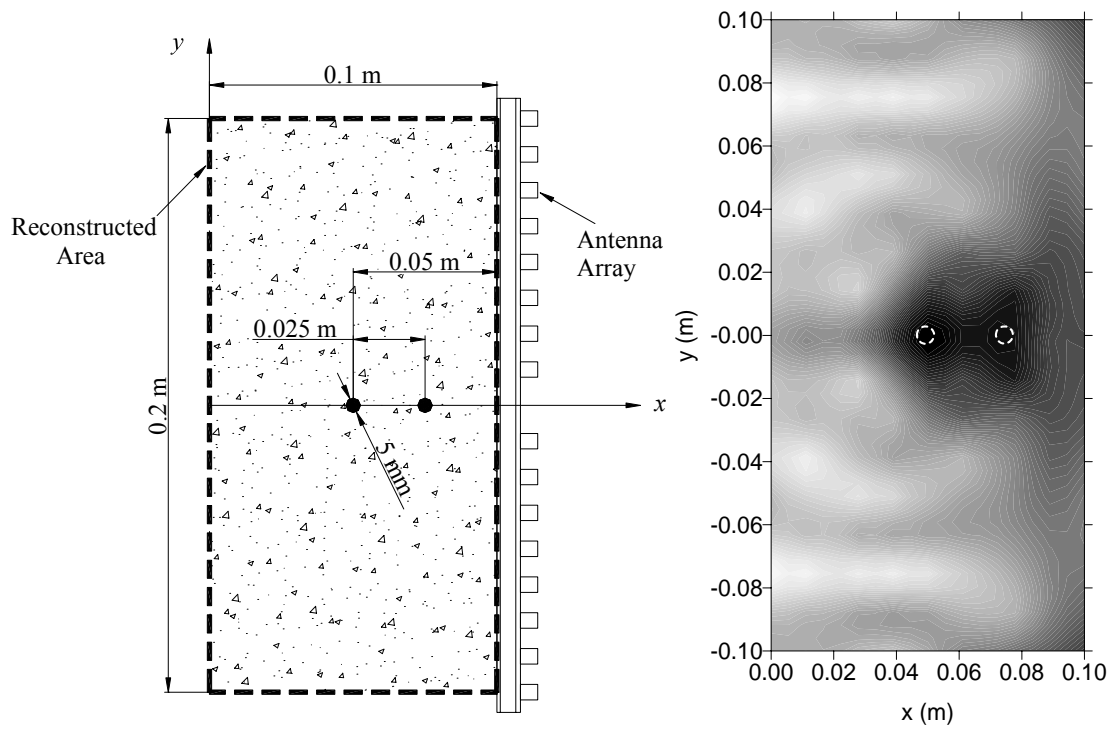
(b) Case 2



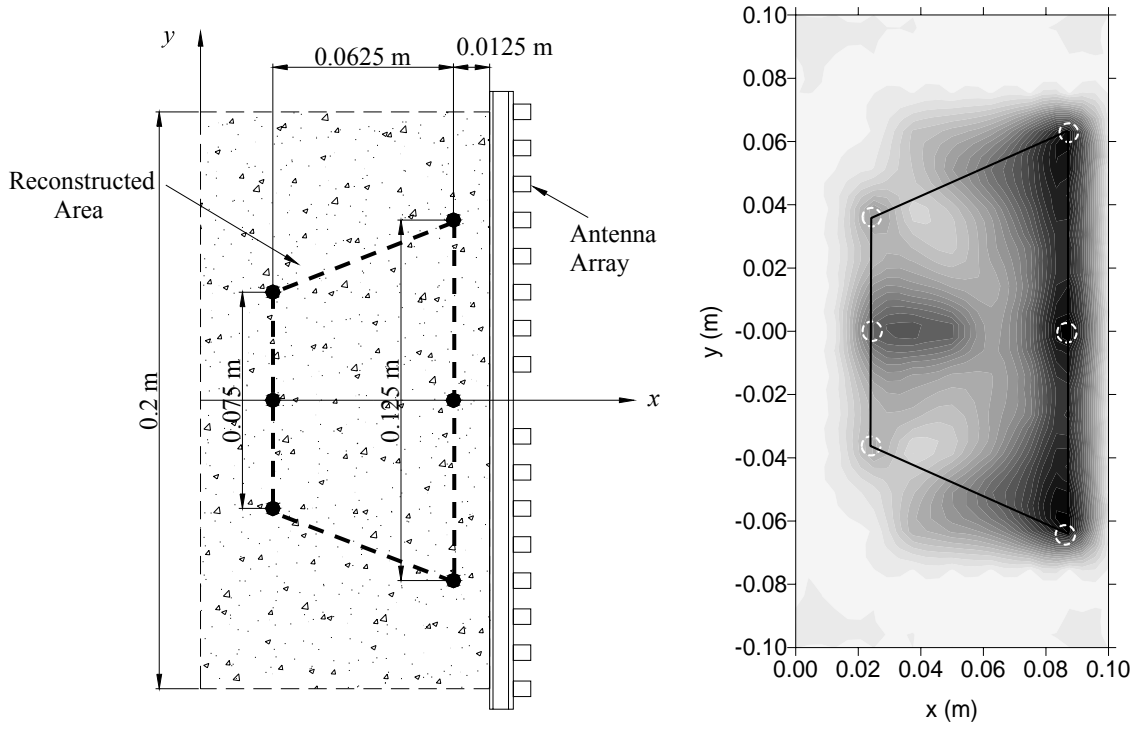
(c) Case 3



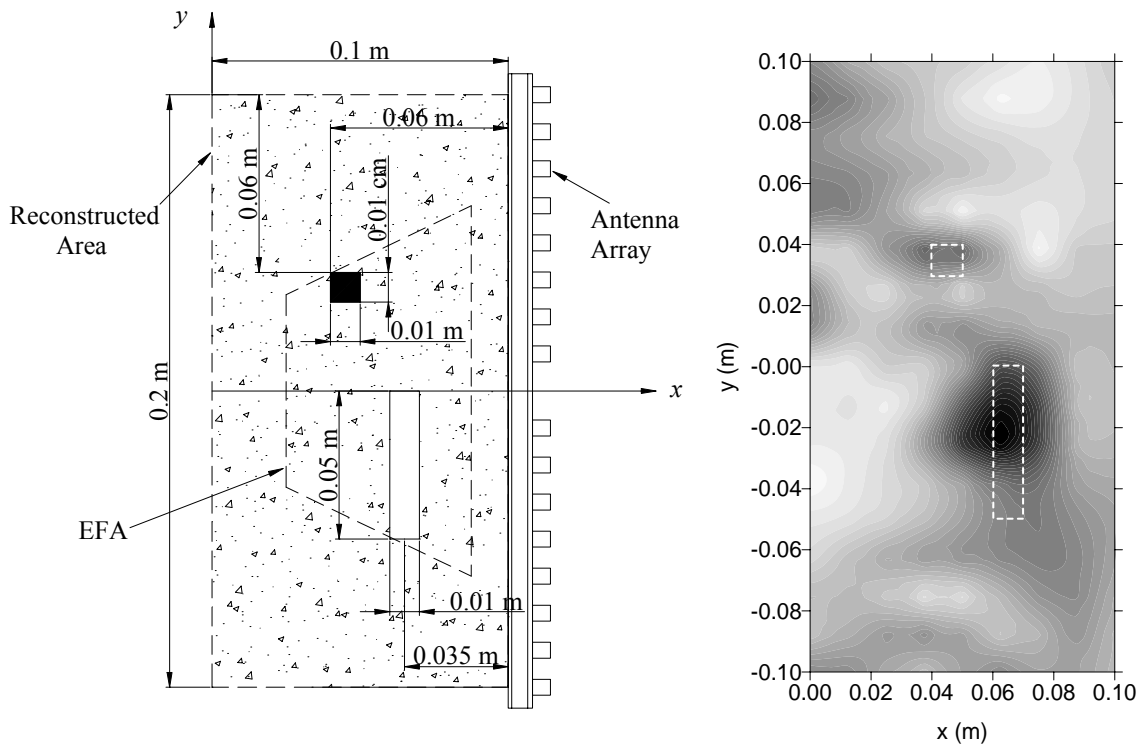
(d) Case 4



(e) Case 5



(f) Case 6



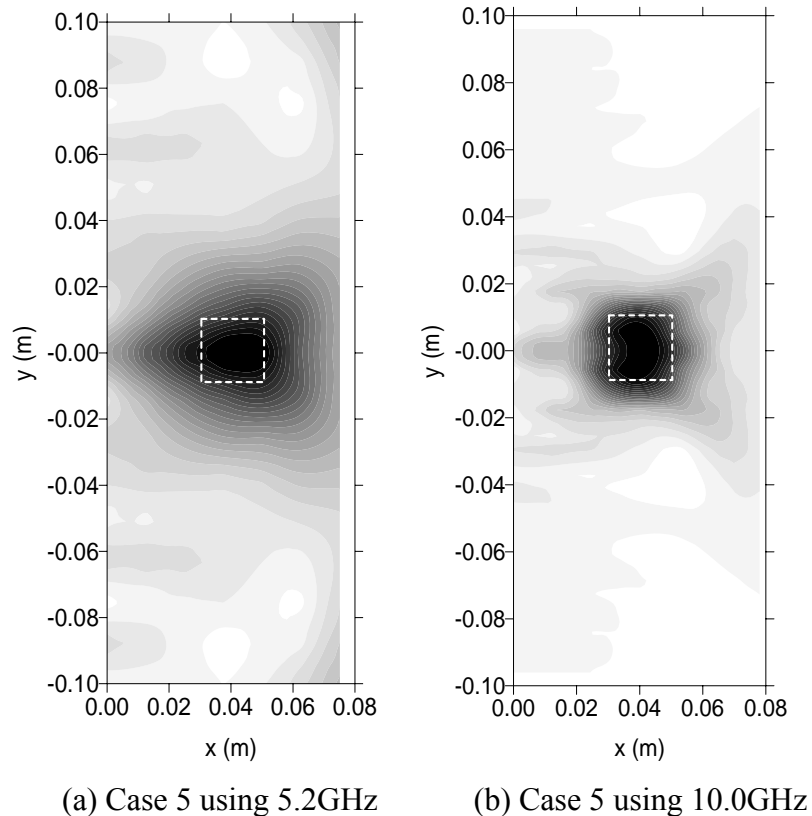
(g) Case 7

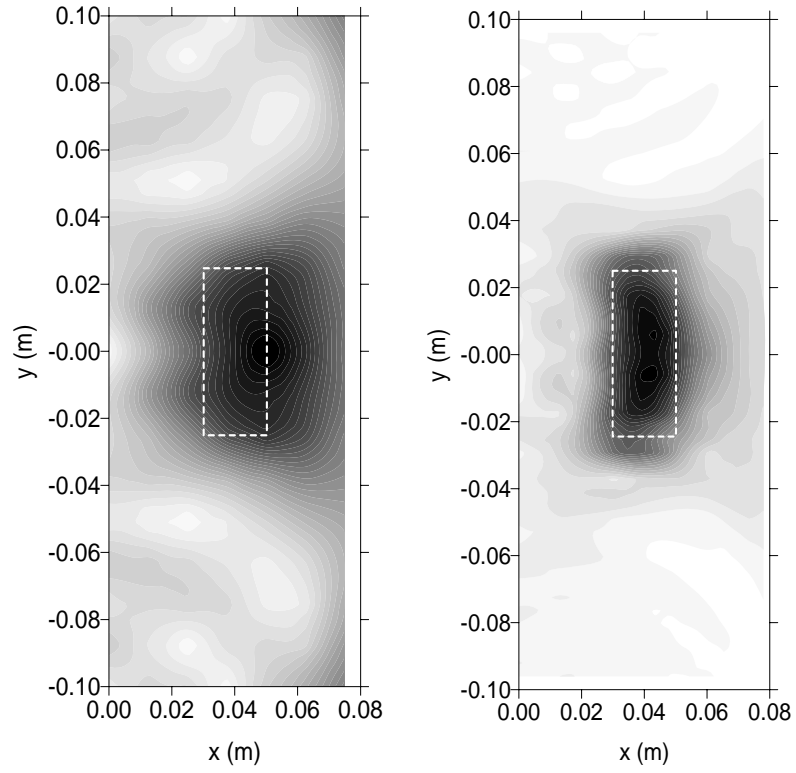
Figure 5.2 Simulation Results with Descriptions

5.3. Simulation Results Using 10.0 GHz

In the antenna design, the illuminating frequency was determined as 5.2GHz as a good compromise between a set of different parameters, such as size, resolution, attenuation, and simplicity of prototype. For that reason, the resolution of the system, as shown in the previous simulation results, was limited to 2.5cm and the exact shape of the object inside concrete could not be reconstructed. Better resolution, however, can be obtained by increasing the illuminating frequency.

In order to demonstrate the improvement of resolution using higher illuminating frequency, cases 5 and case 6 were investigated again with 10.0GHz as an illuminating frequency. For the numerical simulation, the planar rectangular antenna arrays with 16 transmitting and 16 receiving antennas were used. The results in [Figure 5.3](#) show that the resolution of the reconstructed image can be improved by increasing the illuminating frequency and that the exact shape and location of the voids can be reconstructed when using 10.0GHz.





(c) Case 6 using 5.2GHz

(d) Case 6 using 10.0GHz

Figure 5.3 Resolution Improvement Using Higher Frequency

Chapter 6

EXPERIMENTAL VERIFICATION

6.1. Microwave Imaging Using Prototype I

In this section, the effectiveness of the proposed sub-surface imaging technology using the prototype I system was investigated through a series of experiments on a concrete panel and a concrete block.

6.1.1 Experimental Setup

The effectiveness of the proposed sub-surface imaging technology was further investigated through a series of experiments on a concrete panel and a concrete block. A steel rod was placed on one of the faces of the concrete panel to simulate steel rebar. The 30 cm × 30 cm × 30 cm concrete block involves two internal voids artificially generated using Styrofoam (whose dielectric property is the same as that of the air); one is a 2 cm cubic void and the other is a 5 cm × 2 cm × 2 cm void. The Styrofoam blocks were inserted into the concrete during the pouring of concrete with the distance of 3 cm from the face of concrete to the face of Styrofoam in both cases. Samples using steel bars in the air were also prepared. All the experimental cases, identical to those used in the numerical simulation, were described in [Table 6.1](#).

Table 6.1 Descriptions of Cases for Experimental Study

Case number	Description	Reconstructed Area ($x \times y$) (cm×cm)	Exact Locations of Objects (x,y) (cm)
1	Steel sphere at the center of concrete panel	4 × 20	(0,0)
2	square air void inside concrete	8 × 20	(4,0)
3	rectangular air void inside concrete	8 × 20	(4,0)

The experimental setup consisted of a network analyzer, a switch box, coaxial cables and the antenna array as shown in [Figure 6.1](#). The network analyzer is a two-port device capable of transmitting a signal at one port and receiving a signal at the other port while evaluating the magnitude and phase of the receiving signal. The network analyzer was used to evaluate the signal transmitted through the medium (S_{12}). The switch box developed in this study is a radio frequency network capable of controlling multiple antennas in the array and selecting them individually to perform S_{12} measurement.

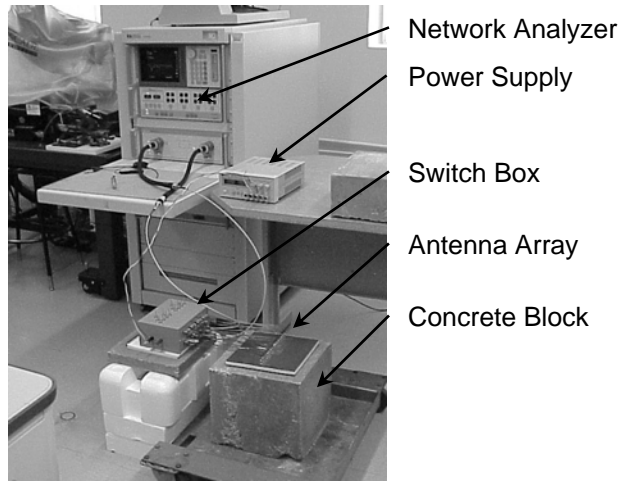


Figure 6.1 Experimental Setup

Calibration was performed to remove the effect of wave reflections and loss in the coaxial cables and the switch box from the measured signals ([Kim 2002](#), [Kim et al., 2002](#)). For the calibration purpose, concrete panel without defect and steel plate are used as represented in [Figure 6.2](#).

Each transmission measurement without all the effects from the coaxial cables and the switch box, which is from the transmitting array to the receiving one, is proportional to the zero-order Hankel function of the second kind, $H_0^{(2)}(k_{e,conc}d_{ij})$, whose argument is proportional to the distance from the transmitting array to the receiving one, d_{ij} ([Balanis, 1998](#)). All the measurement effects from the coaxial cables and the switch box (calibration factor), therefore, can be calculated by dividing each transmission measurement of calibration ($S_{ij}^{(cal_mea)}$) by the zero-order Hankel function of the second kind, and the calibrated transmission measurement ($S_{ij}^{(cal)}$) can be obtained by dividing

each transmission measurement ($S_{ij}^{(mea)}$) by calibration factor, as follows for the case of transmitting array i and receiving array j .

$$S_{ij}^{(cal)} = \frac{S_{ij}^{(mea)}}{Cal_Factor} \quad (6.1)$$

where

$$Cal_factor = \frac{S_{ij}^{(cal_mea)}}{H_0^{(2)}(k_{e,conc} d_{ij})} \quad (6.2)$$

Amplitudes of calibrated measurements in a concrete without defects are proportional to the distance between the transmitting and the receiving arrays, and symmetric with respect to the diagonal in a measurement matrix. The calibration factors of each transmission measurement at 5.2 GHz are used for calculating the calibrated measurement matrix in next section.

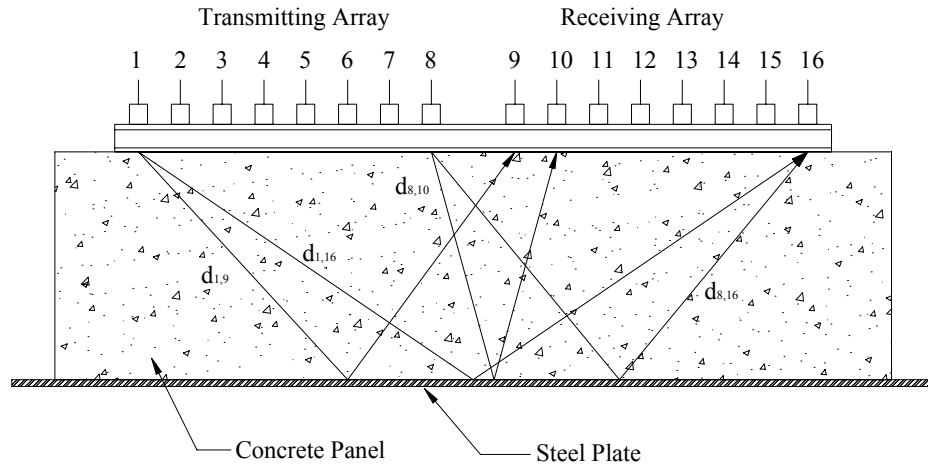


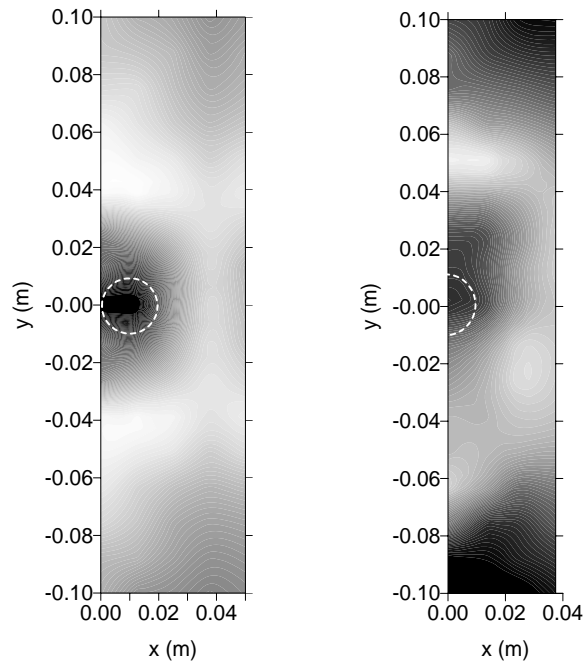
Figure 6.2 Description of Calibration Scheme

6.1.2 Experimental Results

A continuous 5.2 GHz sinusoidal electromagnetic (EM) wave was generated from the signal analyzer and sent to the test specimen. Transmission measurements of each transmitting and receiving array pair at this frequency were assembled to form a measurement matrix. The switch box controlled the active location of the transmitting and receiving arrays from $S_{1,9}$ to $S_{8,16}$. Each measured signal was divided by the

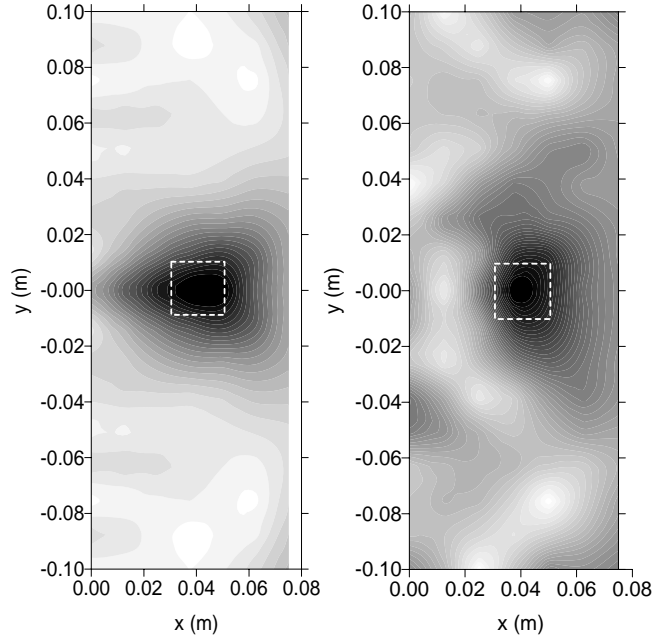
calibration factor at 5.2 GHz and assembled to form a calibrated measurement matrix to be multiplied by the numerical focusing operators. The reconstructed images, the distributions of the electric current amplitude, are plotted in [Figure 6.3](#) through [Figure 6.5](#) for the center cuts of all the experimental cases, comparing with the simulation results.

In case 1 that is identical to numerical simulation case 1, the location as well as the size of the steel sphere was detected, although the edge effects due to the small size of concrete specimen added some noises to the experimental result. Experimental results of cases 2 and 3 are shown in [Figures 6.4\(a\) and 6.5\(a\)](#), that involve air voids inside the concrete block respectively identical to simulation cases 2 and 3. The images of the square and the rectangular Styrofoam's (i.e., the air voids) were successfully reconstructed in terms of their approximate sizes and locations, although the resolution (2.5 cm at 5.2 GHz) was not sufficient to reconstruct the exact features. The numerical simulation results in [Figures 6.4\(b\) and 6.5\(b\)](#) agree with the experimental results in [Figures 6.4\(a\) and 6.5\(a\)](#). This verifies the effectiveness of the simulation model using the program, CST Microwave Studio[®].



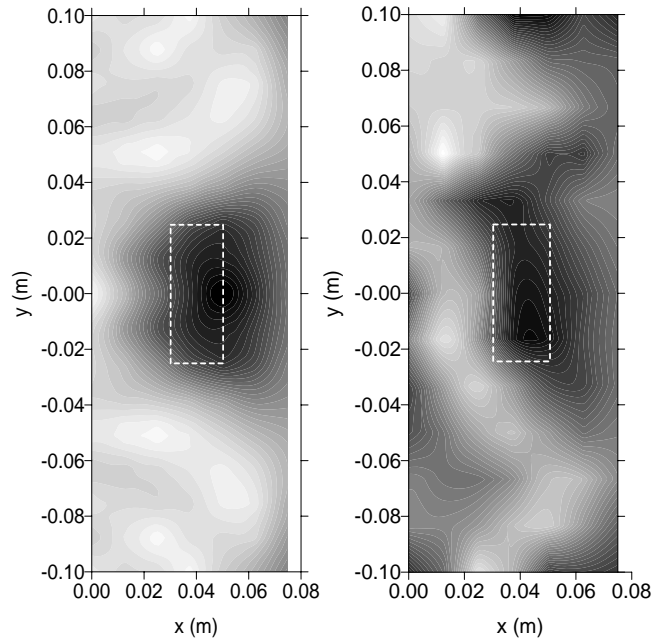
(a) Simulation Result (b) Experimental Result

Figure 6.3 Reconstructed Image of Case 1



(a) Simulation Result (b) Experimental Result

Figure 6.4 Reconstructed Image of Case 2



(a) Simulation Result (b) Experimental Result

Figure 6.5 Reconstructed Image of Case 3

Chapter 7

OPERATOR'S MANUAL OF IMAGING SYSTEM

This document is an operator's manual of the imaging system explaining the usage of the system and the communication details between the modules and function of each unit.

System Description

This microwave image reconstruction system is for condition assessment of concrete structures. The system consists of several units including a control module, a switching unit, an antenna array, a network analyzer, an image reconstruction algorithm, and a display unit. The final product to the user is a reconstructed image of the object under testing, showing 3-dimensional profiles of the object. The reconstructed image is generated using the scattered field by microwave illumination using the antenna array. The measurement is performed by electronically switching the antenna array controlled by the control module and software. The following **Figures 7.1 and 2** describe the job flow and the block diagram of the system, and **Figure 7.3** shows a picture of the system.

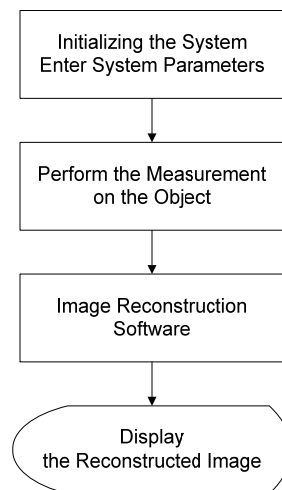


Figure 7.1 Job Flow of the System

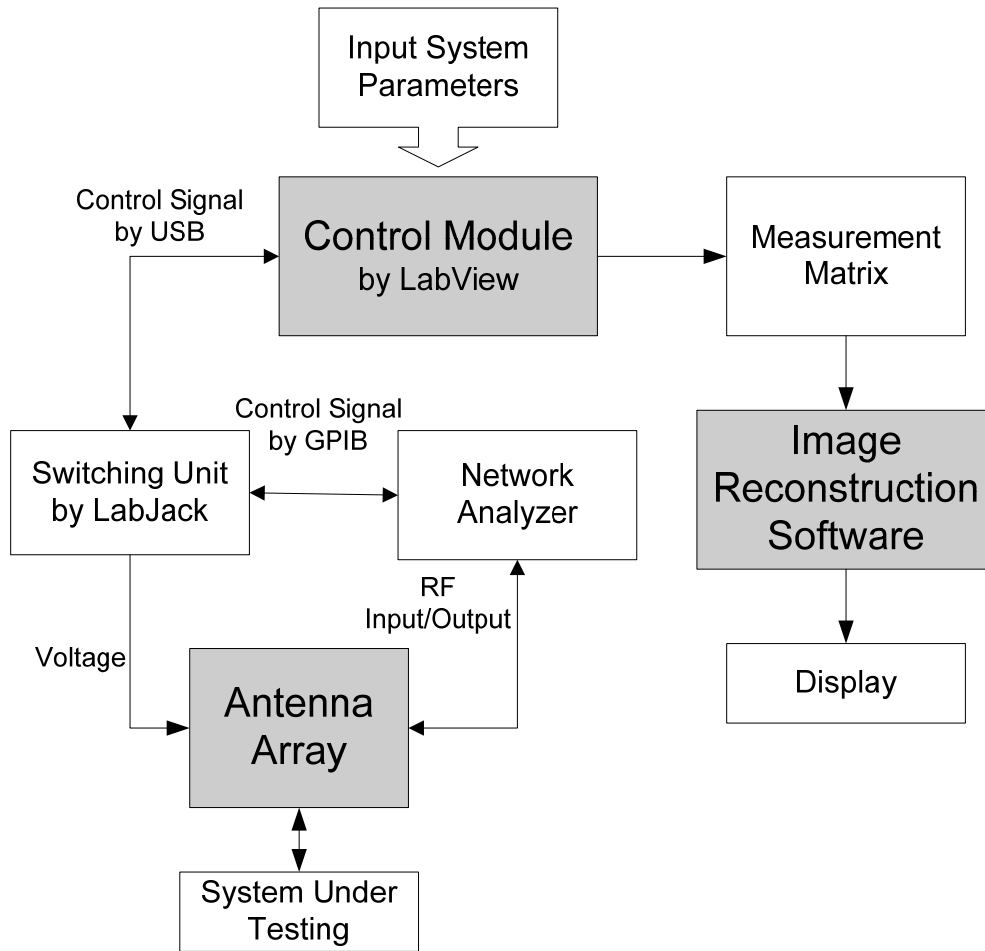


Figure 7.2 Block Diagram of the System

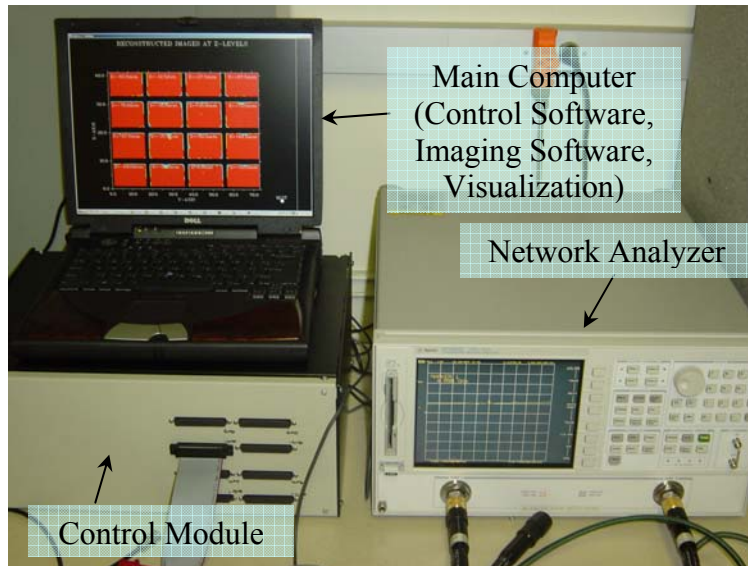


Figure 7.3 Outside View of the System

How to Operate the System?

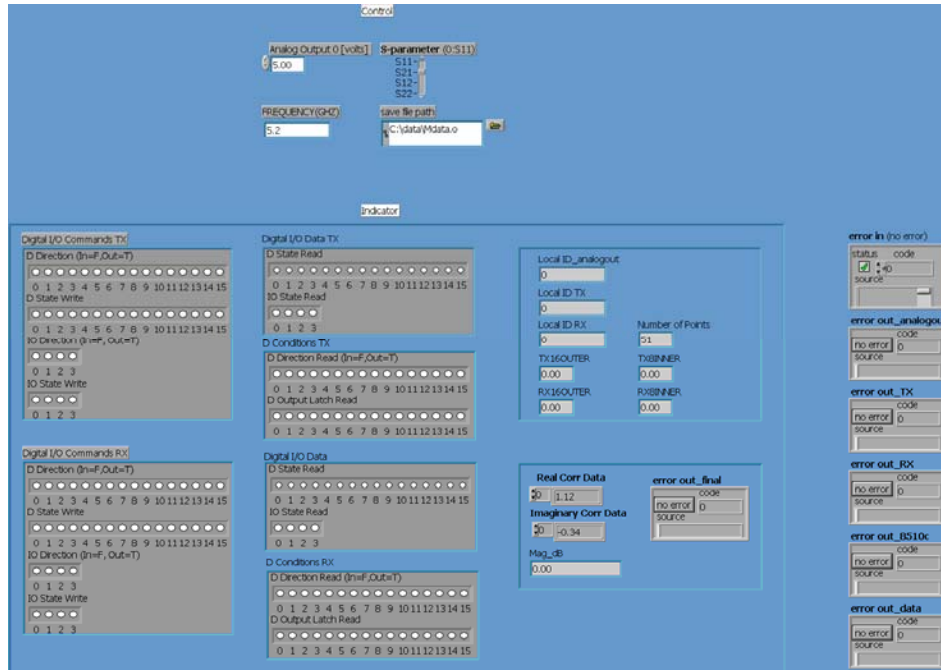
The operation of the system consists of three steps: initialization, measurement, and visualization. At each step, the following operations are needed.

1. Initialization

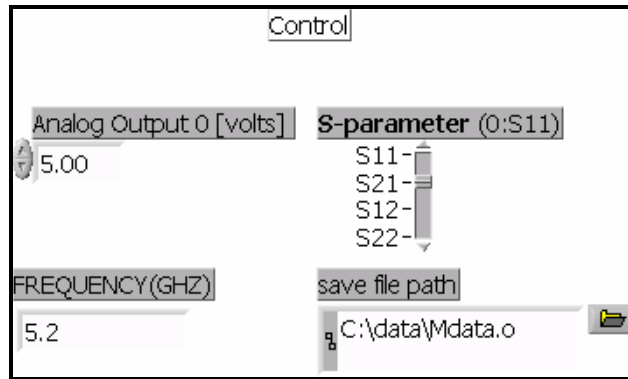
When the operator runs the program named ‘caltrans.exe’, the first step of initialization is to determine and enter the system parameters:

- Frequency (5.2GHz): illuminating frequency
- Analogue Voltage Output (5V): voltage output to control switches
- S-parameter (S21): measurement from the network analyzer
- Save File Path (“mdata.o”): measurement matrix file name and path. File name should always be “mdata.o”.

If the system is operating under the normal condition, the operator can use default values of 5.2, 5.00, S21, and “mdata.o”. **Figure A.4** shows the front panel displayed in the laptop including the system parameter input part.



(a) Front Panel View



(b) System Parameter Input (default values)

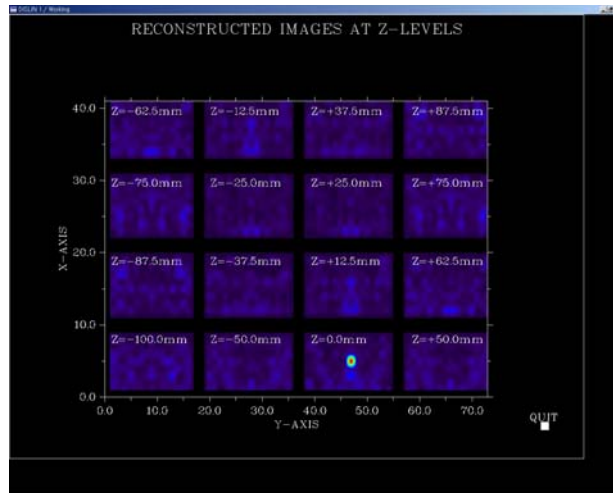
Figure 7.4 Front Panel of Control Module

2. Measurement

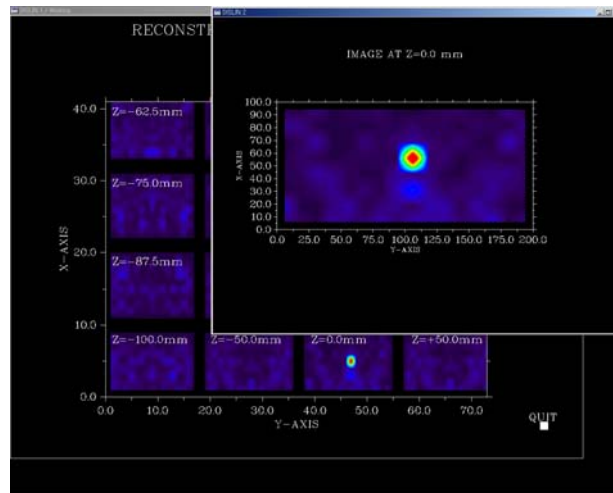
Once the system parameters are set, the operator can put the antenna array on the object to be investigated and click the “RUN” button at the top of the front panel. The control module program will automatically transmit and receive the microwave signal through the antenna array by switching each antenna elements.

3. Visualization

At the end of the measurement, the control module program will automatically execute the image reconstruction program named as ‘nde3d.exe’ opening a new window. The image reconstruction program analyzes the measurement matrix and displays cut images at several vertical locations in the reconstructed volume, and then the operator can select and magnify any of the cut images to investigate in details. Details of the image reconstruction program are introduced at Appendix B.



(a) Several Cut Images along Z-Axis



(b) Magnified Image at Z=0 mm

Figure 7.5 Example Screen Shot of Visualization Software

Chapter 8

SUMMARY AND CONCLUDING REMARKS

A sub-surface focused microwave imaging technology was developed in this project for detecting invisible damage and/or objects inside concrete structures. Significant theoretical, analytical, numerical, and experimental studies have been carried out in this project, laying a theoretical and technical foundation for the implementation of the microwave imaging technology. This project has delivered two prototype microwave imaging systems including hardware (antenna arrays involving a large number of antennas, switching and control circuitry) and software (imaging reconstruction and visualization). One of the systems was successfully tested through experiments on concrete specimen. The following concluding remarks can be made:

- (1) The effectiveness of the image reconstruction algorithm using the innovative numerical bi-focusing operator proposed in this study was verified experimentally as well as numerically. An image resolution in the order of the wavelength in a dielectric medium (concrete in this case) can be achieved by focusing both in the transmitting and receiving arrays, which doubles the resolution achievable by the conventional mono-focusing
- (2) The multi-frequency technique proposed in this project is effective in reducing the background noise and thus enhancing the clarity of the reconstructed image.
- (3) Experiments verified that the slot type of the antenna array is suitable for damage detection of concrete structures due to its high radiation performance and bandwidth as well as low mutual coupling among the antennas.
- (4) Prototype I successfully detected size and depth of invisible air voids and steel inside concrete specimens.
- (5) Prototype II successfully integrated four major modules including the antenna arrays, the control module, software in PC, and a network analyzer into a portable system. The control module under the control of the software effectively controls the bias for diodes to switch antenna with a high speed.

Nomenclature

E_i	<i>Incident Electric Field</i>
E_s	<i>Scattered Electric Field</i>
J	<i>Electric current distribution</i>
J_{eq}	<i>Equivalent electric current distribution</i>
S_{ii}	<i>Scattering parameter (reflection parameter)</i>
S_{ij}	<i>Scattering parameter (transmission parameter)</i>
k_0	<i>Wave number in air</i>
k_e	<i>Effective wave number in a medium</i>
ϵ_r	<i>Relative dielectric constant</i>
λ_0	<i>Wave Length in air</i>
λ_e	<i>Effective wave length in a medium</i>

References

- Balanis, Constantine A. (1989), *Advanced Engineering Electromagnetics*, Wiley, New York.
- Broquetas, A., Romeu, J., Rius, J.M., Elias-Fuste, A., Cardama, A., Jofre, L. (1991), “Cylindrical Geometry: A Further Step in Active Microwave Tomography”, *IEEE Trans. on Microwave Theory and Techniques*, 39, 836-844, May.
- Bucci, O. M., Crocco, L., Isernia, T., and Pascazio, V. (2000), “Inverse Scattering Problems with Multifrequency Data; Reconstruction Capabilities and Solution Strategies”, *IEEE Trans. Geoscience and Remote sensing*, 38(4), 1749-1756.
- Chase, S. B. and Washer, G. (1997), “Nondestructive Evaluation of Bridge Management in the Next Century”, *Public Roads*, July/August, 16-24
- CST-Computer Simulation Technology (2002), *HF Design and Analysis – CST Microwave Studio[®] 4*, Software Manual.
- Dunker, K.F. and Rabbat, B.G. (1990), “Highway Bridge Type and Performance Patterns”, *Journal of Performance of Constructed Facilities, ASCE*, 4(3), 161-173.
- Feng, M. Q., Flaviis, F. D., and Kim, Y. J. (2002), “Use of Microwaves for Damage Detection of Fiber Reinforced Polymer-Wrapped Concrete Structures”, *Journal of Engineering Mechanics, ASCE*, 128(2), 172-183.
- FHWA, (1998), “Transportation Equity Active for 21 Century (TEA-21)”, <http://www.fhwa.dot.gov/tea21/factsheet/bridge.htm>
- Garg, R., Bhartia, P., Bahl, I., and Ittipiboon, A. (2001), *Microstrip Antenna Design Handbook*, Artech House, Boston.
- Gironés, I.M., Jofre, L., Ferrando, M., De Los Reyes, M, and Bolomey, J. Ch. (1987), “Microwave Imaging with Crossed Linear Arrays”, *IEE Proceedings*, 134(3), June, 249-252.
- Harrington, R. F. (1961), *Time Harmonic Electromagnetic Fields*, McGraw Hill, New York
- Haroun, M. A. and Feng, M.Q. (1997), “Lap Splice and Shear Enhancements in Composite-Jacketed Bridge Columns”, *Proceedings of the 3rd US-Japan Bridge Workshop*, Tsububa, Japan

- Kim, Y. J. (2002), *Development of Electromagnetic Imaging Technology for Damage Detection*, Ph.D. Dissertation, University of California, Irvine, CA.
- Kim, Y. J., Jofre, L., De Flaviis, F., and Feng, M. Q. (2002), "Microwave Sub-Surface Imaging Technology for Damage Detection of Concrete Structures", *Proceedings of 15th ASCE Engineering Mechanics Division Conference*, New York, June, 589-596.
- Mast, J., Azevedo, S., Hadda, W., Ng, L., and Burnett, G. (1998), "Microwave Impulse Radar Technology and Applications", *Report of Lawrence Livermore National Laboratory*, UCRL-ID-130474
- Olson, L. D., Jalinoos, F., Aouad, M. F., and Balch, A. H. (1993), "Acoustic tomography and reflection imaging for nondestructive evaluation of structural concrete", *NSF SBIR Final Report (Award #9260840)*, Washington, D.C.
- Pierrri, R., Brancaccio, A., and De Blasio, F. (2000), "Multifrequency Dielectric Profile Inversion for a Cylindrically Stratified Medium", *IEEE Trans. Geoscience and Remote sensing*, 38(4), 1716-1724.
- Slaney, M., Kak, A. C., and Larsen, L. E. (1984), "Limitations of Imaging with First-Order Diffraction Tomography", *IEEE Trans. Microwave Theory and Techniques*, MTT-32(8), 860-874.
- Weil, G. (1994), "Nondestructive Testing of Bridge, Highway, and Airport Pavements", *Journal of Applied Geophysics*, August

Appendix A

REFERENCE MANUAL OF MUDULES

Communications Between the Modules

1. Control Module – Switching Unit (LabJack)

Control module (LabView) sends signals to switching unit of LabJack in order to control the switches in the antenna array. Since the Labjack has the LabView VIs, LabView program needs to have the following functions (also shown in [Figure A.1](#)):

- 1) Give out the output signal of control antenna array
 - i. Transmit antenna switching on one by one
 - ii. Receive antenna switching on one by one when one transmit antenna is switched on
- 2) Control signal of the network analyzer
- 3) Give a certain time to collect the S parameter measurement data (read data from network analyzer). In total there are 128×128 times reading and saving.

Here the measurement speed is dependant on the network analyzer, how fast it could be able to obtain the S parameter data.

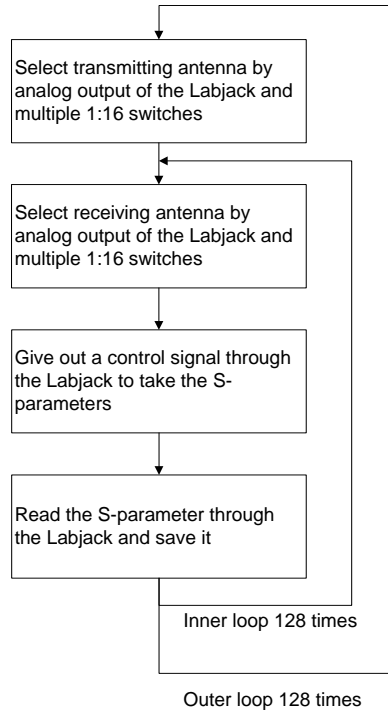


Figure A.1 Schematic of Algorithm

2. Switching Unit (LabJack) – Antenna Array

Analog output of switching unit (labjack) will be connected with 1:16 switch to control the antenna array, **Figure A.7** shows the sample of a 16 antenna array, and **Figure A.8** shows the truth table in which we know how to select only one of the 16th output to make it high to activate the antenna. For our case, by utilizing the enable line, we could expand to control 2 sets of 128-antenna array. The voltage need to switch “on ” is greater than 2.4v according to the data sheet of this 1:16 switch.

The labjack needs to control the transmit antenna and receive antenna array. The **Figure A.2** shows how the control signal goes.

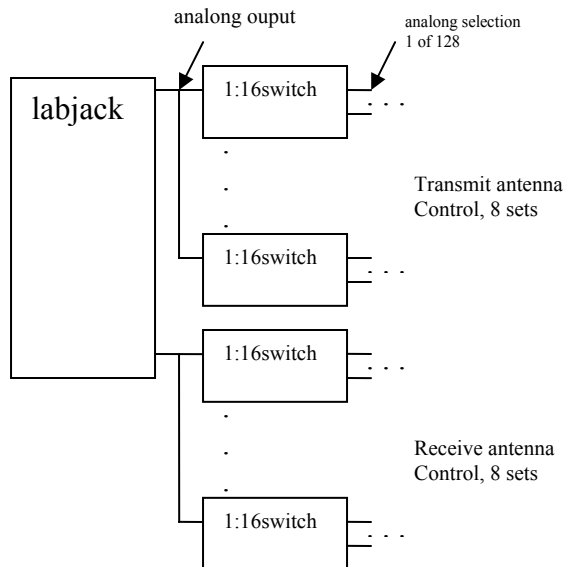


Figure A.2 Practical Model of 1:128 Switch

3. Antenna Array – Network Analyzer

In our case the network analyzer takes the S parameter data once the transmitting and receiving antenna is switched on. To read the data from network analyzer and store the data according to its corresponding antenna is realized by LabView programs.

The following graph shows how to get the measurement data:

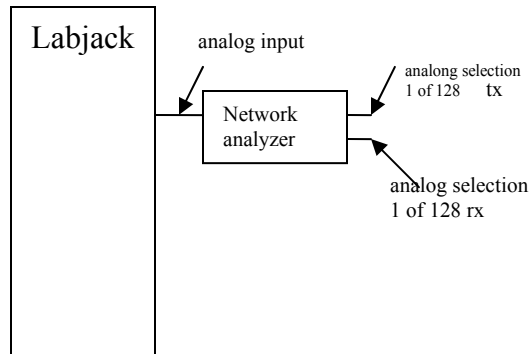


Figure A.3 Communication Between LabJack and Network Analyzer

4. Network Analyzer – Image Reconstruction Algorithm

The image reconstruction algorithm needs a measurement matrix to generate a reconstructed image. The elements of the measurement matrix are scattered fields measured at receiving antenna, and each of them has the index associated with the number of transmitting and receiving antenna; the number of row and column of each element corresponds to the one of transmitting and receiving antenna, respectively. **Figure A.4** describes the numbering of antenna element and corresponding location of the scattered field in the measurement matrix.

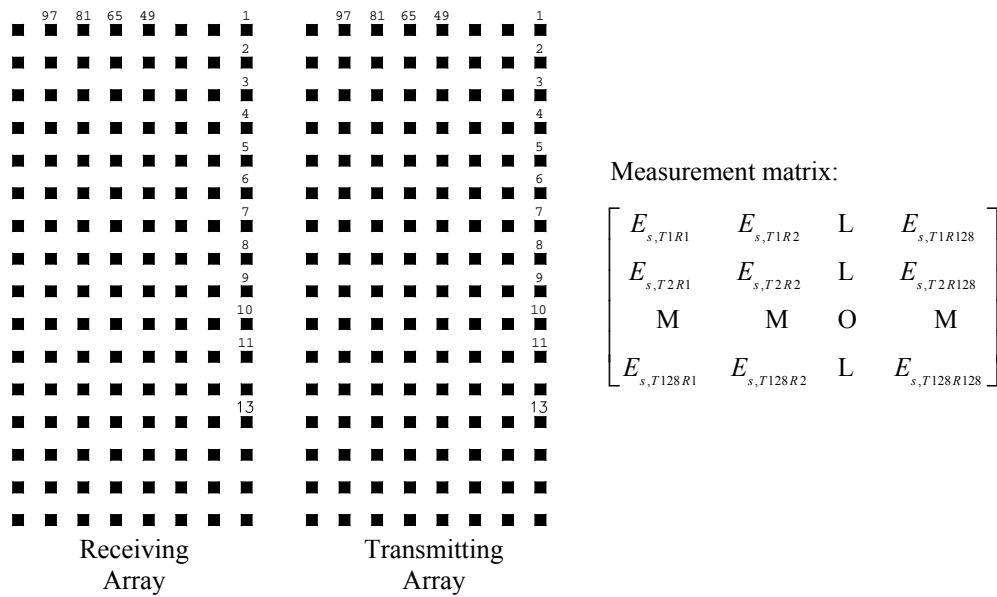


Figure A.4 Element of Measurement Matrix Corresponding to the Number of Element in Antenna Array

The algorithm needs a file as an input, which has scattered field in complex number) in a matrix form, in ASCII format as follows.

```

ES,T1,R1(complex) ES,T1,R2 ES,T1,R3 ES,T1,R4 ...
ES,T2,R1          ES,T2,R2 ...
...
ES,T128,R128      ...
    
```

Details of the Block

1. Control Module

LabView (www.ni.com) is used to control the whole system.

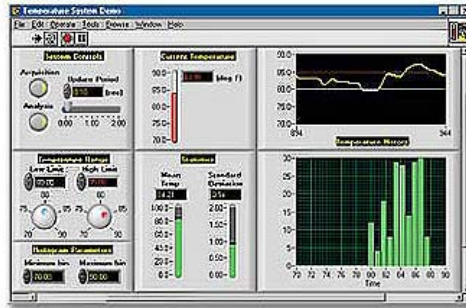


Figure A.5 Interface of LabView

2. Switching Unit

Labjack (www.labjack.com) is used to switch the antenna array.



Figure A.6 Photo of LabJack

Features we use

- 8 Single-Ended, 4 Differential 12-Bit Analog Inputs
- 2 Analog Outputs
- Up to 8 kSamples/Sec (Burst) or 1.2 kSamples/Second (Stream)
- Includes LabVIEW VIs
- Chips wired up with antenna array

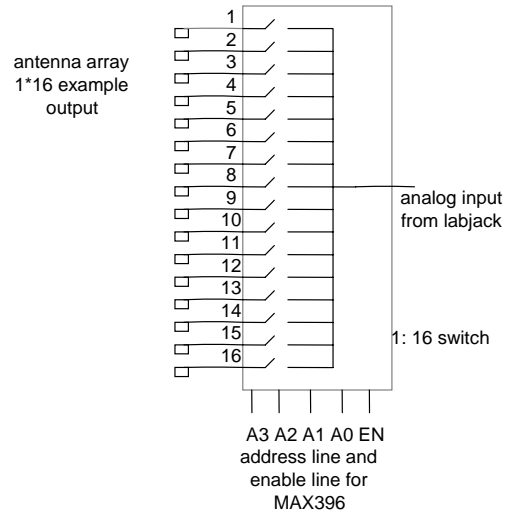


Figure A.7 Using the LabJack with Enable Line and Address Line

MAX396					
A3	A2	A1	A0	EN	ON SWITCH
X	X	X	X	0	NONE
0	0	0	0	1	1
0	0	0	1	1	2
0	0	1	0	1	3
0	0	1	1	1	4
0	1	0	0	1	5
0	1	0	1	1	6
0	1	1	0	1	7
0	1	1	1	1	8
1	0	0	0	1	9
1	0	0	1	1	10
1	0	1	0	1	11
1	0	1	1	1	12
1	1	0	0	1	13
1	1	0	1	1	14
1	1	1	0	1	15
1	1	1	1	1	16

Figure A.8 Truth table of MAX396

Appendix B

MANUAL OF IMAGE RECONSTRUCTION PROGRAM

Description

The program NDE3D is an image reconstruction program using measurement data file, 'mdata.o', which is saved as an ASCII file from network analyzer. NDE3D is embedded on the Labview program, set to be run after the measurement and saving it as an ASCII file.

The measurement data is saved as a matrix format (128 by 128). NDE3D loads the file, multiply the matrix with a focusing operator, which will be explained in next section, and show the cut images along the Z-axis in a window. Each image is an XY plane cut at 16 different locations along Z-axis. The user can pick one of the images to magnify in another window and to investigate more detail. The graphic library used in NDE3D is DISLIN 8.0B, which is developed by Helmut Michels in Germany.

Theory

Formulation of the image reconstruction algorithm was introduced in Chapter 3 of the report.

Input File

NDE3D needs two input files of measurement data and transformation information. Measurement data is an ASCII format file containing 128 by 128 matrix, in which each element is an amplitude of scattered field measured at each receiving antenna. The name of the file is 'mdata.o'.

The transformation information is also needed because the number of each antenna element differs from the one in control system. The file contains two numbers in a row, the number in control system and the corresponding number of real antenna element. The name of the file is 'trans.in'.

Code List with Comments

```

C*****
PROGRAM MAIN
C*****
USE DI SLIN
CHARACTER*16 MEASURE, TRANSFORM
COMPLEX J
COMPLEX FO_RMN, FO_TKL, TMP1, TMP2
COMPLEX SE_F(16, 8, 17), E_F(16, 8, 17), MEA(128, 128), MEA_T(128, 128),
1 MEA_TR(128, 128)
COMPLEX IT(128), IR(128)
REAL FREQ(10), KE(10)

C
COMMON /I OUNI T/I IN, I OUT
COMMON XT, YT, ZT, XR, YR, ZR
COMMON XF, YF, ZF

C
DI MENS I ON XT(16), YT(16), ZT(8), XR(16), YR(16), ZR(8)
DI MENS I ON XF(8), YF(16), ZF(17)
DI MENS I ON XO(100), YO(100), ZO(100), OBJ(100)
DI MENS I ON ABS_SE_F(16, 8, 17)
DI MENS I ON NTRM(128)
DI MENS I ON TTT(256)
DI MENS I ON NSLI CE(17)
C
PARAMETER (NXRAY=73, NYRAY=41)
DI MENS I ON RE(73, 41), RE_S(16, 8)

C
DI MENS I ON XRAY(73), YRAY(41), ZLEV(350), XRAY_S(16), YRAY_S(8)

C
IME=7
ITR=8

C
PI=3.14159265358979
J=(0., 1.)

C
CALL OPENFI LE
C*****
C
GENERATE TX&RX LOCATI ON
C*****
DX=0.
DY=12.5
DZ=12.5

C
DO K=1, 16
XT(K)=100.
XR(K)=100.
ENDDO

C
DO K=1, 8
ZT(K)=100. -DZ*(K-1)
ZR(K)=-12.5-DZ*(K-1)
ENDDO

C
DO L=1, 16
YT(L)=6.25+DY*(L-1)
YR(L)=6.25+DY*(L-1)
ENDDO
C*****
C
GENERATE RECONSTRUCTION VOLUME
C*****
DX=12.5
DY=12.5
DZ=12.5

C
DO K=1, 8
XF(K)=6.25+DX*(K-1)
ENDDO
DO L=1, 16
YF(L)=6.25+DY*(L-1)
ENDDO
DO M=1, 17
ZF(M)=-100+DZ*(M-1)
ENDDO
C*****
C
READ FREQUENCY I NFORMATI ON
C*****
N_FREQ=1

```

```

C      READ(I I N, *) (FREQ(N), N=1, N_FREQ)
      FREQ(1)=5.2
      DO N=1, N_FREQ
          KE(N)=2.302172887*2.*PI/(300./FREQ(N))
      ENDDO

C*****
C      START CALCULATION OF ELECTROMAGNETIC IMAGE OF E_F & SE_F
C*****
C
      DO N=1, N_FREQ
C*****
C      READ MEASUREMENT MATRIX FROM DATA FILES
C*****
C          READ(I I N, *) N_FILE
          N_FILE=1
          MEASURE='M DATA. 0'
          DO NF=1, N_FILE
C
              READ(I I N, *) MEASURE
              OPEN(UNIT=IME, FILE=MEASURE, STATUS='UNKNOWN')
              DO II=1, 128
                  READ(IME, *) (TTT(IJ), IJ=1, 256)
                  DO IJ=1, 128
                      MEA(II, IJ)=TTT(IJ*2-1)+J*TTT(IJ*2)
                  ENDDO
              ENDDO
              CLOSE(IME)
          ENDDO
C*****
C      READ TRANSFORM MATRIX AND TRANSFORM MEASUREMENT MATRIX
C*****
C          TRANSFORM='TRANS. I N'
          OPEN(UNIT=I TR, FILE=TRANSFORM, STATUS='UNKNOWN')
C
C      MAKING TRANSFORMATION MATRIX
C
          DO II=1, 128
              READ(I TR, *) N_CONT, N_ANT
              NTRM(N_CONT+1)=N_ANT
          ENDDO
C
C      TRANSFORM MEASUREMENT MATRIX
C
          DO II=1, 128
              DO JJ=1, 128
                  MEA_T(NTRM(II), JJ)=MEA(II, JJ)
              ENDDO
          ENDDO
          DO JJ=1, 128
              DO II=1, 128
                  MEA_TR(II, NTRM(JJ))=MEA_T(II, JJ)
              ENDDO
          ENDDO
C*****
          DO NZ=1, 17
              DO NY=1, 16
                  DO NX=1, 8
                      WRITE(*, *) NZ, NY, NX
C*****
C      CALCULATE TRANSMITTING FOCUSING OPERATOR
C*****
          DO NK=1, 8
              DO NL=1, 16
                  CALL DIS3D(XT(NK), YT(NL), ZT(NK), XF(NX), YF(NY), ZF(NZ), D_TF)
                  FO_TKL=D_TF/CEXP(-J*KE(N)*D_TF)
                  I T((NK-1)*16+NL)=FO_TKL
              ENDDO
          ENDDO
C*****
C      CALCULATE RECEIVING FOCUSING OPERATOR
C*****
          DO NM=1, 8
              DO NN=1, 16
                  CALL DIS3D(XR(NM), YR(NN), ZR(NM), XF(NX), YF(NY), ZF(NZ), D_RF)
                  FO_RMN=D_RF/CEXP(-J*KE(N)*D_RF)
                  I R((NM-1)*16+NN)=FO_RMN
              ENDDO
          ENDDO
C*****
C      MULTIPLY FOCUSING OPERATOR AND MEASUREMENT MATRIX I T^T*MEA*I R
C*****

```

```

C      CALL ATBC(IT, MEA_TR, IR, 128, 128, E_F(NY, NX, NZ))
C
C          ENDDO
C          ENDDO
C          ENDDO
C          DO IZ=1, 17
C              DO IY=1, 16
C                  DO IX=1, 8
C                      SE_F(IY, IX, IZ)=SE_F(IY, IX, IZ)+E_F(IY, IX, IZ)
C                  ENDDO
C              ENDDO
C          ENDDO
C      ENDDO
C*****
C      END OF CALCULATION
C*****
C*****
C      CALCULATE ABSOLUTE VALUE OF SE_F
C*****
C          DO IZ=1, 17
C              DO IY=1, 16
C                  DO IX=1, 8
C                      ABS_SE_F(IY, IX, IZ)=CABS(SE_F(IY, IX, IZ))
C                  ENDDO
C              ENDDO
C          ENDDO
C*****
C      WRITE OUTPUT FILE
C*****
C      READ(IIN, *) NOUT
C      READ(IIN, *) (NSLICE(N), N=1, NOUT)
C      DO IIZ=1, NOUT
C          IZ=NSLICE(IIZ)
C          DO IY=1, 16
C              WRITE(OUT, 1000) (ABS_SE_F(IY, IX, IZ), IX=1, 8)
C          ENDDO
C      ENDDO
C      DO II=1, 16
C          DO JJ=1, 8
C              RE(II, JJ)=ABS_SE_F(II, JJ, 1)
C          ENDDO
C          DO JJ=12, 19
C              RE(II, JJ)=ABS_SE_F(II, JJ-11, 2)
C          ENDDO
C          DO JJ=23, 30
C              RE(II, JJ)=ABS_SE_F(II, JJ-22, 3)
C          ENDDO
C          DO JJ=34, 41
C              RE(II, JJ)=ABS_SE_F(II, JJ-33, 4)
C          ENDDO
C          DO JJ=45, 52
C              RE(II, JJ)=ABS_SE_F(II, JJ-44, 5)
C          ENDDO
C      ENDDO
C      DO II=20, 35
C          DO JJ=1, 8
C              RE(II, JJ)=ABS_SE_F(II-19, JJ, 5)
C          ENDDO
C          DO JJ=12, 19
C              RE(II, JJ)=ABS_SE_F(II-19, JJ-11, 6)
C          ENDDO
C          DO JJ=23, 30
C              RE(II, JJ)=ABS_SE_F(II-19, JJ-22, 7)
C          ENDDO
C          DO JJ=34, 41
C              RE(II, JJ)=ABS_SE_F(II-19, JJ-33, 8)
C          ENDDO
C          DO JJ=45, 52
C              RE(II, JJ)=ABS_SE_F(II-19, JJ-44, 10)
C          ENDDO
C      ENDDO
C      DO II=39, 54
C          DO JJ=1, 8
C              RE(II, JJ)=ABS_SE_F(II-38, JJ, 9)
C          ENDDO
C          DO JJ=12, 19
C              RE(II, JJ)=ABS_SE_F(II-38, JJ-11, 10)
C          ENDDO
C          DO JJ=23, 30
C              RE(II, JJ)=ABS_SE_F(II-38, JJ-22, 11)

```

```

                ENDDO
                DO JJ=34, 41
                    RE(II, JJ)=ABS_SE_F(II-38, JJ-33, 12)
                ENDDO
                DO JJ=45, 52
                    RE(II, JJ)=ABS_SE_F(II-38, JJ-44, 15)
                ENDDO
                ENDDO
                ENDDO
                DO II=58, 73
                    DO JJ=1, 8
                        RE(II, JJ)=ABS_SE_F(II-57, JJ, 13)
                    ENDDO
                    DO JJ=12, 19
                        RE(II, JJ)=ABS_SE_F(II-57, JJ-11, 14)
                    ENDDO
                    DO JJ=23, 30
                        RE(II, JJ)=ABS_SE_F(II-57, JJ-22, 15)
                    ENDDO
                    DO JJ=34, 41
                        RE(II, JJ)=ABS_SE_F(II-57, JJ-33, 16)
                    ENDDO
                ENDDO
                ENDDO
                DO II=1, 73
                    WRITE(IOUT, 1000) (RE(II, JJ), JJ=1, 41)
                ENDDO
C1000  FORMAT(8F20.10)
C*****
C      PLOT USING DISLIN
C*****
                CALL METAFI('CONS')
                CALL SETPAG('USAL')
                CALL DISINI
                CALL PAGERA
                CALL COMPLX
                ENDDO
                CALL MI XALF
                CALL TITLE('RECONSTRUCTED IMAGES AT Z-LEVELS', 1)
                CALL NAME('Y-AXIS', 'X')
                CALL NAME('X-AXIS', 'Y')
                ENDDO
                CALL SHDMOD('POLY', 'CONTUR')
                CALL AXSPOS(450, 2670)
                CALL GRAF(0.0, 73., 0.0, 10., 0.0, 41., 0.0, 10.)
                ENDDO
                DO II=1, 350
                    ZLEV(II)=0.+(II-1)*100.
                ENDDO
                ENDDO
                DO II=1, 73
                    XRAY(II)=1.+(II-1)
                ENDDO
                DO JJ=1, 41
                    YRAY(JJ)=1.+(JJ-1)
                ENDDO
                ENDDO
                CALL CONSHD(XRAY, 73, YRAY, 41, RE, ZLEV, 350)
                ENDDO
                CALL MESSAG('Z=-62.5mm', 500, 450)
                CALL MESSAG('Z=-75.0mm', 500, 800)
                CALL MESSAG('Z=-87.5mm', 500, 1180)
                CALL MESSAG('Z=-100.0mm', 500, 1560)
                ENDDO
                CALL MESSAG('Z=-12.5mm', 980, 450)
                CALL MESSAG('Z=-25.0mm', 980, 800)
                CALL MESSAG('Z=-37.5mm', 980, 1180)
                CALL MESSAG('Z=-50.0mm', 980, 1560)
                ENDDO
                CALL MESSAG('Z=+37.5mm', 1470, 450)
                CALL MESSAG('Z=+25.0mm', 1470, 800)
                CALL MESSAG('Z=+12.5mm', 1470, 1180)
                CALL MESSAG('Z=0.0mm', 1470, 1560)
                ENDDO
                CALL MESSAG('Z=+87.5mm', 1960, 450)
                CALL MESSAG('Z=+75.0mm', 1960, 800)
                CALL MESSAG('Z=+62.5mm', 1960, 1180)
                CALL MESSAG('Z=+50.0mm', 1960, 1560)
                ENDDO
                CALL MESSAG('QUIT', 2530, 1940)
                CALL HEIGHT(50)
                CALL TITLE

```

```

CALL SYMBOL(16, 2600, 2000)
CALL ENDGRF
C*****
C READ CURSOR CLICK LOCATION AND PLOT IN NEW WINDOW
C*****
1 CALL CSRPT1(NX, NY)
C
IF (NX. GT. 2532 .AND. NX. LT. 2668 .AND.
1 NY. GT. 1939 .AND. NY. LT. 2028)
2THEN
GOTO 10
ELSE IF (NX. GT. 491 .AND. NX. LT. 896 .AND.
1 NY. GT. 1544 .AND. NY. LT. 1823)
2THEN
DO II=1, 16
DO JJ=1, 8
RE_S(II, JJ)=ABS_SE_F(II, JJ, 1)
ENDDO
ENDDO
CALL CLSWIN (2)
CALL OPNWIN (2)
CALL TITLE('IMAGE AT Z=-100.0 mm', 1)
CALL NAME('Y-AXIS', 'X')
CALL NAME('X-AXIS', 'Y')
CALL AXSPOS(465, 1545)
CALL AXSLEN(1860, 930)
CALL GRAF(0.0, 200., 0.0, 25., 0.0, 100., 0.0, 10.)
DO II=1, 16
XRAY_S(II)=6.25+(II-1)*12.5
ENDDO
DO JJ=1, 8
YRAY_S(JJ)=6.25+(JJ-1)*12.5
ENDDO
CALL CONSHD(XRAY_S, 16, YRAY_S, 8, RE_S, ZLEV, 350)
CALL HEIGHT(50)
CALL TITLE
CALL ENDGRF
CALL SELWIN (1)
ELSE IF (NX. GT. 491 .AND. NX. LT. 896 .AND.
1 NY. GT. 1160 .AND. NY. LT. 1471)
2THEN
DO II=1, 16
DO JJ=1, 8
RE_S(II, JJ)=ABS_SE_F(II, JJ, 2)
ENDDO
ENDDO
CALL CLSWIN (2)
CALL OPNWIN (2)
CALL TITLE('IMAGE AT Z=-87.5 mm', 1)
CALL NAME('Y-AXIS', 'X')
CALL NAME('X-AXIS', 'Y')
CALL AXSPOS(465, 1545)
CALL AXSLEN(1860, 930)
CALL GRAF(0.0, 200., 0.0, 25., 0.0, 100., 0.0, 10.)
DO II=1, 16
XRAY_S(II)=6.25+(II-1)*12.5
ENDDO
DO JJ=1, 8
YRAY_S(JJ)=6.25+(JJ-1)*12.5
ENDDO
CALL CONSHD(XRAY_S, 16, YRAY_S, 8, RE_S, ZLEV, 350)
CALL HEIGHT(50)
CALL TITLE
CALL ENDGRF
CALL SELWIN (1)
ELSE IF (NX. GT. 491 .AND. NX. LT. 896 .AND.
1 NY. GT. 770 .AND. NY. LT. 1091)
2THEN
DO II=1, 16
DO JJ=1, 8
RE_S(II, JJ)=ABS_SE_F(II, JJ, 3)
ENDDO
ENDDO
CALL CLSWIN (2)
CALL OPNWIN (2)
CALL TITLE('IMAGE AT Z=-75.0 mm', 1)
CALL NAME('Y-AXIS', 'X')
CALL NAME('X-AXIS', 'Y')
CALL AXSPOS(465, 1545)
CALL AXSLEN(1860, 930)
CALL GRAF(0.0, 200., 0.0, 25., 0.0, 100., 0.0, 10.)

```

```

DO II=1,16
  XRAY_S(II)=6.25+(II-1)*12.5
ENDDO
DO JJ=1,8
  YRAY_S(JJ)=6.25+(JJ-1)*12.5
ENDDO
CALL CONSHD(XRAY_S,16,YRAY_S,8,RE_S,ZLEV,350)
CALL HEIGHT(50)
CALL TITLE
CALL ENDGRF
CALL SELWIN(1)
ELSE IF (NX.GT.491 .AND. NX.LT.896 .AND.
1      NY.GT.422 .AND. NY.LT.700)
2THEN
DO II=1,16
  DO JJ=1,8
    RE_S(II,JJ)=ABS_SE_F(II,JJ,4)
  ENDDO
ENDDO
CALL CLSWIN(2)
CALL OPNWIN(2)
CALL TITLE('IMAGE AT Z=-62.5mm',1)
CALL NAME('Y-AXIS','X')
CALL NAME('X-AXIS','Y')
CALL AXSPOS(465,1545)
CALL AXSLEN(1860,930)
CALL GRAF(0.0,200.,0.0,25.,0.0,100.,0.0,10.)
DO II=1,16
  XRAY_S(II)=6.25+(II-1)*12.5
ENDDO
DO JJ=1,8
  YRAY_S(JJ)=6.25+(JJ-1)*12.5
ENDDO
CALL CONSHD(XRAY_S,16,YRAY_S,8,RE_S,ZLEV,350)
CALL HEIGHT(50)
CALL TITLE
CALL ENDGRF
CALL SELWIN(1)
ELSE IF (NX.GT.948 .AND. NX.LT.1383 .AND.
1      NY.GT.1544 .AND. NY.LT.1823)
2THEN
DO II=1,16
  DO JJ=1,8
    RE_S(II,JJ)=ABS_SE_F(II,JJ,5)
  ENDDO
ENDDO
CALL CLSWIN(2)
CALL OPNWIN(2)
CALL TITLE('IMAGE AT Z=-50.0 mm',1)
CALL NAME('Y-AXIS','X')
CALL NAME('X-AXIS','Y')
CALL AXSPOS(465,1545)
CALL AXSLEN(1860,930)
CALL GRAF(0.0,200.,0.0,25.,0.0,100.,0.0,10.)
DO II=1,16
  XRAY_S(II)=6.25+(II-1)*12.5
ENDDO
DO JJ=1,8
  YRAY_S(JJ)=6.25+(JJ-1)*12.5
ENDDO
CALL CONSHD(XRAY_S,16,YRAY_S,8,RE_S,ZLEV,350)
CALL HEIGHT(50)
CALL TITLE
CALL ENDGRF
CALL SELWIN(1)
ELSE IF (NX.GT.948 .AND. NX.LT.1383 .AND.
1      NY.GT.1160 .AND. NY.LT.1471)
2THEN
DO II=1,16
  DO JJ=1,8
    RE_S(II,JJ)=ABS_SE_F(II,JJ,6)
  ENDDO
ENDDO
CALL CLSWIN(2)
CALL OPNWIN(2)
CALL TITLE('IMAGE AT Z=-37.5 mm',1)
CALL NAME('Y-AXIS','X')
CALL NAME('X-AXIS','Y')
CALL AXSPOS(465,1545)
CALL AXSLEN(1860,930)
CALL GRAF(0.0,200.,0.0,25.,0.0,100.,0.0,10.)

```

```

DO II=1,16
  XRAY_S(II)=6.25+(II-1)*12.5
ENDDO
DO JJ=1,8
  YRAY_S(JJ)=6.25+(JJ-1)*12.5
ENDDO
CALL CONSHD(XRAY_S,16,YRAY_S,8,RE_S,ZLEV,350)
CALL HEIGHT(50)
CALL TITLE
CALL ENDGRF
CALL SELWIN(1)
ELSE IF (NX.GT.948 .AND. NX.LT.1383 .AND.
1 NY.GT.770 .AND. NY.LT.1091)
2THEN
DO II=1,16
  DO JJ=1,8
    RE_S(II,JJ)=ABS_SE_F(II,JJ,7)
  ENDDO
ENDDO
CALL CLSWIN(2)
CALL OPNWIN(2)
CALL TITLE('IMAGE AT Z=-25.0 mm',1)
CALL NAME('Y-AXIS','X')
CALL NAME('X-AXIS','Y')
CALL AXSPOS(465,1545)
CALL AXSLEN(1860,930)
CALL GRAF(0.0,200.,0.0,25.,0.0,100.,0.0,10.)
DO II=1,16
  XRAY_S(II)=6.25+(II-1)*12.5
ENDDO
DO JJ=1,8
  YRAY_S(JJ)=6.25+(JJ-1)*12.5
ENDDO
CALL CONSHD(XRAY_S,16,YRAY_S,8,RE_S,ZLEV,350)
CALL HEIGHT(50)
CALL TITLE
CALL ENDGRF
CALL SELWIN(1)
ELSE IF (NX.GT.948 .AND. NX.LT.1383 .AND.
1 NY.GT.422 .AND. NY.LT.700)
2THEN
DO II=1,16
  DO JJ=1,8
    RE_S(II,JJ)=ABS_SE_F(II,JJ,8)
  ENDDO
ENDDO
CALL CLSWIN(2)
CALL OPNWIN(2)
CALL TITLE('IMAGE AT Z=-12.5 mm',1)
CALL NAME('Y-AXIS','X')
CALL NAME('X-AXIS','Y')
CALL AXSPOS(465,1545)
CALL AXSLEN(1860,930)
CALL GRAF(0.0,200.,0.0,25.,0.0,100.,0.0,10.)
DO II=1,16
  XRAY_S(II)=6.25+(II-1)*12.5
ENDDO
DO JJ=1,8
  YRAY_S(JJ)=6.25+(JJ-1)*12.5
ENDDO
CALL CONSHD(XRAY_S,16,YRAY_S,8,RE_S,ZLEV,350)
CALL HEIGHT(50)
CALL TITLE
CALL ENDGRF
CALL SELWIN(1)
ELSE IF (NX.GT.1432 .AND. NX.LT.1864 .AND.
1 NY.GT.1544 .AND. NY.LT.1823)
2THEN
DO II=1,16
  DO JJ=1,8
    RE_S(II,JJ)=ABS_SE_F(II,JJ,9)
  ENDDO
ENDDO
CALL CLSWIN(2)
CALL OPNWIN(2)
CALL TITLE('IMAGE AT Z=0.0 mm',1)
CALL NAME('Y-AXIS','X')
CALL NAME('X-AXIS','Y')
CALL AXSPOS(465,1545)
CALL AXSLEN(1860,930)
CALL GRAF(0.0,200.,0.0,25.,0.0,100.,0.0,10.)

```

```

DO II=1,16
  XRAY_S(II)=6.25+(II-1)*12.5
ENDDO
DO JJ=1,8
  YRAY_S(JJ)=6.25+(JJ-1)*12.5
ENDDO
CALL CONSHD(XRAY_S,16,YRAY_S,8,RE_S,ZLEV,350)
CALL HEIGHT(50)
CALL TITLE
CALL ENDGRF
CALL SELWIN(1)
ELSE IF(NX.GT.1432 .AND. NX.LT.1864 .AND.
1 NY.GT.1160 .AND. NY.LT.1471)
2THEN
DO II=1,16
  DO JJ=1,8
    RE_S(II,JJ)=ABS_SE_F(II,JJ,10)
  ENDDO
ENDDO
CALL CLSWIN(2)
CALL OPNWIN(2)
CALL TITLE('IMAGE AT Z=+12.5mm',1)
CALL NAME('Y-AXIS','X')
CALL NAME('X-AXIS','Y')
CALL AXSPOS(465,1545)
CALL AXSLEN(1860,930)
CALL GRAF(0.0,200.,0.0,25.,0.0,100.,0.0,10.)
DO II=1,16
  XRAY_S(II)=6.25+(II-1)*12.5
ENDDO
DO JJ=1,8
  YRAY_S(JJ)=6.25+(JJ-1)*12.5
ENDDO
CALL CONSHD(XRAY_S,16,YRAY_S,8,RE_S,ZLEV,350)
CALL HEIGHT(50)
CALL TITLE
CALL ENDGRF
CALL SELWIN(1)
ELSE IF(NX.GT.1432 .AND. NX.LT.1864 .AND.
1 NY.GT.770 .AND. NY.LT.1091)
2THEN
DO II=1,16
  DO JJ=1,8
    RE_S(II,JJ)=ABS_SE_F(II,JJ,11)
  ENDDO
ENDDO
CALL CLSWIN(2)
CALL OPNWIN(2)
CALL TITLE('IMAGE AT Z=+25.0mm',1)
CALL NAME('Y-AXIS','X')
CALL NAME('X-AXIS','Y')
CALL AXSPOS(465,1545)
CALL AXSLEN(1860,930)
CALL GRAF(0.0,200.,0.0,25.,0.0,100.,0.0,10.)
DO II=1,16
  XRAY_S(II)=6.25+(II-1)*12.5
ENDDO
DO JJ=1,8
  YRAY_S(JJ)=6.25+(JJ-1)*12.5
ENDDO
CALL CONSHD(XRAY_S,16,YRAY_S,8,RE_S,ZLEV,350)
CALL HEIGHT(50)
CALL TITLE
CALL ENDGRF
CALL SELWIN(1)
ELSE IF(NX.GT.1432 .AND. NX.LT.1864 .AND.
1 NY.GT.422 .AND. NY.LT.700)
2THEN
DO II=1,16
  DO JJ=1,8
    RE_S(II,JJ)=ABS_SE_F(II,JJ,12)
  ENDDO
ENDDO
CALL CLSWIN(2)
CALL OPNWIN(2)
CALL TITLE('IMAGE AT Z=+37.5mm',1)
CALL NAME('Y-AXIS','X')
CALL NAME('X-AXIS','Y')
CALL AXSPOS(465,1545)
CALL AXSLEN(1860,930)
CALL GRAF(0.0,200.,0.0,25.,0.0,100.,0.0,10.)

```

```

DO II=1,16
  XRAY_S(II)=6.25+(II-1)*12.5
ENDDO
DO JJ=1,8
  YRAY_S(JJ)=6.25+(JJ-1)*12.5
ENDDO
CALL CONSHD(XRAY_S,16,YRAY_S,8,RE_S,ZLEV,350)
CALL HEIGHT(50)
CALL TITLE
CALL ENDGRF
CALL SELWIN(1)
ELSE IF(NX.GT.1917 .AND. NX.LT.2324 .AND.
1 NY.GT.1544 .AND. NY.LT.1823)
2THEN
DO II=1,16
  DO JJ=1,8
    RE_S(II,JJ)=ABS_SE_F(II,JJ,13)
  ENDDO
ENDDO
CALL CLSWIN(2)
CALL OPNWIN(2)
CALL TITLE('IMAGE AT Z=+50.0mm',1)
CALL NAME('Y-AXIS','X')
CALL NAME('X-AXIS','Y')
CALL AXSPOS(465,1545)
CALL AXSLEN(1860,930)
CALL GRAF(0.0,200.,0.0,25.,0.0,100.,0.0,10.)
DO II=1,16
  XRAY_S(II)=6.25+(II-1)*12.5
ENDDO
DO JJ=1,8
  YRAY_S(JJ)=6.25+(JJ-1)*12.5
ENDDO
CALL CONSHD(XRAY_S,16,YRAY_S,8,RE_S,ZLEV,350)
CALL HEIGHT(50)
CALL TITLE
CALL ENDGRF
CALL SELWIN(1)
ELSE IF(NX.GT.1917 .AND. NX.LT.2324 .AND.
1 NY.GT.1160 .AND. NY.LT.1471)
2THEN
DO II=1,16
  DO JJ=1,8
    RE_S(II,JJ)=ABS_SE_F(II,JJ,14)
  ENDDO
ENDDO
CALL CLSWIN(2)
CALL OPNWIN(2)
CALL TITLE('IMAGE AT Z=+62.5mm',1)
CALL NAME('Y-AXIS','X')
CALL NAME('X-AXIS','Y')
CALL AXSPOS(465,1545)
CALL AXSLEN(1860,930)
CALL GRAF(0.0,200.,0.0,25.,0.0,100.,0.0,10.)
DO II=1,16
  XRAY_S(II)=6.25+(II-1)*12.5
ENDDO
DO JJ=1,8
  YRAY_S(JJ)=6.25+(JJ-1)*12.5
ENDDO
CALL CONSHD(XRAY_S,16,YRAY_S,8,RE_S,ZLEV,350)
CALL HEIGHT(50)
CALL TITLE
CALL ENDGRF
CALL SELWIN(1)
ELSE IF(NX.GT.1917 .AND. NX.LT.2324 .AND.
1 NY.GT.770 .AND. NY.LT.1091)
2THEN
DO II=1,16
  DO JJ=1,8
    RE_S(II,JJ)=ABS_SE_F(II,JJ,15)
  ENDDO
ENDDO
CALL CLSWIN(2)
CALL OPNWIN(2)
CALL TITLE('IMAGE AT Z=+75.0mm',1)
CALL NAME('Y-AXIS','X')
CALL NAME('X-AXIS','Y')
CALL AXSPOS(465,1545)
CALL AXSLEN(1860,930)
CALL GRAF(0.0,200.,0.0,25.,0.0,100.,0.0,10.)

```

```

DO II=1,16
  XRAY_S(II)=6.25+(II-1)*12.5
ENDDO
DO JJ=1,8
  YRAY_S(JJ)=6.25+(JJ-1)*12.5
ENDDO
CALL CONSHD(XRAY_S,16,YRAY_S,8,RE_S,ZLEV,350)
CALL HEIGHT(50)
CALL TITLE
CALL ENDGRF
CALL SELWIN(1)
ELSE IF(NX.GT.1917.AND. NX.LT.2324.AND.
1      NY.GT.422.AND. NY.LT.700)
2THEN
  DO II=1,16
    DO JJ=1,8
      RE_S(II,JJ)=ABS_SE_F(II,JJ,16)
    ENDDO
  ENDDO
  CALL CLSWIN(2)
  CALL OPNWIN(2)
  CALL TITLE('IMAGE AT Z=+87.5mm',1)
  CALL NAME('Y-AXIS','X')
  CALL NAME('X-AXIS','Y')
  CALL AXSPOS(465,1545)
  CALL AXSLEN(1860,930)
  CALL GRAF(0.0,200.,0.0,25.,0.0,100.,0.0,10.)
  DO II=1,16
    XRAY_S(II)=6.25+(II-1)*12.5
  ENDDO
  DO JJ=1,8
    YRAY_S(JJ)=6.25+(JJ-1)*12.5
  ENDDO
  CALL CONSHD(XRAY_S,16,YRAY_S,8,RE_S,ZLEV,350)
  CALL HEIGHT(50)
  CALL TITLE
  CALL ENDGRF
  CALL SELWIN(1)
ENDIF
C
GOTO 1
C*****
C  CLOSE DISLIN
C*****
10  CALL CLSWIN(2)
C
CALL DISFIN
C
1000  FORMAT(52F15.5)
C*****
C  END OF PROGRAM
C*****
END

C*****
SUBROUTINE DIS3D(X1,Y1,Z1,X2,Y2,Z2,D)
C*****
D=SQRT((X2-X1)**2+(Y2-Y1)**2+(Z2-Z1)**2)
C
RETURN
END
C
C*****
SUBROUTINE ATBC(A,B,C,IA,IC,R)
C*****
COMPLEX A(IA),B(IA,IC),C(IC),R,TMP,TMP1
COMPLEX ATB(IC)
COMPLEX J
C
J=(0.,1.)
R=0.+J*0.
DO II=1,IC
  ATB(II)=0.+J*0.
  DO IJ=1,IA
    TMP=A(IJ)*B(IJ,II)
    ATB(II)=ATB(II)+TMP
  ENDDO
  TMP1=ATB(II)*C(II)
  R=R+TMP1
ENDDO

```

```

C          RETURN
          END
C
C*****
C          SUBROUTINE OPENFILE
C*****
          CHARACTER*20 INFIL E, OUTFILE
          CHARACTER*16 FROOT
          LOGICAL EFILE
          COMMON /I OUNIT/I IN, I OUT

C          I IN=5
          I OUT=6

C          WRITE(*, *) ' INPUT FILENAME : '
C          FROOT=
C          READ ' (A)', FROOT

C          I=0
C12         I=I+1
          IF (FROOT(I:I).EQ.' ') THEN
C          LEN_FROOT=I-1
          GO TO 20
C          END IF
C15         GOTO 12

C20         INFIL E = FROOT(1: LEN_FROOT)//'. IN'
          OUTFILE = FROOT(1: LEN_FROOT)//'. O'

C          INQUIRE(FILE=INFIL E, EXIST=EFILE)
C          IF( EFILE ) THEN
C          OPEN(UNIT=I IN, FILE=INFIL E, STATUS=' OLD' )
C          ELSE
C          WRITE(*, *) ' *** error : cannot find ',infile
C          GO TO 10
C          END IF
C
C          OPEN(UNIT=I IN, FILE=INFIL E, STATUS=' UNKNOWN' )
          OPEN(UNIT=I OUT, FILE=' OUTPUT. OUT', STATUS=' UNKNOWN' )

C          RETURN
          END
C*****

```

Appendix C

MANUAL OF CONTROL PROGRAM

Since the LabView is a graphical programming language, the flow of the programming is introduced as the following pictures and notes. The interface will be introduced after the programming flow.

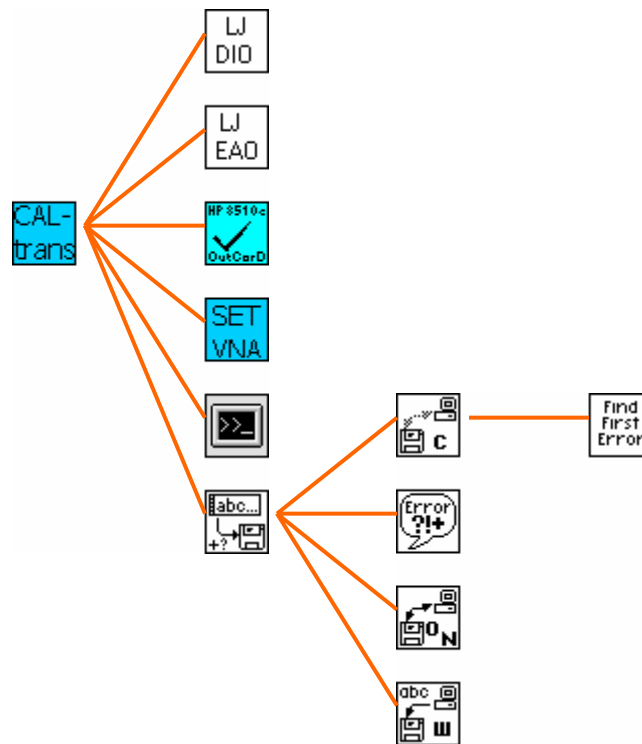


Figure C.1 Hierarchy of the LabView program ‘caltrans.vi’

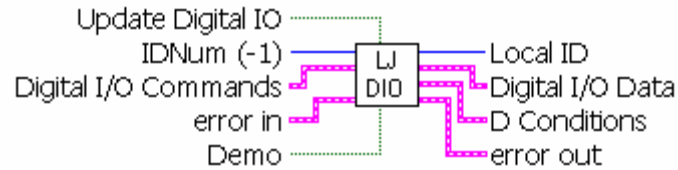
The ‘caltrans.vi’ program is using file sub functions, which are displayed in **Figure C.1**, respectively, DigitalIO.vi, EanalogOut.vi, HP8510C Output Corrected Data.vi, System Exec.vi, and Write Characters To File.vi. Write Characters To File.vi has additional 2 levels of sub functions and since it is a system function of LabView 6i for those functions. please see the help manual of LabView 6i for those functions.

Sub functions are illustrated accordingly; DigitalIO and EanalogOut are functions of LabJack drivers, please refer more details in the manual of LabJack.

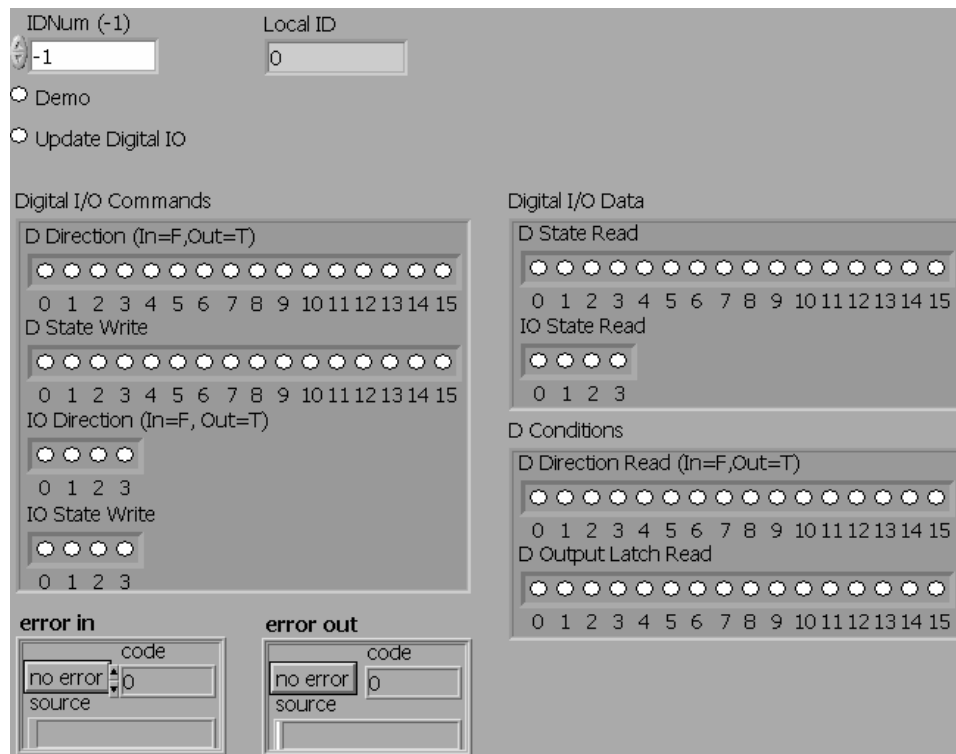
C.1 DigitalIO.vi

Reads and writes to all 20 Digital I/O. execution time for this function is 20 milliseconds or less.

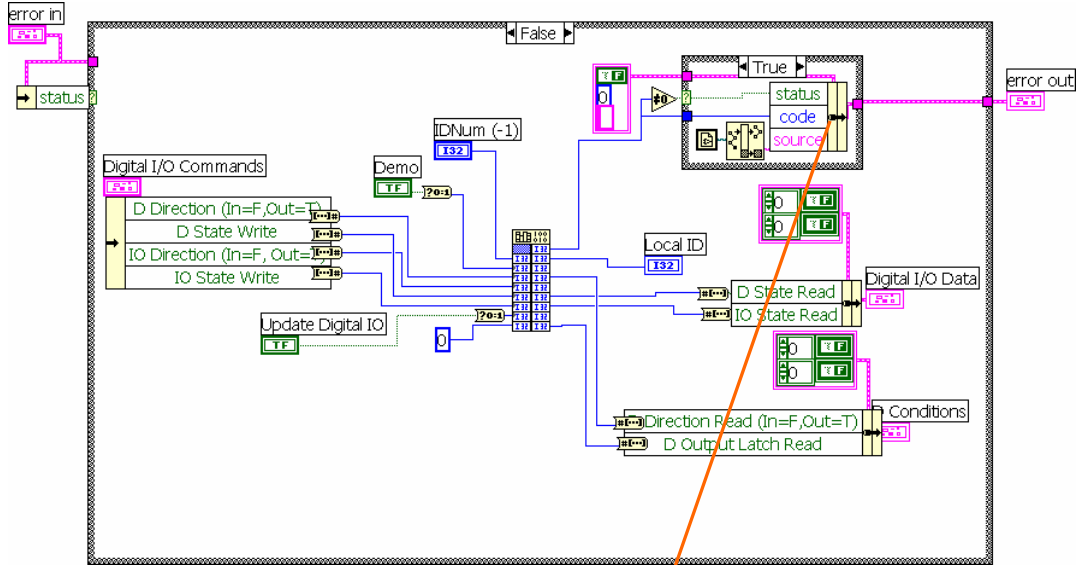
Connector Panel



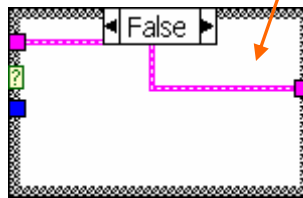
Front Panel



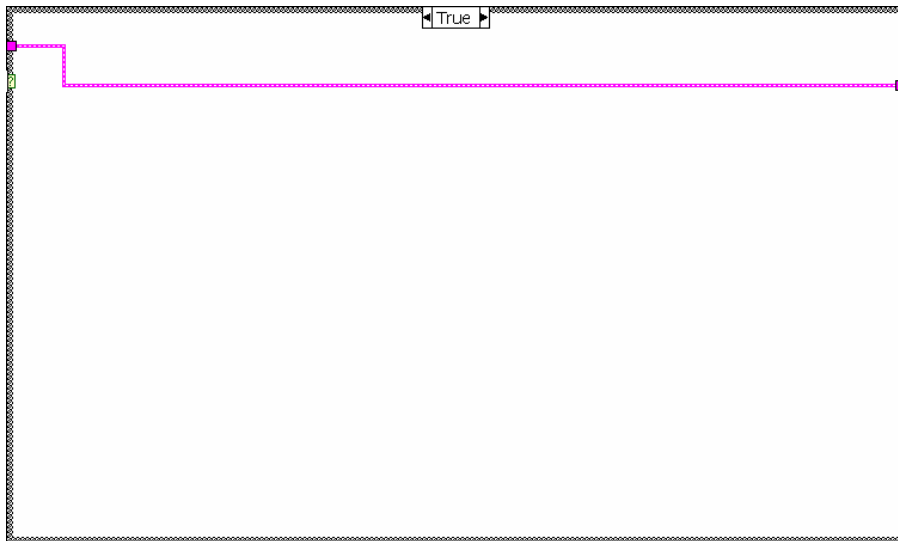
Block Diagram



(a)



(b)



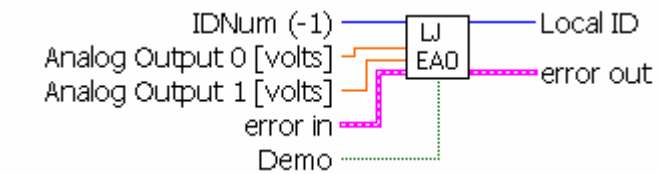
(c)

(b) is the false case of the inner case in (a), shown by the arrow and (c) is the true case of the outer case in the (a).

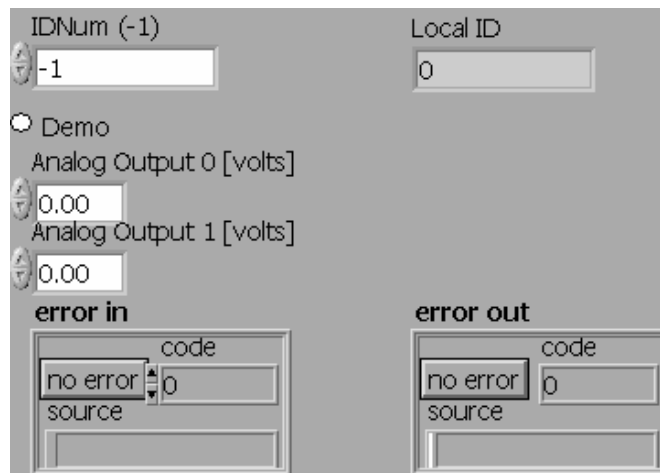
C.2 EAnalogOut.vi

Easy function. This is a simplified of AOUpdate. Sets the voltage of both analog outputs. Execution time for this function is 20 milliseconds or less.

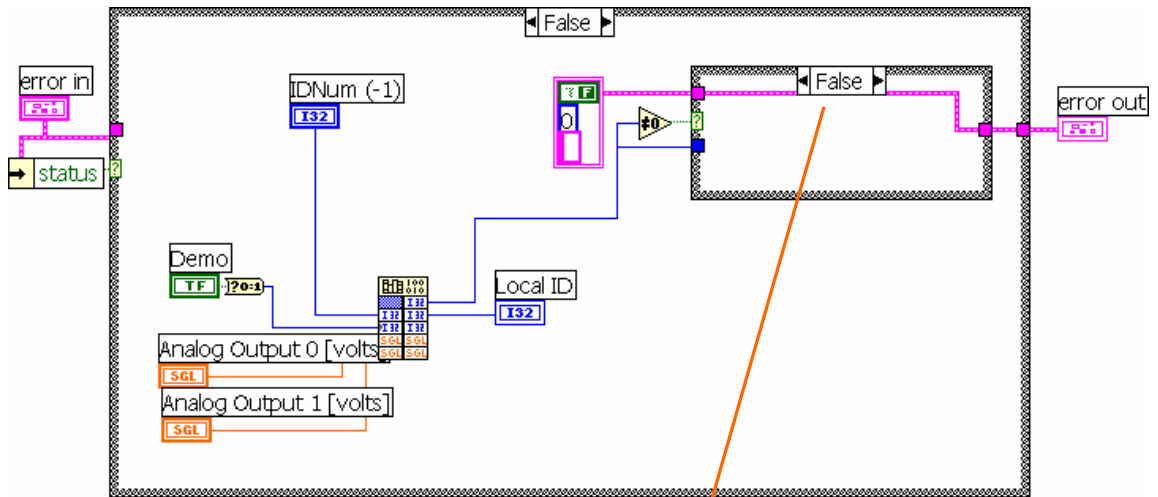
Connector Panel



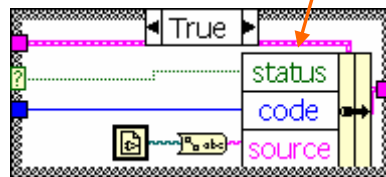
Front Panel



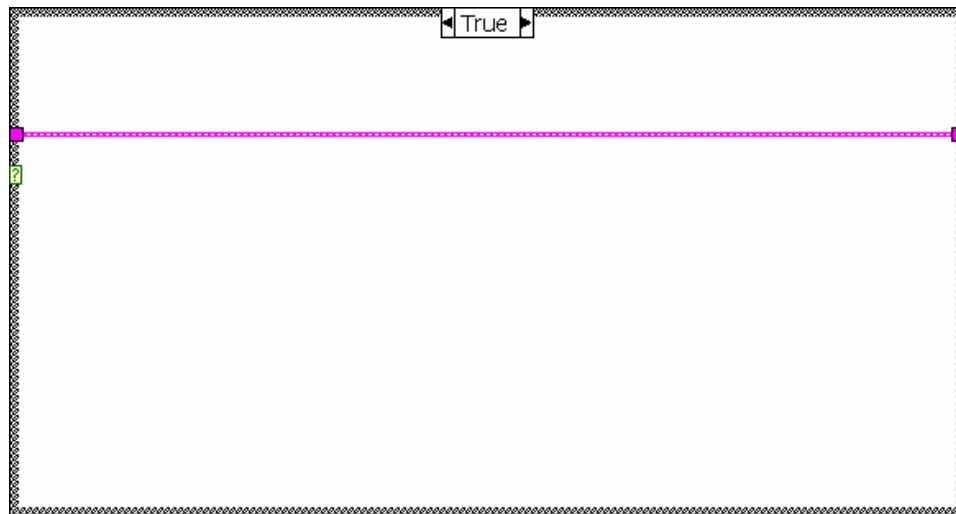
Block Diagram



(a)



(b)



(c)

(b) is the true case of the inner case in (a), shown by the arrow and (c) is the true case of the outer case in the (a).

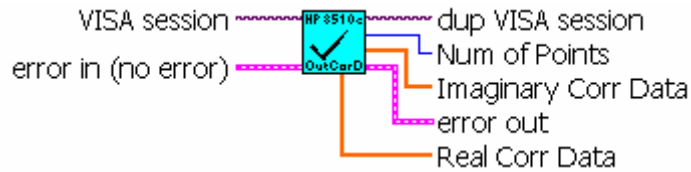
C.3 HP8510C Output Corrected Data.vi

This function outputs real/imaginary pairs from selected channel corrected data memory. In addition to rationing and averaging, corrected data has been through:

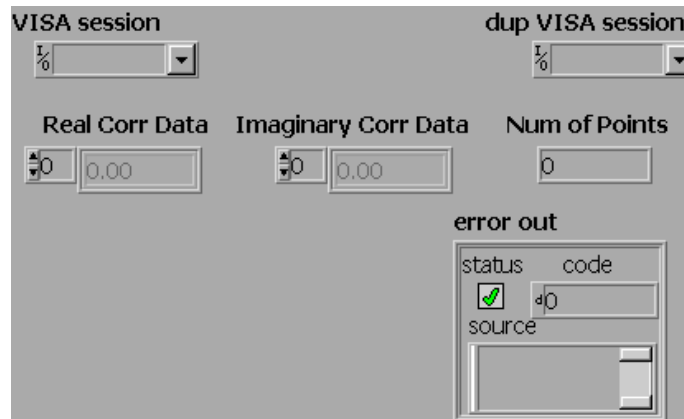
- Time Domain
- Calibration
- Table Delay, electrical delay
- Magnitude offset

Remember that these features must be active to affect the data.

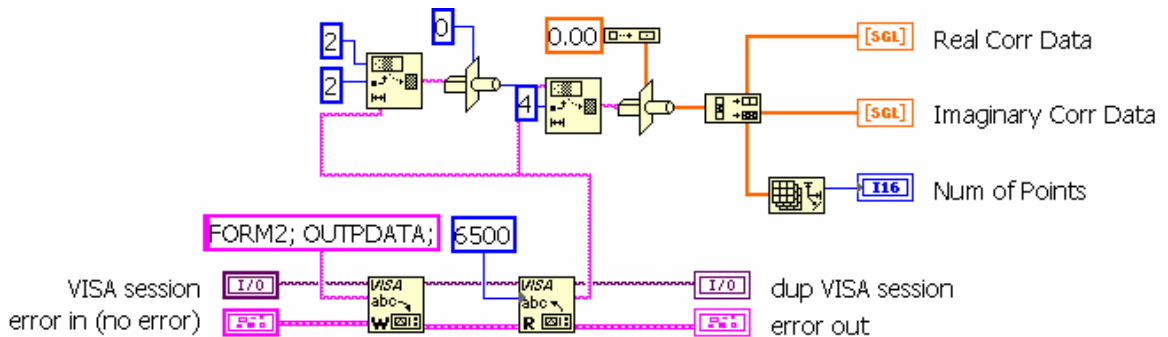
Connector Panel



Front Panel



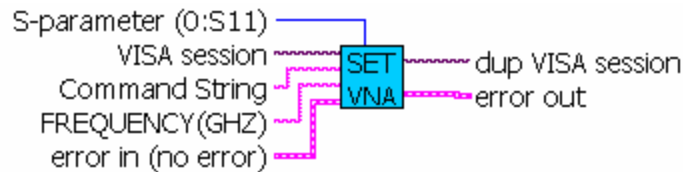
Block Diagram



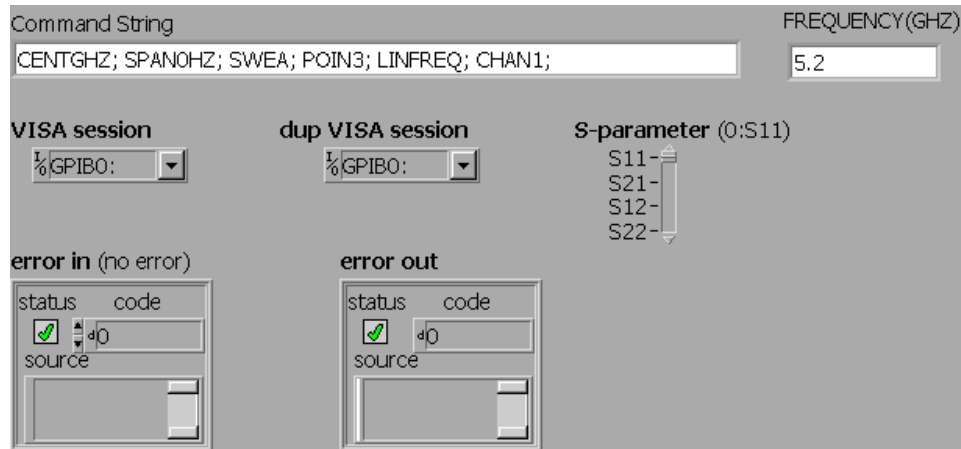
C.4 HP8722ES Set freq Spara.vi

The function initializes the network analyzer to use Channel 1, center frequency and span as specified, with minimum sweep time and number of points 3, display linear frequency and take the S parameter as specified.

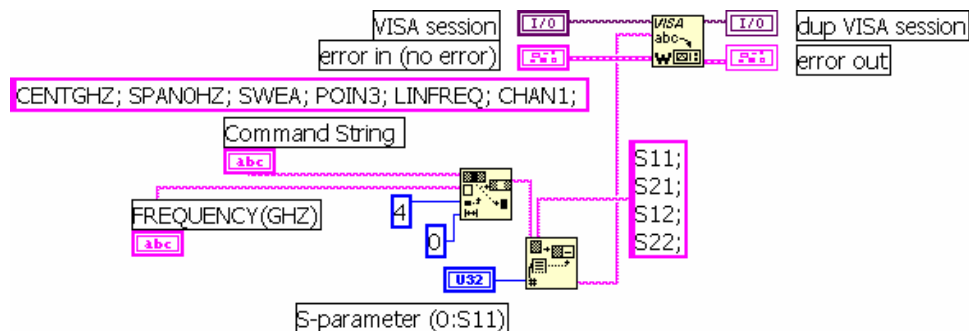
Connector Panel



Front Panel



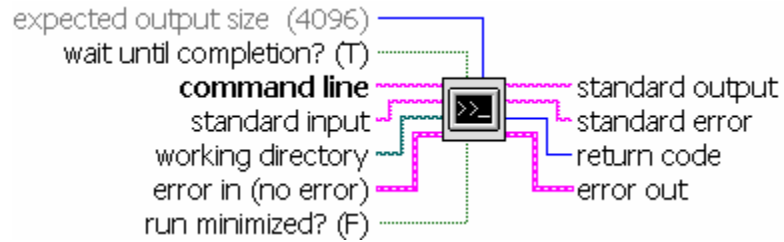
Block Diagram



C.5 System Exec.vi

Executes a system command. Please see the LabVIEW help manual for more details.

Connector Panel



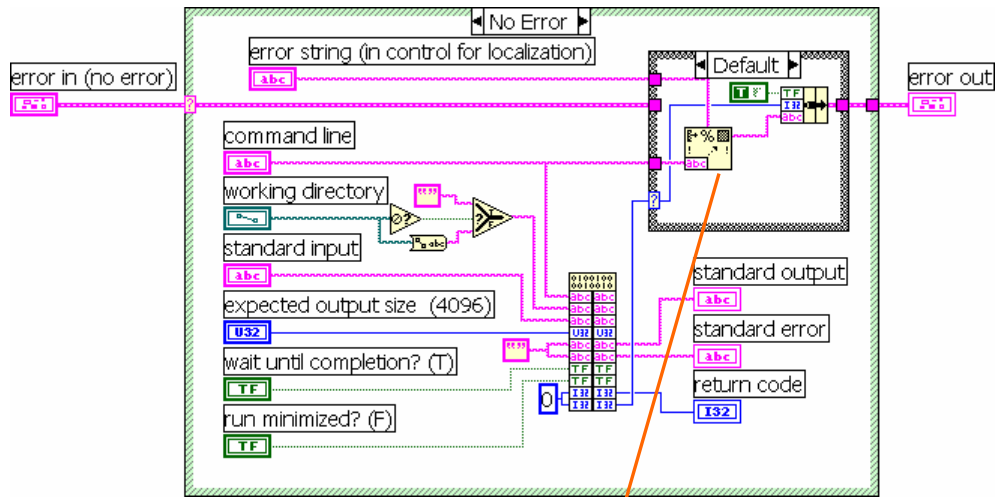
Front Panel

The front panel of the System Exec.vi function includes the following controls and indicators:

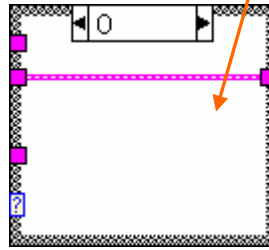
- command line:** A text input field.
- working directory:** A text input field containing "%."
- standard input:** A scrollable text area.
- standard output:** A scrollable text area.
- standard error:** A scrollable text area.
- expected output size (4096):** A numeric control set to 4096.
- return code:** A numeric control set to 0.
- wait until completion? (T):** A boolean control set to True.
- run minimized? (F):** A boolean control set to False.
- error in (no error):** A status indicator showing a green checkmark and a code of 0.
- error out:** A status indicator showing a green checkmark and a code of 0.

Note: If wait until completion? is False, standard input, output, and error will be ignored.

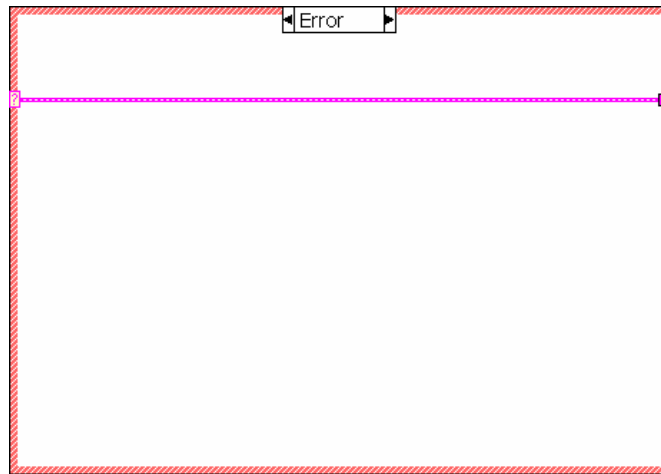
Block Diagram



(a)



(b)



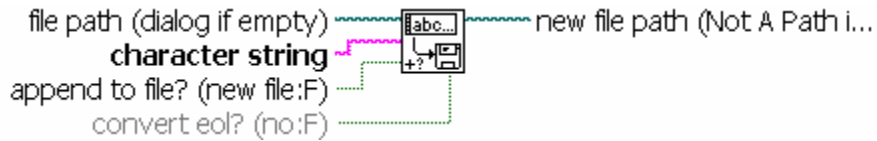
(c)

(b) is the 0 case of the inner case in (a), shown by the arrow and (c) is the error case of the outer case in the (a).

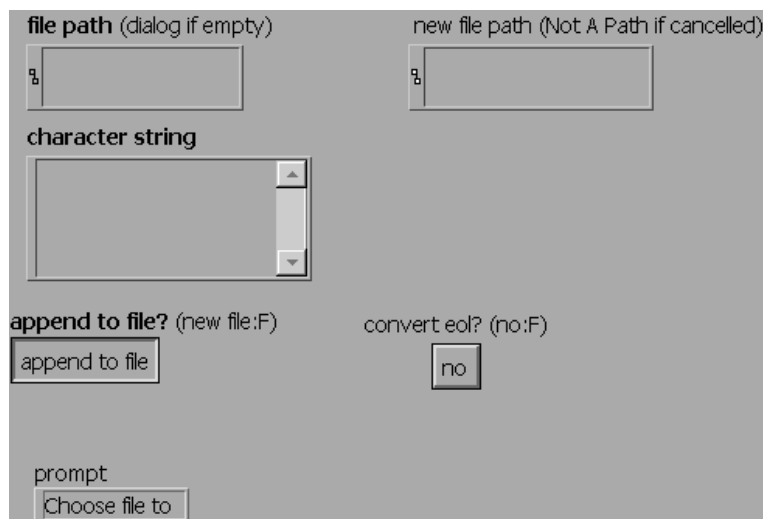
C.6 Write Characters To File.vi

Writes a character string to a new byte stream file or appends the string to an existing file. The VI opens or creates the file before writing to it and closes it afterwards. Please see LabView 6i help manual for more details.

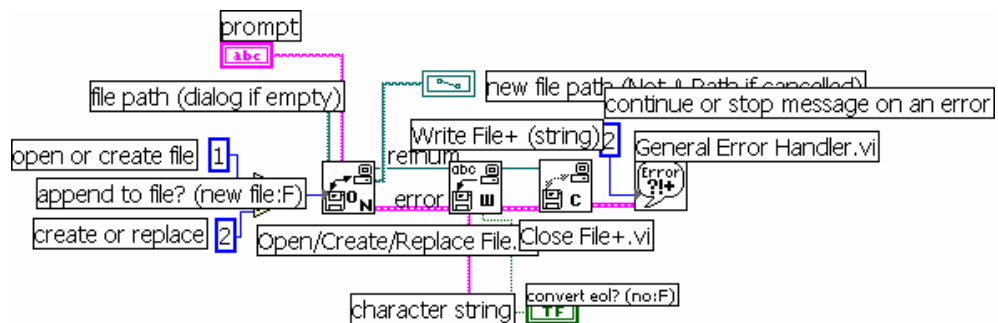
Connector Panel



Front Panel



Block Diagram



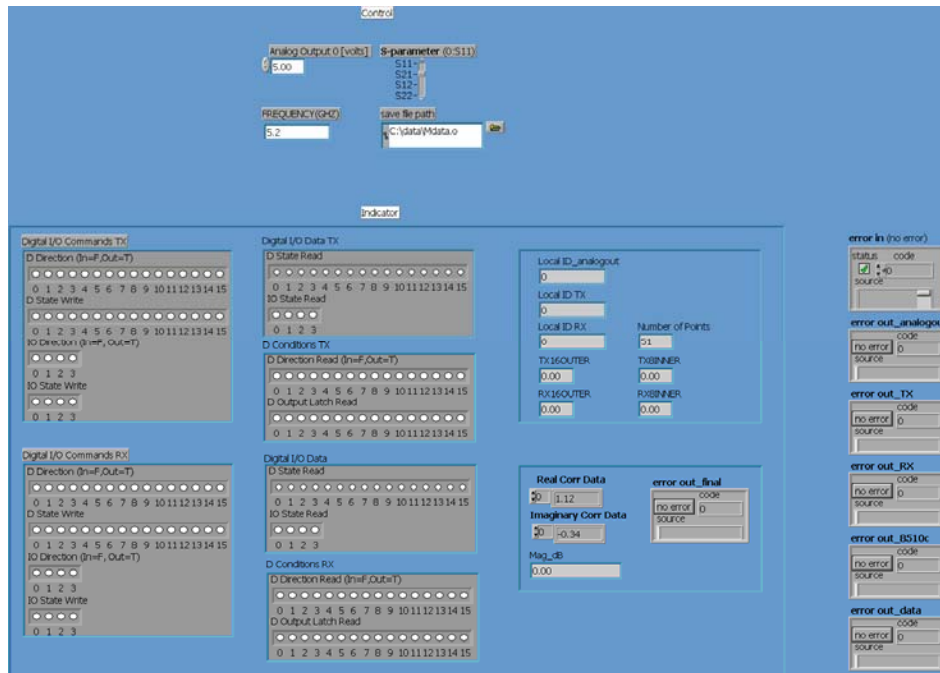
C.7 caltrans.vi

The final function uses the above functions. Details provided here.

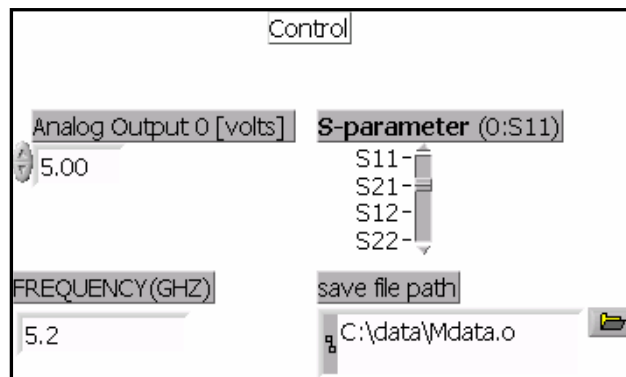
Connector Panel



Front Panel



(a)

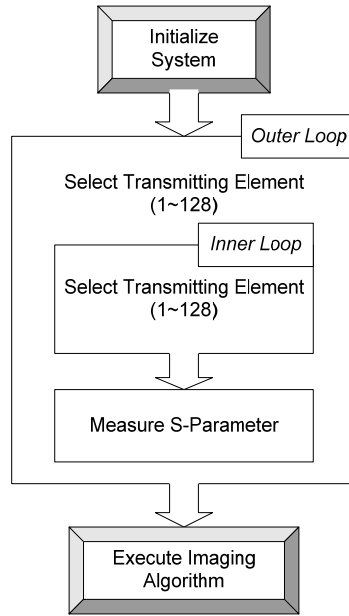


(b)

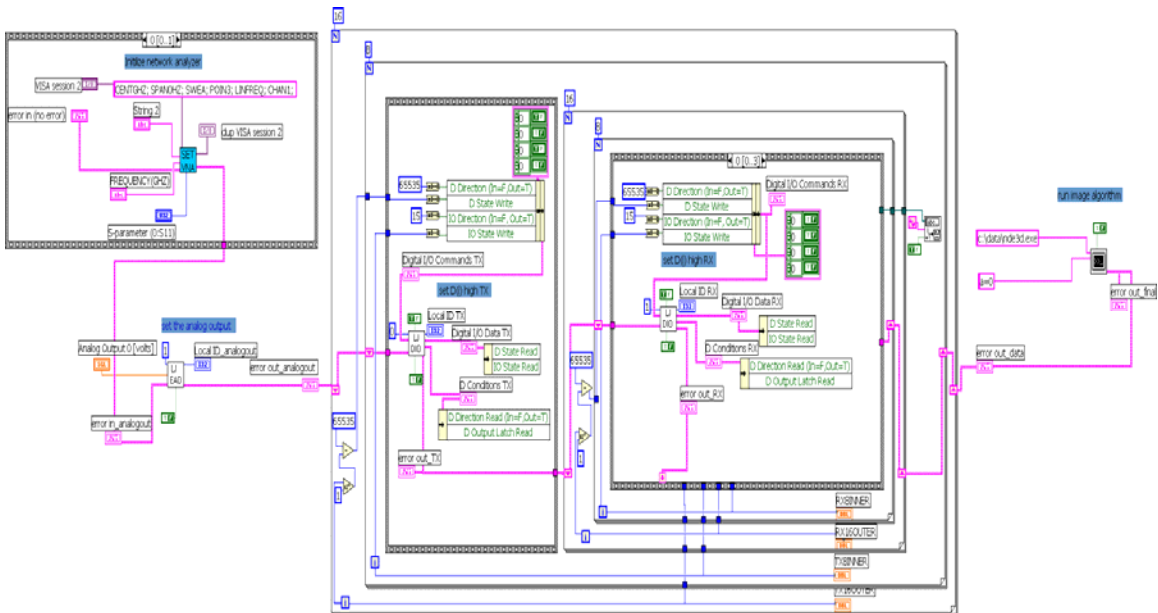
The front panel includes two parts, controls and indicators. For simple case, the controls are variables controllable, while the indicators are variable indicating the status

of data flow, to give us an idea of how the flow is going on now. In part b, the controls are 4 of them, Analog output 0 S parameter, Frequency in GHz, and save file path. The default value is shown above too.

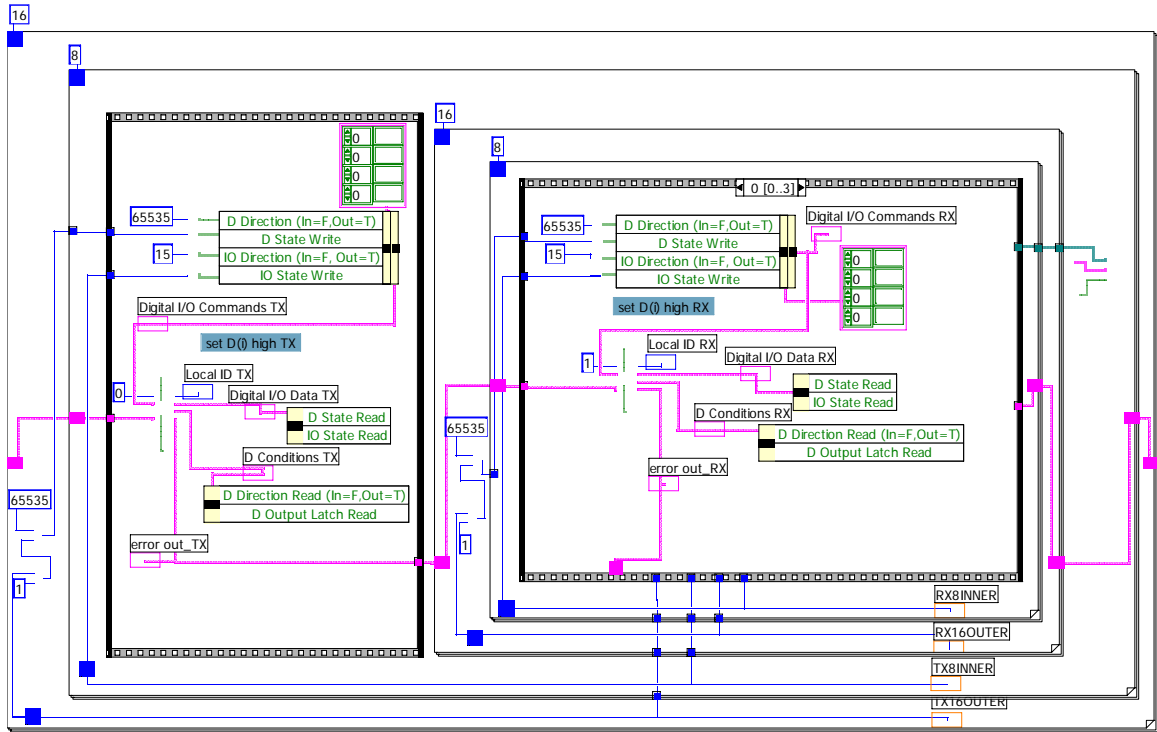
Block Diagram



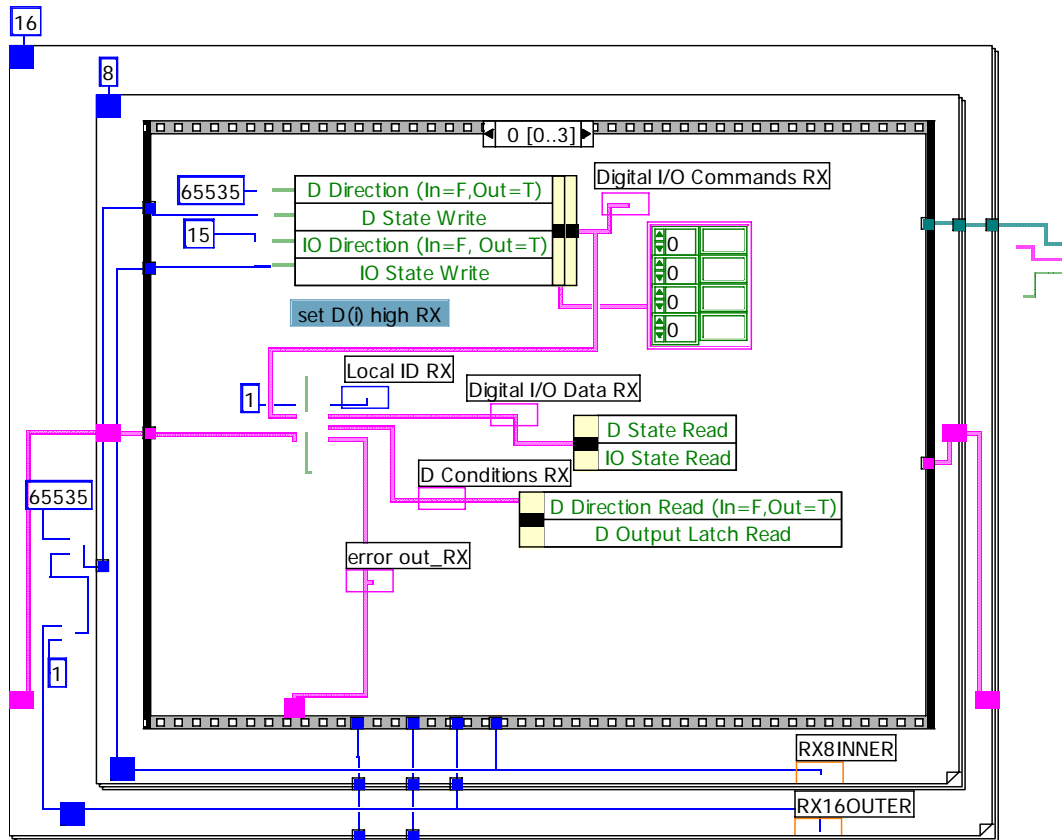
(a)



(b)



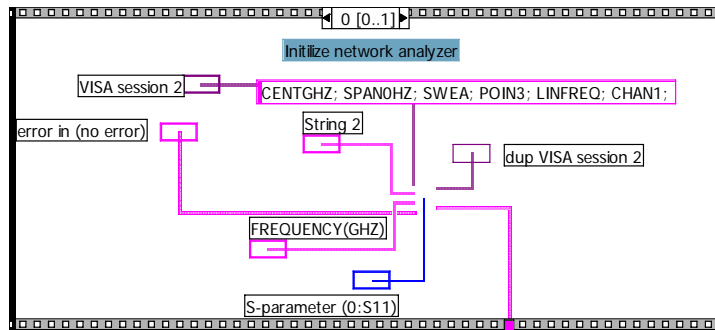
(c)



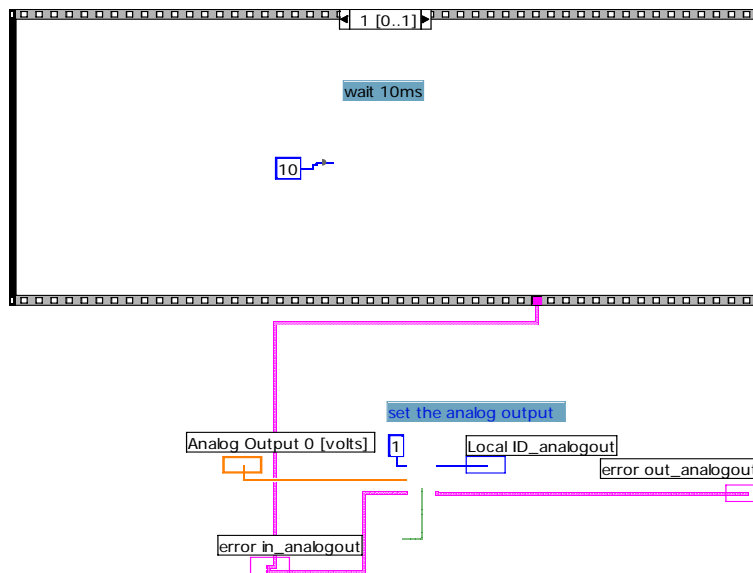
(d)

(a) is the schematic of the block diagram (b), as we compare them, we notice that the three parts are displayed as initialization, taking measurement and running the image algorithm. In (b) 3 blocks are illustrated, the block before the loops is the initialization, the loops are taking measurement and the block after it is to run the image algorithm. Now we see the close-ups of those blocks and we mark them with numbers so that the flow can be illustrated. (c) is the overall measurement taking part, and (d) is the inner loops of receiving antenna arrays. Inside(c), it contains (d) part and a block before (d) part to set the transmitting antenna arrays. In (d), inside the two loops, there is a frame structure, as what in (a), this frame has 2 functions, set the receiving antenna arrays and take the s parameters. The frames are shown in the following steps.

C.8 Initialization

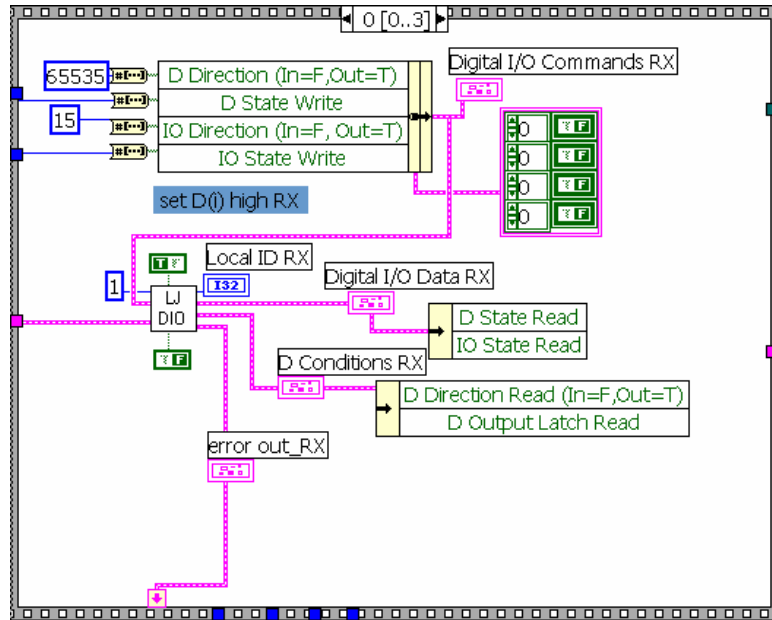


(a) Step 1



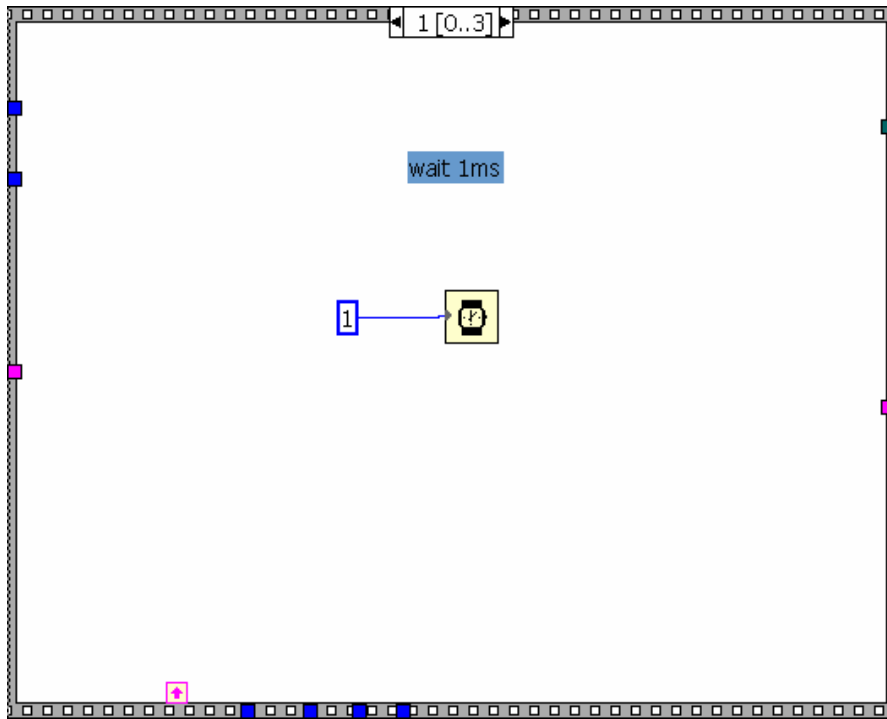
(b) Step 2

Step 1 initializes the network analyzer to use center frequency 5.2GHz and span 0Hz, with minimum sweep time and number of points 3, display linear frequency and take the S parameter as S21 by default by HP8722ES Set freq Spara.vi. Step 2 waits 10 milliseconds and then set the analog output of LabJack ‘1’, no demo with output voltage 5 voltage by default by **EAnalogOut.vi** .

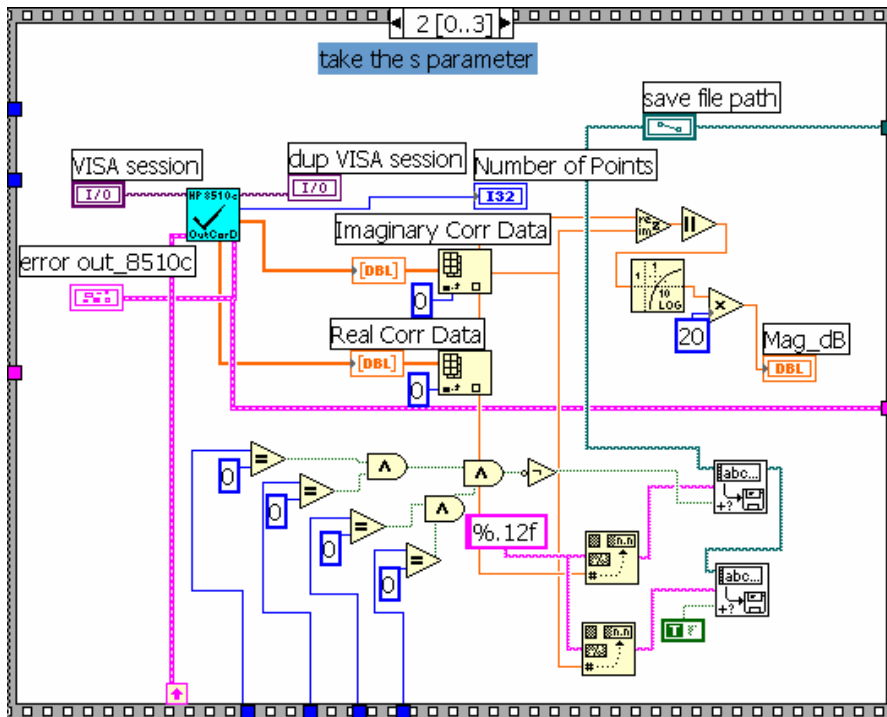


(c) Step 3

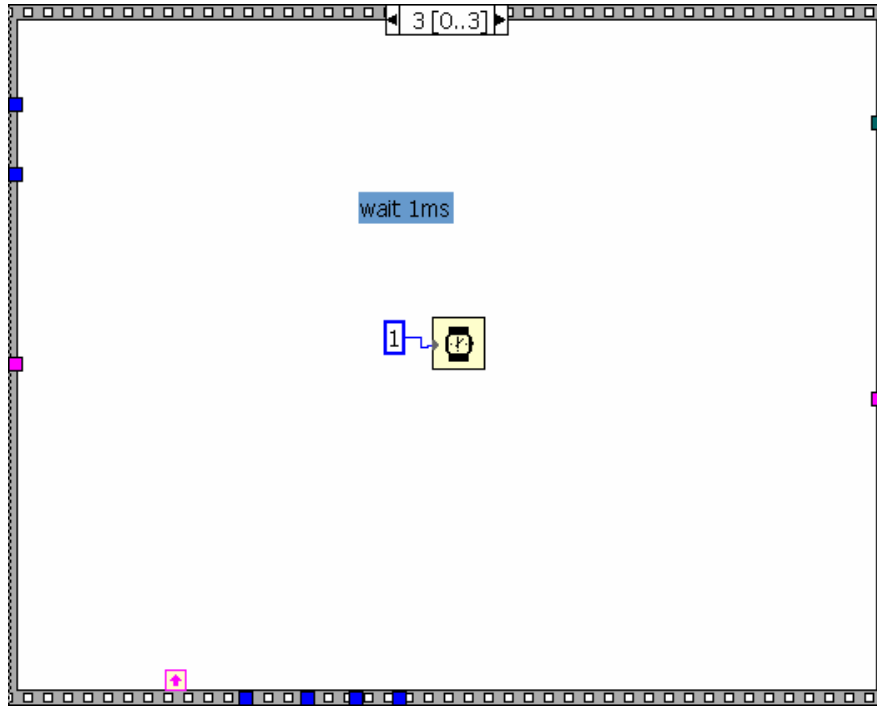
Step 3 sets the biasing outputs of receiving antenna arrays by using the **DigitalIO.vi** function to writes to all 20 Digital I/O. execution time for this function is 20 milliseconds or less. (It is the same for the block in (c) before (d) parts in C.7 Section except that block is for transmitting antenna arrays.)



(d) Step 4

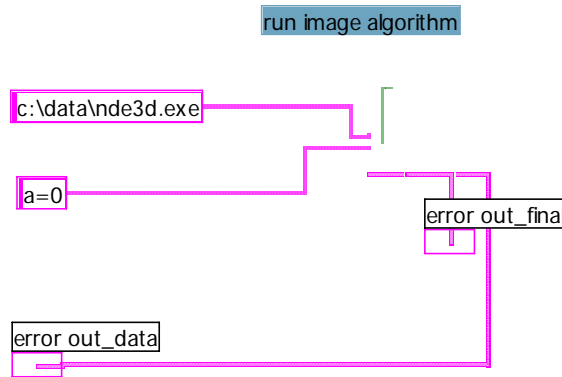


(e) Step 5



(f) Step 6

Step 4 waits 1 ms and step 5 takes the measurement data by using HP8510C Output Corrected Data.vi. This function output real/imaginary pairs from selected channel corrected data memory. Then data will be saved by Write Characters To File.vi. Step 6 waits 1 ms.



(g) Step 7

The 4-6 steps will be run for '128 times 128' sequences, then the image algorithm will be run by System Exec.vi at step 7 by. An image of the concrete will be generated after that.